ABSTRACT

Title of dissertation: THE EFFECTS OF GEOMETRY AND PATCH POTENTIALS ON CASIMIR FORCE MEASUREMENTS

Joseph Landon Garrett, Doctor of Philosophy, 2017

Dissertation directed by: Professor Jeremy Munday
Department of Electrical and Computer Engineering

Electromagnetic fluctuations of the quantum vacuum cause an attractive force between surfaces, called the Casimir force. In this dissertation, the first Casimir force measurements between two gold-coated spheres are presented. The proximity force approximation (PFA) is typically used to compare experiment to theory, but it is known to deviate from the exact calculation far from the surface. Bounds are put on the size of possible deviations from the PFA by combining several sphere-sphere and sphere-plate measurements.

Electrostatic patch potentials have been postulated as a possible source of error since the first Casimir force measurements sixty years ago. Over the past decade, several theoretical models have been developed to characterize how the patch potentials contribute an additional force to the measurements. In this dissertation,

Kelvin probe force microscopy (KPFM) is used to determine the effect of patch potentials on both the sphere and the plate. Patch potentials are indeed present on both surfaces, but the force calculated from the patch potentials is found to be much less than the measured force. In order to better understand how KPFM resolves patch potentials, the artifacts and sensitivities of several different KPFM implementations are tested and characterized. In addition, we introduce a new technique, called tunable spatial resolution (TSR) KPFM, to control resolution by altering the power-law separation dependence of the KPFM signal.

THE EFFECTS OF GEOMETRY AND PATCH POTENTIALS ON CASIMIR FORCE MEASUREMENTS

by

Joseph Landon Garrett

Dissertation submitted to the Faculty of the Graduate School of the
University of Maryland, College Park in partial fulfillment
of the requirements for the degree of
Doctor of Philosophy
2017

Advisory Committee:
Professor Jeremy N. Munday, Chair/Advisor
Professor Ian Appelbaum
Professor Victor Galitski
Professor Min Ouyang
Professor Jan Sengers

Dedication

I dedicate the following thesis to several members of my family.

First, to my parents, who spent so many years of their lives raising me and teaching me the value of creativity and exploration.

Second, to my creative and thoughtful wife, Ginny, who inspired and supported me during the writing of this thesis.

Acknowledgments

There are quite a few people to thank for their role in my development as a physicist. I will begin with the present and then journey further back into the past.

I would like to thank my committee for attending my dissertation defense: Jan Sengers, Min Ouyang, Victor Galitski, and Ian Appelbaum. I would like to thank my advisor Jeremy Munday for all the support that he has given me for these past several years, for listening to ideas for new experiments, and for reading through numerous manuscripts, including the one you are reading now. I would like to thank several professors of IREAP with whom I have worked at one time or another: Edo Waks, Tom Murphy, and Marina Leite. I would also like to thank the other researchers who have contributed to my understanding of the Casimir force, including Diego Dalvit and Ricardo Decca.

As part of the first cohort of Munday lab graduate students, I often had to look outside the walls of the Munday lab for senior graduate student expertise. I would like to thank Ryan Seuss and Shilpi Gupta in particular for the time and thought they gave to designing and working on experiments with me. I learned quite a bit about planning experiments and how to think about science in general, as a way of knowing, as a community, as a career, from the two of you. I would also like to thank all of the graduate students in the Munday lab: Lue Xu, David Somers[1], Kyle Sendgikoski, Kevin Palm, Joe Murray, Sarvenaz Memarzadeh, Dakang Ma, Lisa Krayer, Dongheon Ha, Tao Gong, and Dan Goldman. I would also like to thank

[1]I'm still grateful for the time you took over a special issue paper submission due two days before my wedding.

several post-docs and undergraduates in the lab: Taqiyyah Safi, Tarun Narayan, Adam Maraschky, Jongbum Kim, Meghan Fickett, and Coleman Delude. I'm also grateful for the time I spent working with members of the Leite lab: Beth Tennyson, John Howard, and Chen Gong. I would also like to thank Peter Megson for taking over the graduate student seminar when I stepped down as chair.

IREAP would not be such a great place to do research without all of the support we students receive from the staff. I would like to thank in particular: Kathryn Tracey for her helping with the graduate student seminar, Dottie Brosius for keeping us equipped with office supplies and providing the template for this thesis, Nancy Boone for all of her help sending giant boxes full of microscope equipment back and forth to Santa Barbara, and Nolan Ballew for building equipment for the lab. I would like to thank the UMD Fablab staff, and, in particular, Tom Loughran who kept the Denton e-beam running. The scientists at Asylum Research, including Mark Reitsma and Anil Gannepalli, provided me with invaluable technical support regarding our atomic force microscopy.

Of course, I did learn a little physics before I came to Maryland. At Ohio State University, I would like to thank Nandini Trivedi for introducing me to condensed matter physics research and Eric Duchon, who provided additional physics guidance and originally recommended the University of Maryland to me as a good school to attend. From Lakota East High School I would like to thank Sandee Coats-Haan for introducing me to the study of physics, and convincing me that I would much prefer a second year of high-school physics to a seventh year of band.

Anyway, you can still make music while doing physics. I learned that from

my bandmates in *Rayleigh Jeans and the Ultraviolet Catastrophes*: Nat Steinsultz, George Hine, Jeff Demers, and Madison Anderson. Thanks for all the wild noisy jamming. I am grateful to my friends in 'Physics House' for your friendship and culinary expertise: Alireza Seif, Kiersten Ruisard, Rachel Ruisard, Kevin Pedro, Meredith Lukow, Mahan Amouzegar, and my wife and RJUVC bandmates.

I am grateful to have the kindest people on earth as my parents, Barb and Greg Garrett. I am so lucky to have your support and encouragement. I'm grateful that I have a brother, Dan, who sits around and talks about mathematical modeling and data analysis on family vacations. I am grateful that Liz Garrett, his wife, is around to take care of him. I am grateful for my grandparents Perry "G.G." and George Landon "Grandaddy" Garrett for instilling a fascination with nature in me from a young age, and Robert and Joyce Eversole for teaching me the value of learning, and what the world was like in the years before I was born. I give my thanks to the rest of my family, too numerous to note here, for all their generosity and support throughout the years. Finally, I want to thank my wife, Ginny, for all of her exuberance and creativity throughout these past few years. I will love you forever and ever.

Table of Contents

List of Tables

List of Figures

List of Abbreviations

AFM	Atomic force microscopy
AM-	Amplitude modulation
DDS	Direct digital synthesizer
FLG	Few layer graphene
FM-	Frequency modulation
H-	Heterodyne
HOPG	Highly ordered pyrolytic graphite
IREAP	Institute for Research in Electronics and Applied Physics
JTC	Jump-to-contact
KPFM	Kelvin probe force Microscopy
LIA	Lock-in amplifier
OL	Open loop
PFA	Proximity force approximation
QLM	Quasi-local model
SLD	Superluminescent diode
TSR-	Tunable spatial resolution

List of Variables

Variable	Description
$\mathfrak{a}$	Coupling between DDS and LIA
A_{T}	Amplitude of carrier oscillation, also used for topography feedback
A_{D}	Amplitude of cantilever oscillation at ω_{D}
$\tilde{A}_{\mathrm{D}}$	A_{D} normalized by its value on a flat surface
A_{set}	Amplitude setpoint
A_ω	Amplitude of oscillation at ω_{D} generated by F_ω
b	Intercept of line fit for PFA bounds
$\mathfrak{b}$	Proportionality between drive voltage and shake amplitude
B	Bandwidth of low-pass filter on lock-in amplifier
$\mathscr{B}$	AM Casimir force measurement sensitivity
$\mathfrak{B}$	Fit parameter used to estimate k and γ
$C^{(m)}$	mth derivative of tip-sample capacitance
$\mathfrak{C}$	Autocorrelation function (radial)
d, $(\bar{d})$	Instantaneous (time-averaged) tip-sample separation
d'	Separation between misaligned spheres
d_0	Absolute tip-sample separation
d_0'	Absolute tip-sample separation for misaligned spheres
d_{max}	Maximum possible separation in a Casimir force measurement
d_{min}	Minimum possible separation in a Casimir force measurement
d_{pz}	Position of plate relative to initial position of plate
$\mathfrak{D}$	Cantilever deflection
E_{pp}	Energy per unit area between parallel plates
F_a	Electrostatic force component $\propto V_{\mathrm{AC}}(V_{\mathrm{K}} + V_0)$
F_b	Electrostatic force component $\propto V_{\mathrm{AC}}^2$
F_{C}	Casimir force
F_{es}	Capacitive force on cantilever
F_{H}	Hydrodynamic force
F_{pp}	Force per unit area between parallel plates
F_{r}	Force on rough sphere
F_{s}	Force on smooth sphere
F_{sp}	Force between a sphere and a plate
F_ω	Force at frequency ω
$\vec{F}_{\mathrm{side}}, \vec{F}_{\mathrm{dir}}$	Forces used for sideband or direct actuation
$G(\omega)$	Transfer function of cantilever at frequency ω

List of Variables (continued)

Variable	Description
h	Tip-cone height
k_i	Spring constant of eigenmode i
k_i^{eff}	Effective k_i (chapters 3 and 6)
l_{10-90},$l_{10-90}^{C^{(n+1)}}$	10-90 resolution, for method that depends on $C^{(n+1)}$
$L \equiv x - x_0$	(chapter 2) Distance from potential boundary
L	(chapters 3+) Cantilever beam length
$\mathscr{L}$	Lateral displacement of bottom sphere
m	Slope of line fit for PFA bounds
$n_{\text{det}}, n_{\text{dis}}, n_d$	Detection, displacement, or other noise amplitude spectral densities
$N(B)$	Noise power in detection bandwidth
P	Pressure (from patch potentials)
Q_i	Quality factor of eigenmode i
r	Radial separation (in-plane)
$\vec{r}_i$	Displacement of the tip apex when ith eigenmode is excited
R	Tip radius
$\mathbf{R}$	Rotation matrix
S_{E}	Extraneous signal in KPFM feedback
S_{K}	KPFM signal
S^{I},S^{Q}	In-phase (I) and $\pi/2$-shifted (Q) signals at lock-in
S_{set}	Signal setpoint
S_ω	Signal detected at frequency ω
t	Time
$t_c = 2\pi/\omega_{\text{c}}$	The cut-off time and the cut-off frequency
$\mathfrak{t}$	Water layer thickness
T	Temperature
V_0	Inherent contact potential difference
V_{b}	Surface voltage change across a boundary
V_{K},$V_{\text{K}}^{C^{(n+1)}}$	KPFM voltage, KPFM voltage near a boundary
$V_{\text{E}}, V_{\text{E}}^{\text{T}}$	Extraneous voltage artifacts
V_{m}	Minimum detectable voltage
V_{p}	Voltage perturbation applied to plate
$V_{\text{pl}}(r,\phi)$, V	Surface potential of the plate, sphere in PFA
V_{RMS}	RMS voltage of a surface potential image
V_{shake}	Voltage applied to drive piezo

List of Variables (continued)

Variable	Description
$W(\mathfrak{t})$	Relative increase in C due to water layer
$\vec{x}_{\text{bot}}$	Position of the bottom of the sphere
x_{t}	Tip-cone contact position
$Y_i(t)$	Displacement of ith eigenmode at time t
z_{cant}	Vertical displacement of cantilever beam
β'	Geometric correction to the PFA
$\gamma(\omega), \gamma_i$	Optical lever sensitivity of cantilever at frequency ω or eigenmode i
Γ_0	Damping of sphere far from plate
δ	Tip-cone contact angle (section 3.1)
δ	Signal from non-linearity of electrostatic force (section 4.3)
Δd	Plate piezo shake amplitude
$\Delta\omega$	Frequency shift
$\Delta\omega_c$	Error in initial frequency estimate
$\Delta\omega_{\text{err}}$	Extra frequency shift due to poor estimate of resonance frequency
$\Delta\phi$	Phase error in FM measurement
$\Delta\theta_{\text{ref}}$	Uncertainty in reference phase of LIA
ω_{A}	Frequency at which V_{AC} is applied
ω_{D}	Frequency at which the KPFM signal is detected
ω_i	Frequency of eigenmode i
ω_{M}	Frequency at which force is modulated
ω_{p}	Frequency of voltage perturbations applied to plate
ω_{T}	Frequency of topography/carrier oscillation
ϕ	Phase in FM measurement
ϕ_{A}	Phase of applied voltage V_{AC}
ϕ_{D}	Phase of shift of lock-in amplifier
ϕ_{T}	Phase of topography/carrier oscillation
$\Phi_i(x)$	Shape of cantilever eigenmode
θ_{holder}	Angle of the tip holder
Θ_i	Angle relative to vertical of the tip apex for the ith eigenmode
$\xi(Y_i)$	Angle of the line tangent to the cantilever at position x_{t} and displacement Y_i

List of publications

Portions of this thesis have been drawn from the publications listed below:

J. L. Garrett, D. A. T. Somers, J. N. Munday, "The effect of patch potentials in Casimir force measurements determined by heterodyne Kelvin probe force microscopy." *Journal of Physics: Condensed Matter* **27**, 214012 (2015).

J. L. Garrett, J. N. Munday, "Fast, high-resolution surface potential measurements in air with heterodyne Kelvin probe force microscopy." *Nanotechnology* **27**, 24 (2016).

J. L. Garrett, L. J. Krayer, K. J. Palm, J. N. Munday, "Effect of lateral tip motion on multifrequency atomic force microscopy." *Applied Physics Letters* **111**, 043105 (2017).

Other publications co-authored concurrently include:

D. Ma, **J. L. Garrett**, J. N. Munday, "Quantitative measurement of radiation pressure on a microcantilever in ambient environment," *Applied Physics Letters* **106**, 091107 (2015).

E. M. Tennyson, **J. L. Garrett**, J. A. Frantz, J. D. Myers, R. Y. Bekele, J. S. Sanghera, J. N. Munday, M. S. Leite, "Nanoimaging of open-circuit voltage in photovoltaic devices," *Advanced Energy Materials* **5**, 23 (2015).

R. J. Seuss, E. Leong, **J. L. Garrett**, T. Zhou, R. Salem, J. N. Munday, T. E. Murphy, M. Mittendorff, "Mid-infrared time-resolved photoconduction in black phosphorus," *2D Materials* **3**, 4 (2016).

J. L. Garrett, E. M. Tennyson, M. Hu, J. Huang, J. N. Munday, M. S. Leite, "Real-time nanoscale open-circuit voltage dynamics of perovskite solar cells." *Nano Letters* **17**, 042554 (2017).

Finally, I plan to submit several sections of this thesis to academic journals:

J. L. Garrett, D. A. T. Somers, J. N. Munday, "Measurement of the Casimir force between two spheres." *To be submitted* (2017).

J. L. Garrett, J. N. Munday, "*In situ* control of spatial resolution in scanning force microscopy." *To be submitted* (2017).

J. L. Garrett, K. Sendgikoski, D. A. T. Somers, J. N. Munday, "Sensitivity and accuracy in ambient Casimir force measurements." *To be submitted* (2017).

J. L. Garrett, K. Sendgikoski, J. N. Munday, "Casimir force measurement with patch potential force quantified on both surfaces." *To be submitted* (2017).

Chapter 1: Introduction to the Casimir force and a brief history of its measurement

The simplicity of H. B. G. Casimir's derivation has drawn much attention to the force which bears his name. In less than three pages, using basic concepts from quantum mechanics and electromagnetism, the attraction between perfectly conducting uncharged metal plates is calculated [1]. The ease of the calculation, and the fact that the force seems to come from *nowhere*, grants the force an allure to both physicists and the public. Despite its apparent simplicity, the Casimir force has a long history dating back to the 1870s, when the equations governing electricity and magnetism were first being developed by Maxwell and van der Waals was modifying the ideal gas law to take into account the attraction between particles [2]. Initially, the origin of the forces postulated by van der Waals (vdW) was unknown, but Lebedev, in his PhD work (1890s), posited that the force originated from molecules sending and receiving electromagnetic radiation [3]. In the 1930s, the vdW forces were calculated for several special molecular scenarios: two permanent dipoles, a permanent dipole and an induced dipole, and two induced dipoles [2]. Later in the decade, Hamaker showed that forces between individual molecules could be summed to approximate the force between surfaces [4]. Then, finally, Casimir realized two

key facts that put fluctuation forces on a firm foundation: (1) the fluctuations which contribute to the force are described by the bulk material optical properties and (2) the finite speed of light significantly affects the force and in most cases increases how quickly the force falls off with separation [2, 5]. Further developments by Lifshitz and coworkers generalized Casimir's ideas to arbitrary dielectric materials [6, 7].

Measurements of the Casimir force also have a long history. After five decades since the first experiments, and nearly two decades of intense activity, everyone agrees that the Casimir force has been observed [8, 9]—as well as several interesting properties such as repulsion and its material dependence [10–12]—but, some fundamental experimental questions remain unanswered, such as: what errors are typically present and what are the effects of probe and sample geometry? Moreover, one of the catalysts for the recent development of new measurements from the 1990s onward was the proposition that the Casimir force could be used in microelectromechanical systems (MEMS) as a switch or an actuator. While measurements on a silicon chip [13, 14] represent an important step towards utilizing the Casimir force, it has not yet been utilized in commercial devices.

Characterizing measurement uncertainties not only clarifies how accurately experiment can be compared to theory, but it also helps to show what other effects will be present in MEMS that utilize the Casimir force. One of the most significant of these effects, and one that has proven itself quite difficult to test, is the presence of patch potentials. A patch potential is a region on a surface with an electrostatic potential that differs from the surrounding regions. Electrons within the region of the patch potential have a different chemical potential than electrons outside the

region, so that even when the material is characterized by the same Fermi level, differences in the electrostatic potential are present. Two main sources of patch potentials have been identified: crystal orientation and adsorbates [15]. The differing work functions of different crystal faces primarily originate from electron double-layer effects at the surface [16]. Likewise, adsorbates also affect the surface dipole layer and the material's work function [17]. Patch potentials have been predicted since the earliest experimental comparisons to the Casimir-Lifshitz theory [18], but only recently have adequate theoretical treatments allowed its quantification from electrostatic measurements of interacting surfaces [15, 19]. Other major sources of error include roughness and separation determination. Furthermore, it is difficult to disentangle the Casimir force from hydrodynamic drag in air or liquid environments [20, 21].

In this thesis, new Casimir force measurements are discussed (including the first measurement between two metallized spheres), typical artifacts, and the effect of patch potentials on the measured force. Before that, Kelvin probe force microscopy is discussed, both as a tool to examine the surfaces used in later measurements, and as a simpler platform to introduce several of the errors which plague Casimir force measurements. The dissertation concludes with a new technique to align surfaces in Casimir force measurements, which allows sphere-sphere measurements to be performed. The sphere-sphere measurements are in turn used to put bounds on corrections to the proximity force approximation (PFA).

1.1 What is the Casimir force?

H. B. G. Casimir imagined a perfectly conducting box with sides of length L in which the boundary conditions only permitted certain electromagnetic modes defined by the wave numbers [1]:

$$k_x = \frac{\pi}{L} n_x, \qquad k_y = \frac{\pi}{L} n_y, \qquad k_z = \frac{\pi}{d} n_z, \tag{1.1}$$

where the n_i are integers, and d is the separation between the two walls perpendicular to the z-axis. Each mode has $\frac{1}{2}\hbar\omega$ energy in its quantum-mechanical ground state, where ω is the frequency of a particular mode. Casimir summed the energy of all the modes to find:

$$\frac{1}{2}\sum \hbar\omega = \hbar c \frac{L^2}{2\pi} {\sum_n}' \int_0^\infty \sqrt{\left(n^2 \frac{\pi^2}{d^2} + \chi^2\right)} \chi d\chi, \tag{1.2}$$

where the $'$ on $\sum$ indicates that the n=0 term is multiplied by 1/2. The total energy appears to be infinite, but only energy differences, rather than the total energy, lead to forces, so the energy at $d \to \infty$ is subtracted from the sum. The remaining energy per unit area is then:

$$\frac{E}{L^2} = -\frac{\hbar c \pi^2}{720 d^3}. \tag{1.3}$$

The force per unit area is then found to be:

$$\frac{F}{L^2} = -\hbar c \frac{\pi^2}{240 d^4}. \tag{1.4}$$

Modern calculations incorporate measured material dielectric functions following the theoretical developments of the 1950s [6, 7]. More recent developments have focused on how to include the zero-frequency transverse electric (TE) mode [22] and how to compute Casimir forces efficiently for different geometries [23–26].

The power law of the Casimir force can also be obtained by dimensional arguments. A conservative force is given by minus the spatial gradient of a potential energy. Such a force is proportional to an energy per distance, so that the force per unit area goes as the energy per distance to the third power. The energy of the quantum electromagnetic fluctuations goes as $\hbar\omega = \frac{\hbar c}{\lambda}$. To first order, we assume that the strongest contribution comes from λ that are comparable to the separation d, i.e. $\lambda \sim d$.[1] Thus, $\frac{F}{A} \propto \frac{\hbar c}{d^4}$.

The fundamental constants present in equation 1.4 reveal several characteristics of the Casimir force. The presence of $\hbar$ shows that the force depends on the quantum nature of the fluctuations. The presence of the speed of light, c, shows that the force depends on the speed at which fluctuations propagate between the surfaces. Finally, the force results from electromagnetic fluctuations, rather than electromagnetic charge, as can be noted by the absence of the electron charge, e, from the formula.

[1] Very large λ do not fit between the plates and very small λ, *e.g.* x-rays, become invisible to the plates and do not contribute to the force.

1.1.1 Proximity force approximation

The proximity force approximation (PFA) is used to compare Casimir force experiments to theory, because calculations of the Casimir force beyond the plate-plate geometry are computationally intensive [27]. The proximity force approximation is the assumption that the interaction between two curved surfaces can be modeled as the sum of a series of parallel plates. Derjaguin showed that for uniform surfaces, this approximation leads to a relationship between the force between curved surfaces and the energy between parallel plates [28]:

$$F_{\rm sp} = 2\pi R' E_{\rm pp}, \tag{1.5}$$

where R' is the effective radius of the interacting surfaces, $F_{\rm sp}$ is the sphere-plate force, and $E_{\rm pp}$ is the energy per unit area between parallel plates. In this thesis, we are concerned with the simpler sphere-sphere and sphere-plate interactions for which the effective radius is $R' = (R_1^{-1} + R_2^{-1})^{-1}$, where R_1 is the upper sphere and R_2 is the lower sphere. For the sphere-plate geometry, $R_2 \to \infty$, so that $R' \to R_1$.

To derive equation 1.5 from the proximity force approximation, we assume a sphere-plate geometry and a force with a power-law dependence on separation, *e.g.* the force per unit area is $F_{\rm pp} = Cd^{-n}$, with C a constant and $n>0$. The PFA states that force between a sphere and a plate is:

$$F_{\rm sp} = \int_0^{2\pi}\int_0^{R} \frac{C}{\left(d + \frac{r^2}{2R}\right)^n} r\,{\rm d}r{\rm d}\theta. \tag{1.6}$$

By integrating, the simplified PFA is verified to agree with equation 1.5:

$$F_{\rm sp} = 2\pi \frac{R}{n-1} \frac{C}{d^{n-1}}, \tag{1.7}$$
$$= 2\pi E_{\rm pp} R$$

where the term on the right is the potential energy per unity area that would give rise to the power-law force. Because the Casimir force depends on the optical properties of the samples used for the measurement, and because these optical properties vary significantly between different samples of the same material [29, 30], it is necessary to calculate the Casimir force using the optical properties of the exact samples. Because it is typically not computationally feasible to perform a complete Casimir force numerical calculation that includes both optical properties and the sphere-plate geometry, the proximity force approximation is used instead. Recent work has focused on how sample optical properties change corrections to the PFA [27].

1.2 A brief history of Casimir force measurements

Here we briefly discuss the Casimir force measurements made prior to and during my work on this thesis. The point here is to show how a gradual increase in precision enabled a flurry of new Casimir-based phenomena to be experimentally observed in the 1990-2000s. The rate of new discoveries has slowed significantly since 2010, with some authors expressing concern about experimental precision and accuracy claims [31–33].

Soon after the development of the Lifshitz theory, Sparnaay found that "The observed attractions do not contradict Casimir's theoretical prediction" [18], but the errors were too large to stringently test the theory. In a later experiment, the force between a chromium coated plate and a half-sphere was measured and found to follow the general power law of the force predicted by Lifshitz with a correction due to the optical properties of the chromium [8]. In 1997 the modern era of Casimir force measurements began with a measurement by Lamoreaux in which the Casimir force was measured between a gold-coated lens and a plate over separations that varied over an order of magnitude [9]. By observing the force over such a wide range of separations, its power law was deduced clearly, and agreed with the Casimir-Lifshitz prediction within experimental uncertainty.

After Lamoreaux, many more groups started to measure the Casimir force. Modern technology, particularly the development of the atomic force microscope (AFM) [34], enabled precise force measurement with smaller, more controllable samples. While the AFM was originally designed for spatial imaging more than force measurements, the sensitivity of AFM cantilevers to small forces [35] (<10 pN) allowed Casimir force measurements to be performed on commercial instrumentation. First among them was the group of Mohideen, who pioneered combining several sequential cantilever deflection versus distance curves, each at a different voltage, for the measurement of the Casimir force [36]. The spheres used in AFM measurements tend to be smaller than those used within torsion pendulums, and so, while the range of the earlier experiments usually covered separations out to several microns, the AFM experiments focused on measuring the force in the 20 - 700 nm separation

range [11, 20, 37].

1.2.1 New developments in Casimir force measurements

Many subsequent experiments expanded the range of materials and geometries between which the Casimir force could be measured, while others focused on developing microelectromechanical systems (MEMS) to utilize Casimir force. MEMS are expected to be one of the most pertinent applications of Casimir force experiments, and as such, they contributed some of the most accurate measurements [38,39] and have been used to study the dynamics accessible when driving with a non-linear force [40]. A large step towards fabricating MEMS devices that incorporate the Casimir force was the recent fabrication of a force measurement device etched into a silicon chip [13].

The dependence on the interacting materials' dielectric response was tested by measuring the force between dissimilar metals [41], semiconductors [42, 43], transparent conduction oxides [11], and semi-metals [44], and with 2D materials [45]. A gold and silicon dioxide interacting across bromobenzene led to the measurement of a repulsive Casimir force [10]. Several measurements have been performed in air and other gases [11, 37, 46]. While air is not predicted to alter the Casimir force, measurements in air show how effects such as a thin water layer and the hydrodynamic force must be accounted for in a MEMS device that relies on the Casimir force [47, 48].

The first steps towards a switchable Casimir force were made by optically

injecting charge carriers into a silicon membrane and observing the change in the measured force modulation [49]. By assuming all other forces were constant, *e.g.* electrostatic forces or temperature gradient induced forces, the observed force modulation was attributed to the Casimir force. Further work used two phases of AIST, a phase-change material often cited as a candidate for information storage [50]. The ideal experiment would utilize a material that can switch *in situ* and would allow calibration to ensure that it is only the Casimir force, and not some other force, that is varying. The difference between the Casimir forces between two states of a material is typically only a small portion of the total force, and so measurements of switchable forces are particularly sensitive to uncertainty. In chapters 2 and 3, heterodyne Kelvin probe force microscopy is introduced and its resolution is evaluated so that it can be used later to characterize patch potentials on the interacting surfaces used in Casimir force experiments. Chapter 4 presents our force measurement method, compares it to two other techniques in air, identifies several major sources of error, and quantifies how much each source contributes to the total uncertainty. Chapter 5 presents measurement of patch potentials on the surfaces used for Casimir force measurements, alongside force measurements themselves.

The unusual non-additivity of the Casimir force has led to several experiments and proposals involving the geometry-dependence of the Casimir force. Gratings are a common structure to study as they are simple to approach theoretically, as they can be defined completely by a period, a width, and a depth. Early studies of gratings in silicon showed a small increase in the total force compared to a proximity area approximation [51], while later studies on gold showed a decrease [52].

A recent MEMS device even measured a non-monotonic force [14]. A number of interesting theoretical predictions, including repulsion and non-contact gears, rely on controlling the interaction geometry [53–55]. Much recent work has also been focused on measuring a Casimir torque, which is caused by anisotropy of the interacting surfaces [56–59]. In chapter 6, our measurement of the Casimir force between two spheres is presented. Chapter 7 provides an outlook for future experiments.

Chapter 2: Kelvin probe force microscopy: a prelude

The atomic force microscope (AFM) was developed by Binnig and Quate [34] in 1986, about ten years before Lamoreaux measured the Casimir force out to six microns [9]. Even though much of the development of the atomic force microscope has been focused towards improved spatial resolution [60–62], rather than force measurements which came later [63,64], many of the techniques used in AFM operation are pertinent to Casimir force measurements as well. In addition, AFM has served as the basis for many scanning probe techniques, one of which, Kelvin Probe force microscopy (KPFM), is itself incorporated into many Casimir force measurements.

Atomic force microscopy is discussed in order to introduce the microscope and its components, as well as to introduce, in a simpler setting, some of the techniques used in the Casimir force measurements themselves. Later, in chapter 5, KPFM is used to determine the patch potentials on gold surfaces used for Casimir force measurements. This chapter is a modified version of [65].

2.1 History of Kelvin probe force microscopy

The original amplitude-modulation Kelvin probe force microscopy (AM-KPFM) method [66] has been used in numerous studies investigating nanoscale phenomenon

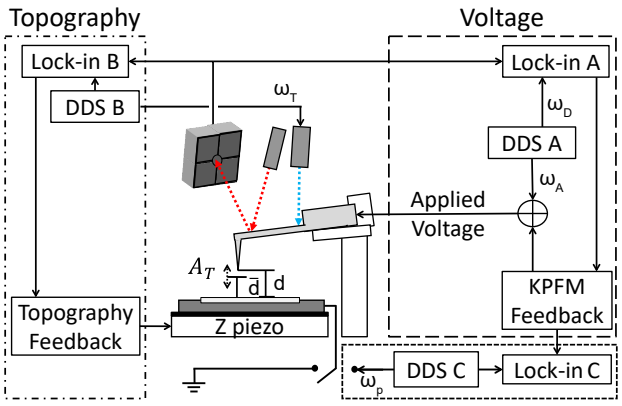

Figure 2.1: A feedback loop controls the separation between a photothermally driven cantilever and the sample through the cantilever's oscillation amplitude by adjusting the sample height (left). A voltage V_{AC} at frequency ω_{A} is added to V_{K}, the KPFM voltage, and applied to the probe. The cantilever oscillation at ω_{D} is then detected by lock-in amplifier B and used by a feedback loop to control the DC voltage applied to the cantilever (right). A third lock-in amplifier measures the response of V_{K} to a perturbation in order to deduce the KPFM transfer function.

including: potential contrast between metals [67], components of integrated circuits [68], semiconductor doping [69], pn junctions [70], self-assembled monolayers [71], Langmuir films [72], crystal orientation of metals [73], and biomolecular binding to DNA [74]. Developments such as lift mode [75] alleviated problems with adhesion and allowed the investigation of softer surfaces [76, 77]. AM-KPFM may seem suited for fast measurements, as it can operate quickly, and scan speeds of over 1 mm/s have been reported [74]; however, in AM-KPFM, the voltage contrast is typically only a qualitative representation of the surface potential due to an averaging effect of the cantilever, the stray capacitance effect [75, 78–80]. Moreover, AM-KPFM is susceptible to a class of artifacts that originate from interfering signals and appear in traditional KPFM measurements as topographical coupling [81–84].

The development of Frequency-Modulation (FM) KPFM [85] improved spatial resolution and repeatability [86–88] and has been used to quantitatively compare

nanoscale potentials with macroscopic work functions on both semiconductors [89] and graphene [88], to identify semiconductor crystal orientations [90], to characterize lipid self-organization [91], to quantify band bending at grain boundaries [92], to study charge transport and trapping in quantum dots [93], and to investigate the charge distribution at sub-molecular and atomic length scales [94,95]. However, dynamics are difficult to measure with FM-KPFM because of its slow scan speeds—the result of potential and topographic feedback loops detected near the same cantilever resonance, limiting detection bandwidth [86,87].

Techniques that try to couple the repeatability and spatial resolution of FM-KPFM with enhanced time resolution include time resolved electrostatic force microscopy and pump-probe KPFM, which both probe the dynamic response to an impulse point-by-point [96,97], and open loop (OL) KPFM techniques, which eliminate the KPFM voltage feedback loop [98–100]. However, not every dynamic process is caused by an impulse, and the typical scan speed with high-resolution open-loop techniques is about 1 μm/s [98,100], slower than AM-KPFM.

Operation in air is necessary to study biological molecules such as lipids and DNA [74,101] and to study solar cell properties such as open-circuit voltage and degradation in realistic operation conditions [102,103]. However, developments of KPFM have often focused on operation in vacuum [85,104]. In air, challenges such as vastly lower Q factors, which reduce sensitivity, and a thin adhesive water layer must be overcome [105].

A recent technique, Heterodyne (H) KPFM, operates similarly to FM-KFPM but separates the topography and voltage signals by hundreds of kHz [104]. Orig-

inally, in vacuum, the separation was utilized to increase the voltage sensitivity through amplification by the second cantilever eigenmode, while maintaining spatial resolution equal to FM-KPFM [104, 106]. Measurements in vacuum show that H-KPFM, like FM-KPFM, avoids the stray capacitance artifact that affects AM-KPFM [80].

2.1.1 Heterodyne KPFM

Here we demonstrate that H-KPFM combines the repeatability and spatial resolution of FM-KPFM with scan speeds of up to 32 μm/s (1x1 μm, 256×256 pixels, 16 s, trace and retrace). Moreover, H-KPFM achieves its time resolution without requiring an impulse. We show that it is not susceptible to several topographical artifacts that hinder the other KPFM methods. We demonstrate that it is compatible with lift mode. A second implementation of H-KFPM is also introduced, in which the topography is detected with the second cantilever resonance and the voltage with the first, for additional voltage sensitivity. The temporal resolution, voltage contrast, and spatial resolution of H-KPFM are each compared to those of both FM- and AM-KPFM. It is deduced that H-KPFM improves upon the spatial resolution of AM-KPFM and improves upon the scan speed of FM-KPFM, resulting in a new technique with improved performance in ambient conditions.

2.1.2 Analysis of the KPFM method

In KPFM, a signal, S_{K}, is generated by applying an AC voltage, V_{AC}, at frequency ω_{A} to a conductive tip above a grounded sample. A feedback loop applies a KPFM voltage, V_{K}, to the probe so that S_{K} vanishes. The signal on which the KPFM feedback acts is:

$$S_{\mathrm{K}} = -\zeta_j(V_{\mathrm{K}} + V_0), \tag{2.1}$$

where $V_0 = V_{\mathrm{tip}} - V_{\mathrm{sample}}$ is the contact potential difference between the tip and sample when both are grounded, and $\zeta_j \equiv \zeta_j(V_{\mathrm{AC}})$ is the sensitivity, which depends on the KPFM technique used (indicated through the subscript j), V_{AC}, the probe geometry, and imaging settings: such as the lift height. When $V_{\mathrm{K}} = -V_0 = V_{\mathrm{sample}} - V_{\mathrm{tip}}$, the signal vanishes. An image is created from the recorded V_{K} as the cantilever raster scans the surface. The KPFM signal is written in the form of equation 2.1 in order emphasize the similarity of H-KPFM to prior KPFM techniques and to facilitate their comparison.

In AM-KPFM, S_{K} is detected at the same frequency as the applied V_{AC} (↕ in figure 2.2), *i.e.* $\omega_{\mathrm{D}} = \omega_{\mathrm{A}}$ for AM-KPFM. Here we calculate the force above a conducting sample by modeling the tip-sample system as an metallic capacitor with energy $U = \frac{1}{2}CV^2$. The case for semiconductors is more complicated, but KPFM feedback operation is similar, and reduces to the metal case in the heavily-doped limit [107]. The force on the cantilever has components at frequencies DC, ω_{D}, and

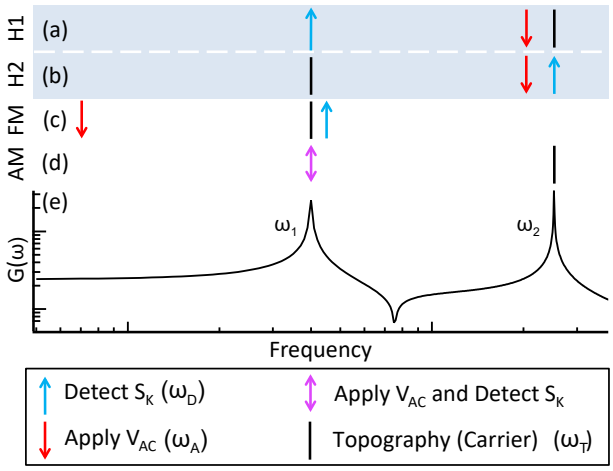

Figure 2.2: In H-KPFM (a,b) an alternating voltage is applied at a frequency $\omega_2 - \omega_1$ (↓). The cantilever's response is mixed with oscillation at the carrier frequency in order to be detected at one resonance (↑). The carrier oscillation occurs at another resonance and is also used to maintain time-averaged distance to the surface (|). Likewise, in the sideband implementation of FM-KPFM (□, c) a voltage is applied and the response detected at different frequencies: the alternating voltage is applied at $\omega_A \ll \omega_1$ and detected at $\omega_1 + \omega_A$. In AM-KPFM ( ), the alternating voltage is applied at the same frequency at which the cantilever response is detected (↕). The magnitude of the cantilever transfer function $G(\omega)$ with each eigenmode modeled as a point-mass, is shown in (e).

$2\omega_D$. The vertical force on the cantilever at frequency ω_D is then [75]:

$$F_{\omega_D} = -C' V_{AC}(V_K + V_0), \tag{2.2}$$

where $C' = \frac{\partial C}{\partial d}$. We assume that the motion of each cantilever eigenmode is purely along the $\hat{z}$-axis so that the transfer function of the cantilever $G(\omega)$ relates the driving force on the tip to the oscillation amplitude A_D of the cantilever:

$$A_D = G(\omega_D) F_{\omega_D}. \tag{2.3}$$

The optical lever sensitivity $\gamma(\omega_D)$ relates the signal generated at the photodetector

to the amplitude of cantilever oscillation, so that:

$$\begin{aligned} S_{\text{photo}} &= \gamma(\omega_{\text{D}})A_{\text{D}}, \\ &= -\gamma(\omega_{\text{D}})G(\omega_{\text{D}})C'V_{\text{AC}}(V_{\text{K}}+V_0). \end{aligned} \tag{2.4}$$

The signal from the photodetector is recorded by a quadrature lock-in amplifier with relative phase ϕ_{D}:

$$\begin{aligned} S^{\text{I}} &= \text{Re}[-\gamma(\omega_{\text{D}})G(\omega_{\text{D}})C'V_{\text{AC}}(V_{\text{K}}+V_0)e^{i\phi_{\text{D}}}], \\ S^{\text{Q}} &= \text{Re}[-\gamma(\omega_{\text{D}})G(\omega_{\text{D}})C'V_{\text{AC}}(V_{\text{K}}+V_0)e^{i(\phi_{\text{D}}+\frac{\pi}{2})}], \end{aligned} \tag{2.5}$$

where S^{I} and S^{Q} are the in-phase and quadrature components of the signal, respectively, at the lock-in amplifier. The KPFM feedback loop operates on S^{I}, and when put in the form of equation 2.1 is:

$$S_{\text{K}} \equiv S^{\text{I}} = -\zeta_{\text{AM}}(V_{\text{K}}+V_0), \tag{2.6}$$

where the sensitivity of AM-KPFM is:

$$\zeta_{\text{AM}} = \text{Re}[\gamma(\omega_{\text{D}})G(\omega_{\text{D}})C'V_{\text{AC}}e^{i\phi_{\text{D}}}]. \tag{2.7}$$

The relative phase of the lock-in amplifier, ϕ_{D}, is adjusted in order to maximize the sensitivity.

Table 2.1: Example cantilever characteristics

Name	ω_1 (kHz)	k_1 (N/m)	Q_1	γ_1 (V/nm)	ω_2	k_2	Q_2	γ_2
HQ:CSC35/Pt-C (μmasch)	130	5.0	230	0.030	810	88	440	0.070

Table 2.2: Common artifacts in Kelvin probe force microscopy

Type	Example Source	H	FM	AM
Extraneous Signal (S_{E})				
Time-independent	AC inductive coupling, between V_{AC} and piezo (figure 2.3) [84]	-	-	×
Periodic	Topographical oscillation detected in voltage bandwidth (figure 2.6i)	-	×	-
Intermittent	Collision with surface	×	×	×
Geometric				
Stray Capacitance	Long-range electrostatic force from cantilever [75, 78, 80]	-	-	×
Tip trajectory	The tip apex trajectory of higher eigenmodes is not vertical (section 3.1, [108])	×	-	×

Legend: × = large artifact, - = small artifact

In H-KPFM and FM-KPFM, the cantilever is shaken with amplitude A_{T} at the carrier frequency ω_{T} by a non-electrostatic method (here, photothermally), V_{AC} is applied at ω_{A}, and the KPFM signal is detected at ω_{D} (|, ↓, and ↑, respectively, in figure 2.2). The oscillation A_{T} is used for topography control in single-pass mode, but is also critical for the H-KPFM signal, and so must be present, even when lift mode is used. We assume that the cantilever position is well-approximated by the sinusoidal motion at ω_{T} (figure 2.2), so that:

$$(d - \bar{d}) = A_{\mathrm{T}} \cos(\omega_{\mathrm{T}} t + \phi_{\mathrm{T}}), \tag{2.8}$$

where z is the instantaneous tip-sample separation, $\bar{d}$ is the time-averaged separation, A_{T} is the amplitude of the carrier oscillation, and ϕ_{T} is the phase. Here we Taylor expand the tip-sample electrostatic force around its time-averaged height $\bar{d}$ so that the capacitive force on the cantilever is [104]:

$$\begin{aligned} F_{\mathrm{es}} = &- \left[C' + C'' A_{\mathrm{T}} \cos(\omega_{\mathrm{T}} t + \phi_{\mathrm{T}}) \right] \\ &\times \frac{[V_{\mathrm{AC}} \cos(\omega_{\mathrm{A}} t + \phi_{\mathrm{A}}) + V_{\mathrm{K}} + V_0]^2}{2}. \end{aligned} \tag{2.9}$$

As in AM-KPFM, a term linear in V_{AC} is used for the KPFM feedback, and there are three frequencies at which such a signal is generated: ω_{A}, $\omega_{\mathrm{A}} + \omega_{\mathrm{T}}$, and $|\omega_{\mathrm{A}} - \omega_{\mathrm{T}}|$. The force at the first frequency, proportional to C', is used for AM-KPFM (see equation 2.2), while the forces at the second and third frequencies, each

proportional to C'', are used for H-KPFM. Then, up to a phase shift, each force is:

$$F_{\omega_{\mathrm{D}}} = -\frac{C'' A_{\mathrm{T}}}{2} V_{\mathrm{AC}}(V_{\mathrm{K}} + V_0). \tag{2.10}$$

In this chapter, we choose $\omega_{\mathrm{D}} = \omega_{\mathrm{A}} + \omega_{\mathrm{T}}$. The case $\omega_{\mathrm{D}} = |\omega_{\mathrm{A}} - \omega_{\mathrm{T}}|$ results in an equivalent force. Then, as with AM-KPFM above, the signal used for H-KPFM feedback depends on the cantilever transfer function and the optical lever sensitivity at the detection frequency, so that the signal at the photodiode is, up to a phase shift:

$$S_{\mathrm{photo}} = -\frac{\gamma(\omega_{\mathrm{D}}) G(\omega_{\mathrm{D}}) C'' A_{\mathrm{T}}}{2} V_{\mathrm{AC}}(V_{\mathrm{K}} + V_0). \tag{2.11}$$

Once the phase shift is included, the H-KPFM feedback signal is put in the form of equation 2.1 with sensitivity:

$$\zeta_{\mathrm{H}} = \mathrm{Re}\left[\frac{\gamma(\omega_{\mathrm{D}}) G(\omega_{\mathrm{D}}) A_{\mathrm{T}}}{2} C'' V_{\mathrm{AC}} e^{i(\phi_{\mathrm{T}} + \phi_{\mathrm{A}} + \phi_{\mathrm{D}})}\right]. \tag{2.12}$$

Thus the sensitivity of H-KPFM differs from AM-KPFM both by its dependence on C'' instead of C' and by its dependence on the carrier oscillation amplitude A_{T}. If it is necessary to scan far from the surface, A_{T} can be increased to enhance sensitivity. Note that FM-KPFM similarly depends on A_{T} [87].

In H-KPFM, both the detection frequency, ω_{D} and the carrier oscillation frequency, ω_{T}, are free to be chosen, and once chosen, determine the frequency at which V_{AC} is applied, ω_{A}. Earlier works on H-KPFM considered the case $\omega_{\mathrm{T}} = \omega_1$, the

first cantilever resonance, and $\omega_D = \omega_2$, the second cantilever resonance [80,104,106]. In this article, this implementation is called "H2" for heterodyne amplified by the second cantilever resonance. Here the case $\omega_T = \omega_2$, $\omega_D = \omega_1$ is also considered, for enhanced sensitivity, and we call it "H1" because S_K is amplified by the first resonance.

2.2 Implementation

2.2.1 Experimental setup

All methods are implemented on a commercial AFM (Cypher, Asylum Research). The motion of a platinum-coated cantilever is measured with an optical lever employing a 860 nm laser and detected by a quad-photodiode. The optical lever sensitivity is determined for each eigenmode from amplitude vs. distance curves, and the spring constants are determined by fitting the cantilever's thermal spectrum (table 2.1).

KPFM is implemented using two direct digital synthesizers (DDS), each paired with a lock-in amplifier (LIA). In particular, the cantilever is excited at ω_T photothermally by DDS B (figure 2.1) for topography control. DDS A generates an AC voltage at frequency ω_A that is applied to the probe. LIA A detects the cantilever's oscillation at ω_D. The relative phases of signals from DDS A and B are maintained through the synchronization of the AFM's internal clock. To measure the transfer function of the KPFM loop, DDS C is used to apply an AC voltage, V_p to the substrate. LIA C detects the response of V_K to the perturbation.

AM feedback is used for the topographical loop for all KPFM methods. In our earlier experiment [109], an FM feedback loop controlled the tip-substrate distance while maintaining attractive-mode scanning [110]. Although FM topography feedback is adapted for the original implementation of H-KPFM [104], it contains one major disadvantage: the frequency shift is a non-monotonic function of distance [64] and so the tip collides with the surface when its motion deviates too far from the topography setpoint. With AM topography control, the feedback operates on a signal that is monotonic with distance, except at one bistability that can be avoided [110]. When AM feedback is used for topography, small perturbations, that once destroyed probes, no longer affect scan stability.

The settings for the different KPFM techniques are chosen to realistically represent each technique's capabilities and are similar to those of previous experiments [86, 87]. FM-KPFM is implemented with sideband detection [87]: $\omega_{\mathrm{T}} = \omega_1$ and $\omega_{\mathrm{D}} = \omega_1 + \omega_{\mathrm{A}}$, and the modulation frequency $\omega_{\mathrm{A}} = 2$ kHz is maintained. For AM-KPFM, V_{AC} is applied at ω_1, and the topography loop operates at ω_2. For H-KPFM, the H1 implementation uses $\omega_{\mathrm{T}} = \omega_2$ and $\omega_{\mathrm{D}} = \omega_1$, while $\omega_{\mathrm{T}} = \omega_1$ and $\omega_{\mathrm{D}} = \omega_2$ for H2 (see figure 2.2). For all methods, $V_{\mathrm{AC}} = 1$ V.

All scans are performed on a micron-sized flake of few-layer graphene (FLG) on boron doped silicon with a thin native oxide layer (15-25 Ohm-cm, Virginia Semiconductor), prepared by exfoliation [111]. Both flakes of highly ordered pyrolytic graphite (HOPG) and FLG are observed with AFM (figure 2.6). The HOPG is a few tens of nm tall and causes band bending in the Si surface potential at its edges but has negligible patch potentials. The FLG is ≈ 1 nm high and does not change

the surface potential of Si around it but is covered with patch potentials. Because the FLG/Si boundary has less topography change, and a surface potential profile that is symmetric around the boundary, it is chosen for the following measurements.

2.2.2 Eliminating artifacts

Several artifacts originate from signals interfering with the Kelvin probe signal, S_{K} [81,82,84,112]. Examples of such signals include AC coupling between V_{AC} and a piezo in the cantilever holder (figure 2.3) or detection of the topography oscillation (at ω_{T}) within the lock-in amplifier (LIA) bandwidth (table 2.2). The resulting signal detected at the LIA contains both the desired signal, S_{K}, and an extraneous signal, S_{E}, and is given by:

$$S^{\mathrm{I}} = S_{\mathrm{K}} + S_{\mathrm{E}}. \tag{2.13}$$

A setpoint, S_{set} for the voltage feedback loop is chosen to compensate for S_{E} (above we assume $S_{\mathrm{E}} = 0$, and so a setpoint is not needed). When both S_{E} and S_{set} are included, the Kelvin probe loop detects the voltage:

$$V_{\mathrm{K}} = -V_0 + V_{\mathrm{E}}, \tag{2.14}$$

which contains an extraneous voltage:

$$V_{\mathrm{E}} = \frac{S_{\mathrm{E}} - S_{\mathrm{set}}}{\zeta_j}. \tag{2.15}$$

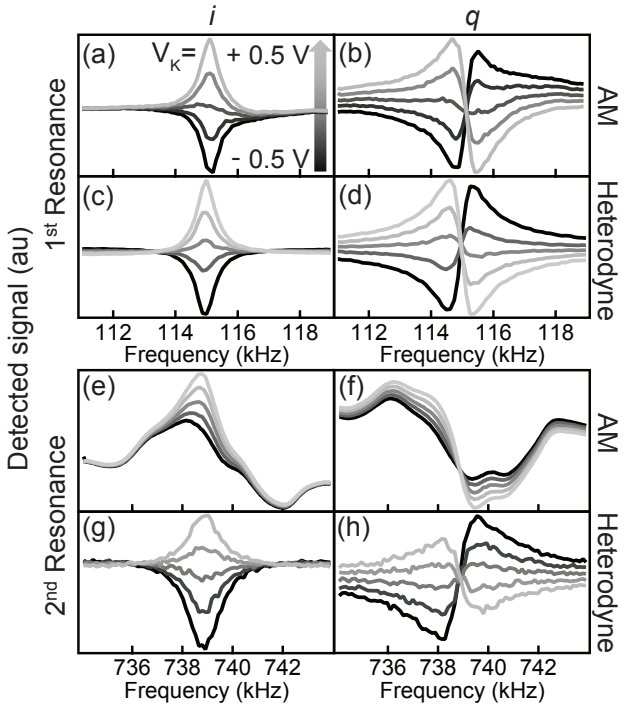

Figure 2.3: H-KPFM removes the distortion caused by AC coupling in the KPFM signal vs. detection frequency curves ($S^{\mathrm{I}}_{\mathrm{LIA}}$ vs ω_{D} and $S^{\mathrm{Q}}_{\mathrm{LIA}}$ vs ω_{D}). (a,b) At the first eigenmode, the in-phase (I) and quadrature (Q) components of the AM-KPFM signal show little distortion, but (e,f) at the second eigenmode, distortion due to inductive AC coupling between the KPFM voltage and tip holder, which increases with frequency, is observed. (c,d,g,h) Heterodyne excitation generates no distortion. The KPFM voltage applied to the tip, V_{K}, is sampled at values above and below the contact potential difference. Similar measurements were used to detect AC coupling in [81].

The topography is imprinted on V_{K} through the height-dependence of ζ_j, the sensitivity from equation 2.1, which complicates attempts to remove the artifact in post-processing [84].

Conversely, the height dependence of V_{E} can also be used to identify S_{E}. If S_{E} is small enough and does not vary in time, S_{set} can be chosen so that the numerator of equation 2.15 vanishes. In this dissertation, the height dependence of V_{K} is used to choose S_{set}. If a sample has uniform surface potential, then:

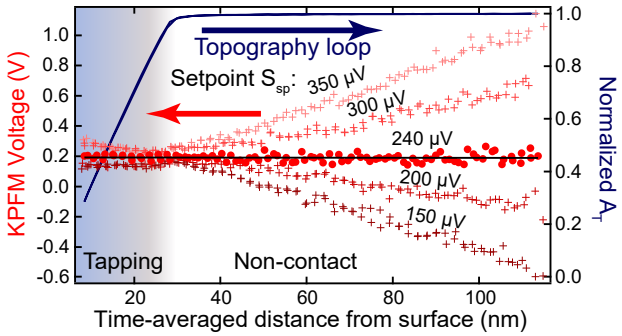

Figure 2.4: The setpoint of the KPFM feedback loop is adjusted to minimize the height-dependence of the KPFM voltage, V_{K}. Here the setpoint is swept from 150 to 350 μV over several approaches. The center curve (240 μV, •) shows a distance dependence of only 0.03 mV/nm. The dark blue curve indicates the topographical oscillation amplitude normalized to its value far from the surface.

$$\frac{\mathrm{d}V_{\mathrm{K}}}{\mathrm{d}\bar{d}} = \frac{\mathrm{d}V_{\mathrm{E}}}{\mathrm{d}\bar{d}} = \frac{S_{\mathrm{set}} - S_{\mathrm{E}}}{\zeta_j^2}\frac{\partial \zeta_j}{\partial \bar{d}}. \tag{2.16}$$

If $\mathrm{d}V_{\mathrm{K}}/\mathrm{d}\bar{d} \approx 0$, then $S_{\mathrm{set}} \approx S_{\mathrm{E}}$, as $\mathrm{d}\zeta_j/\mathrm{d}\bar{d}$ does not vanish.

To minimize V_{E}, the KPFM feedback setpoint, S_{set}, is varied over a range of 200 μV, and a V_{K} vs. height curve is recorded for each S_{set} (figure 2.4). For most S_{set}, the measured V_{K} does depend on height, indicating that $S_{\mathrm{set}} \neq S_{\mathrm{E}}$. The variation amongst the curves decreases when the tip-sample separation is reduced (until intermittent contact with the sample begins at $\approx$ 20 nm). The setpoint with the least distance dependence (240 μV), is maintained for the KPFM scans. The offset originates at the output of the low-pass filter on the lock-in amplifier for our setup, and it varies slightly from day to day, so the calibration must be repeated for every set of measurements.

2.3 Resolutions

The temporal, voltage, and spatial resolutions of the different KPFM implementations are compared through several tests, the results of which are summarized in table 2.3.

2.3.1 Time resolution

H-KPFM achieves fast time resolution by avoiding several artifacts that limit speed of the other KPFM techniques (Table 2.2). Because several limits on KPFM time resolution are proportional to ω_{D}, such as the bandwidth of a cantilever resonance ($\omega_{\mathrm{D}}/2Q$) and the Nyquist frequency ($\omega_{\mathrm{D}}/2$), higher resonant frequencies are expected to increase bandwidth. However, for AM-KPFM, higher frequencies also increase the AC coupling [84] (figure 2.3). AC coupling does not affect H-KPFM or FM-KPFM as significantly because the applied and detected signals are at different frequencies. Consequently, H-KPFM can employ cantilevers with higher resonant frequencies than AM-KPFM. This limitation of AM-KPFM is due to the drive piezo that is present in most cantilever holders. Additional circuitry can mitigate this artifact [81–83], but typically the circuitry must be custom-made.

On the other hand, the artifact that limits FM-KPFM scan speed is fundamental to its operation. In both H- and FM-KPFM, carrier and KPFM signals must be present at the same time. If $A_{\mathrm{T}} = 0$, then S_{K} vanishes, even in lift mode (equation 2.11, [87]). FM-KPFM scan speed is limited by a periodic S_{E} imprinted on the KPFM signal because the two signals, at ω_{D} and ω_{T}, are so close in frequency

space. Then the extraneous signal is estimated by considering how the cantilever oscillation A_{T} at ω_{T} is detected by a lock-in amplifier with reference signal at ω_{D}. When the signal is input into equation 2.15, the extraneous voltage is:

$$V_{\mathrm{E}}^{\mathrm{T}} = \frac{\gamma(\omega_{\mathrm{T}})A_{\mathrm{T}}}{\zeta_j}\mathrm{Re}\left[\frac{e^{i(\omega_{\mathrm{A}}t)}}{1+i\omega_{\mathrm{A}}/(2\pi B)}\right], \tag{2.17}$$

where B is the bandwidth of the LIA's low-pass filter, and we set $S_{\mathrm{set}} = 0$ for simplicity. In typical KPFM operation, the prefactor, $\frac{\gamma(\omega_{\mathrm{T}})A_{\mathrm{T}}}{\zeta_j}$, is large compared to the surface voltage contrast being measured. To reduce $V_{\mathrm{E}}^{\mathrm{T}}$ then, B must be chosen so that $B \ll \omega_{\mathrm{A}}$. For H-KPFM ω_{A} >100 kHz, so the bound on B is large. FM-KPFM, however, typically works with $\omega_{\mathrm{A}}/2\pi \approx 1-3$ kHz, which limits B. $V_{\mathrm{E}}^{\mathrm{T}}$ decreases with increasing ω_{A}, which can be used to increase the available bandwidth even though it concurrently decreases the sensitivity because $|G(\omega_1+\omega_{\mathrm{A}})|$, which is proportional to the sensitivity, decreases with increasing ω_{A}. Note also that because $V_{\mathrm{E}}^{\mathrm{T}}$ is periodic in time it cannot be mitigated by varying the KPFM feedback loop setpoint.

Previous measurements of time resolution either investigate the KPFM feedback loop response to a periodic voltage applied to the setpoint [87], or substrate [113], or how quickly a well-characterized sample can be scanned while retaining KPFM contrast [74]. Here the former method is used to estimate the cut-off frequency, ω_{c}, which is defined as the frequency at which the KPFM loop response has dropped to $\approx 71\%$ of the low-frequency response (-3 dB). In table 2.3, the cut-off time, $t_{\mathrm{c}} = 2\pi/\omega_{\mathrm{c}}$, is listed instead, so that smaller values indicate a better resolution.

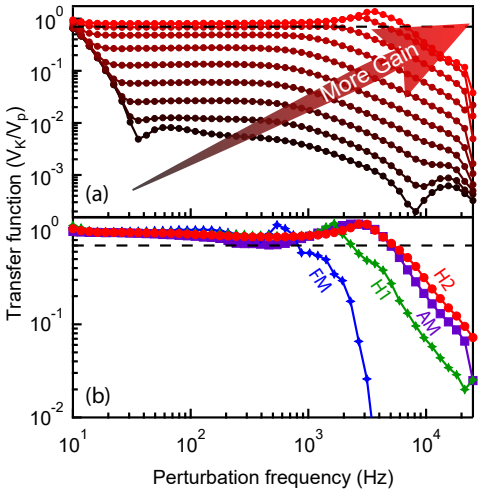

Figure 2.5: The transfer functions for the different KPFM methods are measured by applying a periodic voltage perturbation to the substrate and recording the response of the KPFM loop. (a) The transfer function of a H-KPFM voltage feedback loop increases and becomes more uniform as the gain is increased (H2 implementation). The proportional gain is increased 3 orders of magnitude, and overshoot is constrained to $\frac{V_K}{V_p} \leq 1.2$. A dashed line indicates the -3 db point used to calculate the cut-off frequency, ω_c. (b) The cut-off frequency depends strongly on the method used, varying by almost an order of magnitude. The gain for each of the methods is chosen by the same optimization procedure.

The reported time resolutions of AM-KPFM typically exceed those of FM-KPFM, even though the specific resolution depends on both the cantilever and atomic force microscope used. Of the references discussed here, a few optimize temporal resolution for their AFMs [74, 113]. For the others, the speeds cited are typical of an imaging method rather than the outcome of an optimization procedure. Diesinger *et al.* [113] report an implementation of AM-KPFM that achieves $\omega_c/2\pi \approx$ 200 Hz, limited by the analog-digital conversion of the KPFM loop. In air, Sinensky and Belcher demonstrate that AM-KPFM can maintain some voltage contrast at scan speeds up to $1,172$ μm s^{-1}, by scanning 2-μm wide stripes of DNA [74]. In the

language used here, that corresponds to $\omega_c/2\pi \approx 1.2$ kHz. FM-KPFM is reported to operate with similar speed when either in the sideband ($\omega_c/\pi \approx 35$ Hz) or phase locked loop ($\omega_c/2\pi \approx 30$ Hz) is used, even though the sources of speed limitation are dissimilar [87,114]. Recent improvements to the KPFM feedback increase the cut-off frequency to 100 Hz with a larger modulation frequency (4 kHz) [115]. Reported open-loop FM-KPFM scan speeds include 0.85 $\mu m s^{-1}$ (or 5 min per (500 nm)^2, 256×256 pixel scan, trace and retrace) [100] and 1.3 $\mu m s^{-1}$(or 3 min per (450 nm)^2, 256×256 pixel scan, trace and retrace) [98].

To measure the closed loop transfer function of each KPFM method, an AC voltage ($V_p = 1$ V at perturbation frequency ω_p) is applied to the substrate by a third DDS, while the cantilever height is maintained at the surface by a topographical feedback loop, with $A_T \approx 8$ nm. The KPFM loop tracks the voltage, and $V_K(\omega_p)$ is detected by a third lock-in amplifier. The frequency is swept from $\omega_p/2\pi = 10$ Hz to 25 kHz. The proportional gain of the control loop is increased until the bandwidth stops increasing, and the integral gain is then increased until the transfer function is flat across its bandwidth (figure 2.5). The cutoff frequencies for H2, H1, and AM are 5.3, 2.3, and 5.0 kHz, respectively (table 2.3). By further optimizing the feedback loops the bandwidth might be increased [113, 115, 116].

The measurement of the FM-KPFM transfer function is complicated by the presence of the topographical feedback signal near the KPFM signal, which causes V_K to include an extraneous, rapidly oscillating voltage (see equation 2.17). The separation between the KPFM signal and the interfering topography signal is equal to the ω_A of FM-KPFM, which here is 2 kHz, quite typical for FM-KPFM [86, 87].

First the transfer function is measured with only the lock-in amplifier's own low-pass filter, but the extraneous voltage is so large that it overwhelms the signal until the frequency of the low-pass filter is decreased to 700 Hz, giving $\omega_c/2\pi \approx 400$ Hz. However, the extraneous voltage imprinted by the topography signal remains ≈ 400 mV, prohibitively large for practical measurements. Second, a notch filter is placed on the lock-in amplifier at $\omega_A/2\pi$ (2 kHz) in order to further mitigate V_E^T. The notch filter both decreases V_E^T, and also allows the filter on the lock-in amplifier to be increased to 1 kHz. In this configuration the cutoff frequency of FM-KFPM is determined to be $\omega_c/2\pi \approx 820$ Hz.

To investigate how ω_c translates into imaging speed, a few-layer graphene (FLG) flake is scanned with H- and FM-KPFM while the line scan speed is increased from 1 Hz to 79 Hz, over a 1×1 μm area with 256×256 pixels with $A_T = 16$ nm (figure 2.6). By 4 Hz (48 s per frame), FM-KPFM shows stripes. To investigate the cause of these stripes, the FLG is imaged without the aforementioned notch filter at 2 kHz. At 8 Hz, the amplitude of the stripes is < 0.3 V with the notch filter, but rises to > 1.5 V when the notch filter is removed. Thus the signal V_E^T does contribute to the stripe artifact, although the details of the feedback loop likely influence the stripes as well. At higher frequencies, the FM feedback loop oscillates wildly near the edges of the FLG.

With H-KPFM, on the other hand, clear contrast is maintained up to 16 Hz (16 s per frame), and at higher frequencies some contrast is maintained. However, the topographical feedback loop stops tracking the surface, and topographical inconsistency affects the potential image. At 79 Hz, patches on the graphene flake are

no longer visible. A similar limitation due to topographical feedback loop speed is reported in [74].

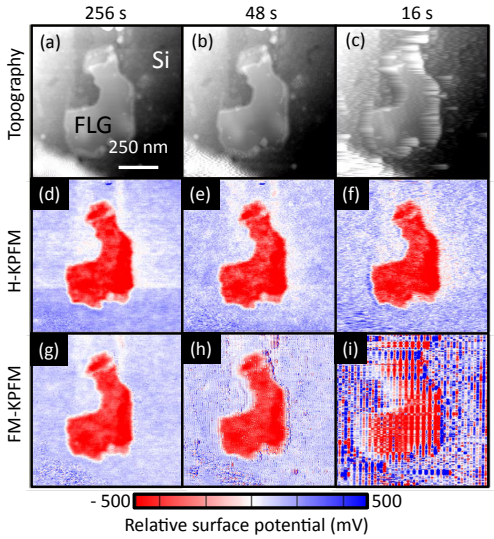

Figure 2.6: Images show the affect of increasing scan speed. (a-c) Topography images of the few layer graphene (FLG) become blurred. (d-f) H-KPFM allows the potential of FLG to be imaged with increasing speed and minimal distortion. (g-i) The topography oscillation is imprinted on the potential image when the bandwidth is increased if FM-KPFM is used. Topography scanning may be the primary speed limit. The height of the FLG is ≈ 2 nm. All scans are 256×256 pixels.

Table 2.3: Resolutions that characterize KPFM

Resolution	Figure of Merit	Definition	H2	H1	FM	AM	(units)
Time*	$t_c = 1/\omega_c$	Closed-loop 3 dB cut-off time [113]	0.19	0.43	1.2	0.20	ms
Voltage**	V_m	$V = V_K + V_0$ for which signal = noise [66]	73	41	96	2.0	mV
Space**	l_{10-90}	Distance from boundary over which voltage changes from 10% to 90% [87]	45	42	49	68	nm

*At $A_T = 8$ nm, $V_{AC} = 1$, $V_p = 1$ V, and at the surface, with topographical feedback on
**At $A_T = 8$ nm, Bandwidth = 200 Hz, V_{AC}=1 V, and lift height 11 nm

2.3.2 Voltage resolution

Whereas the tip apex detects the potential directly beneath it, the inclusion of stray capacitance from the cantilever results in surface potential spatially averaged over many microns (about the width of the cantilever) [75, 78–80]. The unknown and varying relative capacitances of the tip apex and cantilever limit AM-KPFM to qualitative contrast in most conditions [75, 78]. Both H-KPFM and FM-KFPM mitigate the stray capacitance effect through their dependence on C'' rather than C' [80, 86]. Here the stray capacitance must be assessed in order to understand the relation between the measured potential sensitivity and the ability to actually distinguish between two nanoscale objects. The capacitance of tip and cantilever

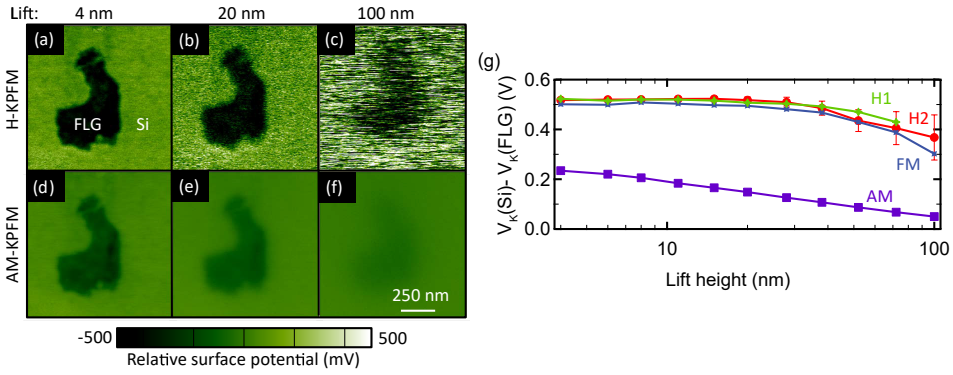

Figure 2.7: The voltage contrast between a few layer graphene (FLG) flake and Si substrate reveals the stray capacitance effect. (a-c) The voltage contrast between (few-layer) graphene and silicon changes little as the probe height increases from 4 to 100 nm for H-KPFM. (d-f) However, for AM-KPFM, the contrast at 100 nm differs by a factor of five from that at 4 nm. (g) A comparison between the four different KPFM methods shows that methods that depend on C'' more accurately represent the potential contrast than AM-KPFM, which depends on C'.

changes with tip-sample separation, and consequently, so does the measured average voltage contrast between the FLG flake and Si substrate, ΔV. The correspondence

between the actual and measured potentials is tested by observing the change of ΔV with lift height, akin to [117]. At closest approach the tip apex capacitance dominates. As the tip-sample separation is increased, ΔV changes little until the proportion of capacitance due to the apex decreases to a value comparable to the cantilever capacitance contribution. The criterion of $\frac{\mathrm{d}\Delta V}{\mathrm{d}d} \approx 0$ near the surface is adopted to ensure that the apex contribution dominates. In the limit of large lift height, the cantilever contribution dominates, and no potential contrast is observed. The potential contrast is estimated for each height by calculating the difference between the average potential inside the FLG/silicon boundary (figure 2.11e) and the average potential outside.

The contrast between Si and FLG changes little for H- and FM-KPFM, as the cantilever lift height is varied (figure 2.7a-c,g). On the other hand, the AM-KPFM detected voltage contrast changes by a factor of five as the lift height is decreased from 100 to 4 nm (figure 2.7d-f,g). Thus the average potential contrast measured with C'' methods is more accurate than the contrast measured by AM-KPFM.

The minimum detectable voltage, V_{m}, is the tip-sample voltage difference at which the signal is equal to the noise [64,66,104,106]. Here $N(B)$ is the noise power in the signal $S^{\mathrm{I}}_{\mathrm{LIA}}$ within the bandwidth B. The minimum detectable voltage for any KPFM method is:

$$V_{\mathrm{m}} = \frac{\sqrt{N(B)}}{\zeta_j}. \tag{2.18}$$

Note that $N(B)$ increases as the bandwidth increases. Thus increasing temporal

resolution restricts voltage resolution.

The sources of noise in an AFM can be divided into three categories [118]. The first, detection noise, includes angular fluctuations of the light beam and optical shot noise. The second, displacement noise, includes the reaction of the topography feedback loop to perturbations, such as 60 Hz line noise or the voltages applied in KPFM. The third, force noise, includes Brownian motion and stresses caused by light optical intensity fluctuations. Because ω_{D} is near a resonance in H-KPFM, we assume Brownian motion is the dominant force noise. In this limit, the total noise in the signal is:

$$N(B) = \frac{1}{2}\int_{-B}^{B}\left[\frac{2\gamma_i^2 k_i k_{\mathrm{B}} T}{\pi\omega_i Q_i}|G(\omega_i+\omega)|^2 + n_{\mathrm{det}}^2(\omega) + n_{\mathrm{dis}}^2(\omega)\right]\mathrm{d}\omega, \tag{2.19}$$

where the first term in the brackets represents the noise due to Brownian motion of the cantilever [119], k_{B} is Boltzmann's constant, T is temperature, n_{det} is the detection noise amplitude spectral density (which is nearly constant over the integral), and n_{dis} is displacement noise amplitude spectral density (which depends on the specifics of KPFM operation). If we consider only the Brownian motion of the cantilever, and assume the detection bandwidth B is less than the bandwidth of the cantilever ($B < \omega_i/2Q_i$), then the integral in equation 2.19 can be computed

analytically:

$$N(B) \approx \frac{\gamma_i^2 k_{\mathrm{B}} T}{\pi k_i} \arctan\left(\frac{2Q_i B}{\omega_i}\right), \tag{2.20}$$

yielding the same noise as used in previous calculations of V_{m}, in the limit of small B [66].

To understand how cantilever characteristics affect the minimum detectable voltage, each eigenmode of $G(\omega)$ is modeled as a point mass harmonic oscillator [120]. Then the minimum detectable voltage becomes:

$$V_{\mathrm{m,H}} = \frac{2\sqrt{2k_{\mathrm{B}}T}}{\sqrt{\pi} A_{\mathrm{T}} V_{\mathrm{AC}} C''} \sqrt{k_i \arctan\left(\frac{2Q_i B}{\omega_i}\right)}. \tag{2.21}$$

Conversely, if the dominant noise source is broadband detector noise (*e.g.* off-resonance), then $N(B) \approx n_{\mathrm{det}}^2 B$. The minimum detectable voltage when detector noise dominates is:

$$V_{\mathrm{m,H}} = \frac{2n_{\mathrm{det}}\sqrt{B}}{A_{\mathrm{T}} V_{\mathrm{AC}} C''} \frac{1}{|G(\omega_{\mathrm{D}})|\gamma(\omega_{\mathrm{D}})}. \tag{2.22}$$

Note that the optical lever sensitivity depends on the eigenmode excited (a cantilever bends more for the same d displacement if excited at higher eigenmodes [121]).

The minimum detectable voltage, V_{m} is experimentally determined by measuring the signals at the lock-in amplifier, S^{I} and S^{Q} (equation 2.5), with the feedback loop open. The detection phase, ϕ_{D}, is swept from -180° to 180° at V_{K} = -1, -0.3, 0.3, and 1 V. For each ϕ_{D}, the sensitivity ζ_j is determined by fitting S^{I} vs $(V_{\mathrm{K}} + V_0)$ to a

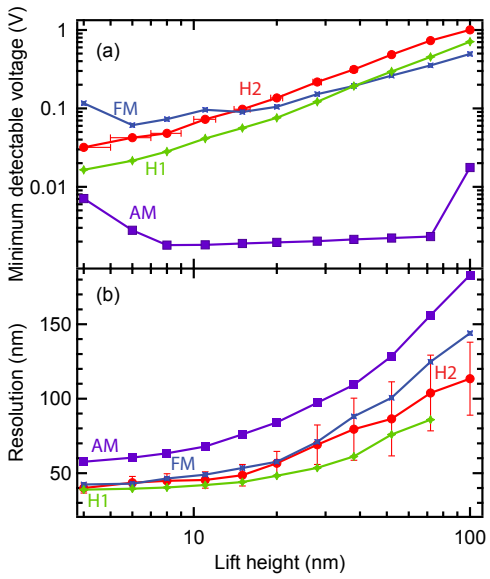

Figure 2.8: The (a) minimum detectable voltage and (b) 10-90 resolution both increase with lift height, for all methods. The data plotted here are for cantilever topographical oscillation of $A_{\mathrm{T}} = 8$ nm. Both heterodyne methods achieve resolutions similar to FM-KFPM.

line, the slope of which is ζ_j (equation 2.1). Calculating ζ_j for several ϕ_{D}, allows us to account for a small systematic offset on the output of the LIA, and to determine the ϕ_{D} that maximizes ζ_j. The noise at the output of the LIA is sampled at 5 kHz, and the calculations here consider the noise within a bandwidth of 200 Hz. Then equation 2.18 is used to calculate V_{m}.

The lift-height dependence of V_{m} for FM- and H-KPFM is measured. For each lift height, a force curve is used to set the position at the chosen lift height, where the probe is held for the duration of the V_{m} measurement. As the separation is increased, V_{m} increases, for all implementations (figure 2.8a). AM-KPFM has the smallest minimum detectable voltage; however, the small V_{m} is a consequence of the stray capacitance of the cantilever, which causes potential contrast to only be qualitative, and limits spatial resolution [75, 87]. Within H2, V_{m} increases more

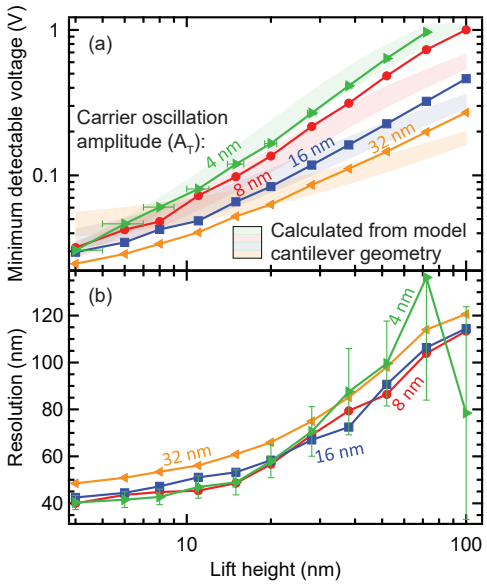

Figure 2.9: With H-KPFM in the H2 implementation, (a) the minimum detectable voltage, V_{m}, and (b) the 10-90 resolution, l_{10-90}, both increase with lift height. Larger shake amplitude, A_{T}, decreases V_{m}, but no effect on resolution is found above the noise level as a function of A_{T}. A cantilever model is used to calculate expected V_{m} (shaded regions).

quickly with lift height for smaller A_{T} (figure 2.9a). In addition, V_{m} is calculated from a model cantilever geometry [78] combined with noise from equation 2.20 for the cantilever described in table 2.1, where the tip radius and opening angle are the only free parameters. A tip radius of 16 ± 2 nm with an opening angle of $40 \pm 5°$ is found to approximate the $A_{\mathrm{T}} = 4$ nm data. The calculated V_{m} for this geometry, for all A_{T} are plotted in figure 2.9.

Similarly, we measure V_{m} while in tapping mode, as the topographical setpoint is gradually decreased. The noise in both H-KPFM implementations increases slowly as the setpoint is decreased, but the noise density in FM-KPFM increases rapidly, so that close to the surface, V_{m} for FM-KPFM is about an order of magnitude larger (figure 2.10). Because the noise does not increase as rapidly for H1, the source of the

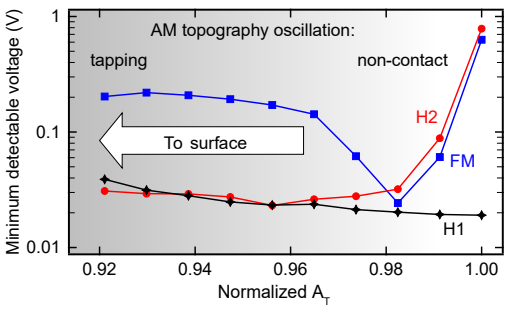

Figure 2.10: The minimum detectable voltage changes as a function of the normalized A_{T}, which decreases as the probe moves closer to the surface (as in figure 2.4). A smaller setpoint moves the cantilever closer to the surface. Far from the surface H2 and FM-KFPM have similar V_{m}, but it becomes much greater for FM-KPFM nearer the surface, where the noise increases. The H1 method uses a different eigenmode for topography, and does not have the steep increase in V_{m}. The gradient from dark to light represents the change from tapping mode to a non-contact mode as the topography setpoint is increased and the probe is lifted from the surface.

noise is not solely due to using the first resonance for KPFM detection. Likewise, because the rapid noise increase is not seen in H2, the source of the extra noise is not solely due to which resonance is used for topography control. Thus, we suspect that the rapid increase in noise when FM-KPFM approaches the surface is due to signal detection (ω_{D}) and topography control (ω_{T}) utilizing the same eigenmode.

2.3.3 Spatial resolution

Determining the spatial resolution of KPFM typically involves observing potential change around a boundary. Jacobs *et al.* showed that the boundary between two micron-scale objects allows for a clear empirical definition of spatial resolution and calculated a 25-75 resolution, *i.e.* the distance over which 50% of the total observed voltage change occurred, as a function of lift height [75, 122, 123]. Zerweck *et al.* similarly calculate a 10-90 resolution [87]. An equation for the resolution from

a point probe is derived in [123]. Others have sought information about the resolution by comparing the boundaries to particular functions, such as arctangent [123] or Boltzmann functions [124].

Here we estimate a 10-90 resolution, $l_{10\text{-}90}$, by fitting the measured potential as a function of distance from the boundary to a hyperbolic tangent (tanh, figure 2.11). The theoretically expected form of the measured potential near the boundary is very nearly a tanh within the proximity force approximation, as shown in section 2.3.3.1. For large lift heights (> 20 nm), the resolution is large enough to prevent V_{K} from reaching its asymptotic value over the scan size, which necessitates the use of a fit. The noise inherent in KPFM is overcome by averaging around the boundary. The equation of the tanh fit to the boundary is:

$$\overline{V_{\mathrm{K}}}(x) = (V_b \tanh\left[\ln(9)(x - x_0)/l_{10\text{-}90}\right] + c)/2, \tag{2.23}$$

where V_b is the potential change across the boundary, $\overline{V_{\mathrm{K}}}(x)$ is the average measured V_{K} a distance x from the boundary, x_0 is the center of the boundary, and $l_{10\text{-}90}$ is the 10-90 resolution. This fit gives the empirical spatial resolution. In order to determine whether or not the measured potential on either side of the boundary corresponds to the actual potential difference, one must supplement this data with either theory [87] or knowledge of the accuracy of the detected voltage (as in figure 2.7).

Regions of few layer graphene and silicon are identified by watershed segmentation [125]. First, the image is median filtered in order to mitigate the effect of noise

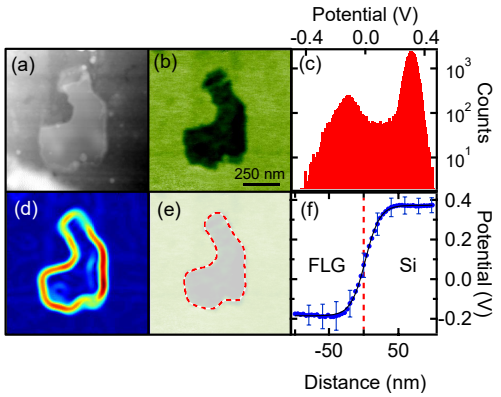

Figure 2.11: Few layer graphene on silicon shows (a) height contrast and (b) significant voltage contrast. (c) A histogram of the KPFM dat shows that the potential distribution is bimodal. (d,e) A watershed algorithm is applied to gradient magnitude of the potential image (d) in order to calculate the boundary (e, – – –). (f) Voltages are summed as a function of the distance from the boundary (•) and fit to a tanh function (black solid line), from which the 10-90 resolution is deduced.

on the algorithm, and the trace and retrace are averaged. Second, the gradient magnitude of the resultant potential image is calculated with a Sobel algorithm [125]. Third, points of lowest and highest potential across the image are marked. Fourth, the watershed algorithm is applied with the two marked points forming the origin of each basin (figure 2.11).

Once the image is divided into two components, we plot the potential of the unaltered measurement as a function of the distance from the estimated boundary, and fit the resulting curve to a tanh function (figure 2.11e,f). The 10-90 resolution, $l_{10\text{-}90}$, is then extracted from the fit.

For all KPFM methods used, $l_{10\text{-}90}$ increases with lift height (figures 2.8,2.9b), as observed before with AM-KPFM [75]. Both implementations of H-KPFM and FM-KPFM achieve better spatial resolution than AM-KPFM, at all heights, but the error is too large to discern a difference between the former three. However,

when the resolution approaches the length of the few layer graphene, or when the minimum detectable voltage reaches the contrast between the objects, the error grows large. Finding a longer, straighter boundary to measure, with larger contrast, could aid in future measurements of resolution at larger lift heights.

2.3.3.1 An equation for spatial resolution

Above we discuss the spatial resolution of KPFM in terms of $l_{10\text{-}90}$, the 10-90 resolution, or the distance over which 80% of the voltage change across a boundary occurs. We determine $l_{10\text{-}90}$ by fitting $V_{\mathrm{K}}(x)$, the potential measured across a boundary, to a hyperbolic tangent (equation 2.23).

Here, we use the proximity force approximation (PFA) for a sphere interacting with a plate to derive an analytic expression for $V_{\mathrm{K}}(x)$ for both C' and C'' KPFM methods. Furthermore, we demonstrate that the tanh function approximates the form of $V_{\mathrm{K}}(x)$ better than the arctan function in order to motivate our choices in the text. Finally, we estimate how $l_{10\text{-}90}$ changes with height and tip radius. We note that an equation for resolution exists in the large separation, small probe limit [123], but better resolution is achieved with small tip-sample separation, and so that is our focus here.

The PFA for the capacitive force of a sphere above a plate can be written as [126]:

$$F(d) = \frac{\epsilon_0}{2} \int_0^{2\pi} \mathrm{d}\phi \int_0^R r dr \frac{(V - V_{\mathrm{pl}}(r,\phi))^2}{(d + r^2/2R)^2}, \tag{2.24}$$

where R is the radius of the sphere, $V_{\rm pl}(r,\phi)$ is the potential of the plate at position (r,ϕ), and V is the potential of the sphere (here assumed to be spatially uniform). The voltage applied to the probe that minimizes nth derivative of this force can be found by taking n derivatives with respect to d and one with respect to V,

$$\frac{\partial^{n+1}F(d)}{\partial V \partial z^n} = \frac{\partial}{\partial d^n}\left[\epsilon_0 \int_0^{2\pi} \mathrm{d}\phi \int_0^R r dr \frac{V - V_{\rm pl}(r,\phi)}{(d + r^2/2R)^2}\right]. \tag{2.25}$$

At the Kelvin probe voltage, $V = V_{\rm K}(x)$, for which the KPFM signal $S_{\rm K}$ vanishes, equation 2.25 vanishes as well. Near a boundary, the potential of the plate is $V_{\rm pl}(r,\phi) = V_b\Theta(\cos(\phi)+L/r)$, where $L = x - x_0$ is the distance between the location of the probe and the boundary and Θ is the Heaviside step function . The potential is V_b for $r\cos(\phi) > -L$ and 0 otherwise. To simplify the calculation, we define the function $\Lambda(z,R,L)$:

$$\begin{aligned}\Lambda(d,R,L) &= \int_0^{2\pi} \mathrm{d}\phi \int_0^R r\mathrm{d}r \frac{\Theta(\cos(\phi)+L/r)}{(d+r^2/2R)^2}, \\ &= R\left(\frac{2L\,\arctan\left(\sqrt{\frac{R^2-L^2}{L^2+2Rd}}\right)}{d\sqrt{L^2+2Rd}} + \frac{2R\,\arccos\left(-\frac{L}{R}\right)}{d(R+2d)}\right).\end{aligned} \tag{2.26}$$

For a KPFM method with a signal proportional to the $(n+1)^{\rm th}$ derivative of capacitance, the Kelvin probe voltage near a boundary is:

$$V_{\rm K}^{C^{(n+1)}}(L) = V_b \frac{\Lambda^{(n)}}{2\Lambda^{(n)}|_{L=0}}, \tag{2.27}$$

where $\Lambda^{(n)} = \frac{\partial^n \Lambda}{\partial d^n}$, and $C^{(n+1)}$ represents a method that depends on the $(n+1)^{\rm th}$

derivative of capacitance. For example, for AM-KPFM, the signal of which is proportional to C', the Kelvin probe voltage is:

$$V_{\mathrm{K}}^{C^{(1)}}(L) = V_b\Bigg[\frac{1}{2} + \frac{\arcsin\left(\frac{L}{R}\right)}{\pi} + \frac{L(2d+R)\,\arctan\left(\sqrt{\frac{R^2-L^2}{L^2+2dR}}\right)}{\pi R\sqrt{2dR+L^2}}\Bigg]. \tag{2.28}$$

It must be noted that the PFA only considers the contribution of the tip apex to the KPFM signal. In AM-KPFM the dominant contribution to the signal comes from the cantilever. At a boundary, equation 2.28 will predict the shape of $V_{\mathrm{K}}^{C^{(1)}}(x)$, but the V_b coefficient will be much less than the potential difference across the boundary because AM-KPFM only measures qualitative potential contrast [75].

For the C'' methods (H- or FM-KPFM) the minimizing potential equation is more complicated, and so it has been plotted in figure 2.12a. To facilitate data analysis, a simpler function can be used to approximate equation 2.27. Both arctan and tanh functions have the desired behavior: monotonic, odd around $L = 0$, and asymptotic to a constant as $L \to \infty$. The slope of $V_{\mathrm{K}}^{C^{(n+1)}}(L)$ is steepest at $L = 0$ and so fitting for small L is most important. Arctan and tanh are used to approximate equation 2.27 by matching the first derivative of each function to our exact analytic expression:

$$\begin{aligned} V_{\mathrm{tanh}}^{C^{(n+1)}} &= V_b\frac{\tanh(2a^{C^{(n+1)}}L)+1}{2}, \\ V_{\mathrm{arctan}}^{C^{(n+1)}} &= V_b\frac{\arctan(\pi a^{C^{(n+1)}}L)+\pi/2}{\pi}, \end{aligned} \tag{2.29}$$

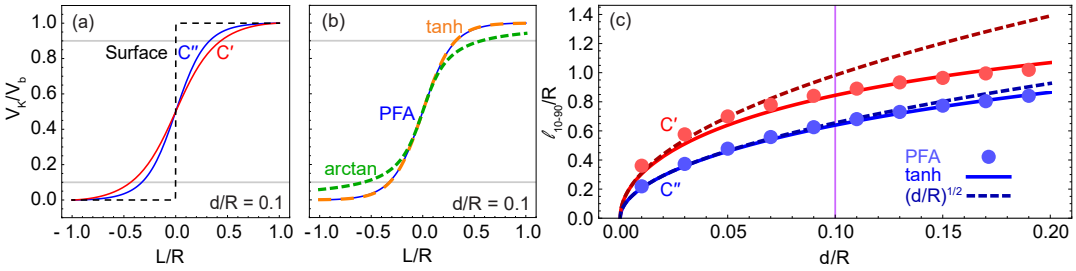

Figure 2.12: The normalized Kelvin probe voltage near a boundary in the proximity force approximation (PFA) is shown in (a) for both the AM-KPFM (C', red) and H- and FM-KPFM (C'', blue) variants. The dashed black line shows the normalized potential on the surface directly and two grey lines indicate the 10-90 potential change. (b) A tanh function (dashed orange) is a much better fit to the analytic expression (PFA) for the C'' method than an arctan function chosen in the same way (dashed green). (c) The 10-90 resolution predicted by a tanh function fit (solid) is compared to that calculated numerically by the exact PFA expression (•). At small d/R, the 10-90 resolution increases with separation $\propto \sqrt{d/R}$, and this approximate expression is plotted for both the C' and C'' methods (dashed). A purple line indicates the value of d/R for which (a,b) are plotted.

where,

$$a^{C^{(n+1)}} = \left.\frac{\partial V_{\mathrm{K}}^{C^{(n+1)}}}{\partial L}\right|_{L=0}, \tag{2.30}$$

Both functions are plotted in figure 2.12b to visually depict how well each fits equation 2.27. The tanh fit follows the exact expression more closely than the arctan fit. The tanh fit can then be used to estimate l_{10-90} as a function of d and R:

$$l_{10-90}^{C^{(n+1)}} = \frac{\ln(9)}{2a^{C^{(n+1)}}}. \tag{2.31}$$

Which, for AM-KFPM is:

$$l_{10-90}^{C^{(1)}} = \frac{\pi \log(81)\sqrt{dR}}{2\sqrt{d/R} + \sqrt{2}(2d/R+1)\arctan\left(\sqrt{\frac{R}{2d}}\right)}. \tag{2.32}$$

The more complicated expression of $l_{10-90}^{C''}$ is plotted in figure 2.12c. Taylor expanding around $\sqrt{z/R} \approx 0$, the resolutions are:

$$\begin{aligned} \frac{l_{10-90}^{C^{(1)}}}{R} &\approx \sqrt{2}\,\ln(9)\sqrt{\frac{d}{R}}\ \text{(AM method)}, \\ \frac{l_{10-90}^{C^{(2)}}}{R} &\approx \frac{2}{3}\sqrt{2}\,\ln(9)\sqrt{\frac{d}{R}}\ \text{(H-,FM- methods)}. \end{aligned} \tag{2.33}$$

Jump-to-contact limits how small d can become, and consequently limits the possible spatial resolution. These approximations are also compared to the exact PFA result in figure 2.12c.

The resolutions calculated here are a lower bound on the resolution possible with KPFM because many components of the probe that would broaden the resolution are neglected. Though the electrostatic probe-surface force from the tip cone and cantilever have been calculated for uniform potential [78, 127], we are unaware of any analytic procedure to take into account variations of the surface potential. A procedure does exist to calculate the electrostatic force between a sphere and a plate with potential variations [128], but the KPFM probe geometry is only slightly better represented by such a model. Most importantly, these extra cases all reduce to the PFA near the surface, where the best spatial resolution is achieved.

2.4 H-KPFM summary

In this chapter, we explore the versatility of H-KPFM and uncover its beneficial characteristics, the most prominent of which is its speed. The H1 implementation improves the minimum detectable voltage by $\approx 80\%$ relative to the original implementation. The next chapter discusses both our investigations into the effects of roughness and cantilever dynamics on H-KPFM and a generalization of the heterodyne actuation technique. Further studies into the technique of H-KPFM should investigate how to incorporate better control techniques for potential estimation (*e.g.* [115]) and tracking of the surface (*e.g.* [129]), which now limits KPFM scan speed. Cantilevers could be designed specifically for H-KPFM [130] to reduce the difference between the spring constants of the first and second eigenmodes, which would improve the sensitivity of H-KPFM. Likewise, cantilever resonance frequencies could be chosen to enable open-loop H-KPFM [99].

Heterodyne KPFM improves upon the time resolution of FM-KPFM. Rates of several frames per minute are achieved. Its speed is not limited by AC coupling or bandwidth overlap, and so with appropriate cantilevers it will operate even faster. It also improves upon the spatial resolution of AM-KPFM. These new implementations of H-KPFM will facilitate fast and accurate measurements of nanoscale potential dynamics. Most importantly, it provides a robust method for determining the force from patch potentials later in chapter 5.

Chapter 3: Utilizing cantilever dynamics in KPFM

This chapter tests and develops the KPFM methods described in chapter 2 using a more comprehensive model of the cantilever dynamics. The first half, adapted from a recent publication [108], tests how the tip apex trajectory interacts with the slope of a sample to affect the stability of the KPFM feedback loop. The second half explores how non-linearities in the tip-sample force can be used to improve the spatial resolution of KPFM, in order to calculate the patch potential force more accurately later in chapter 5. An improvement in spatial resolution is achieved, but is tied to a simultaneous loss in voltage contrast.

3.1 Lateral tip motion

In atomic force microscopy (AFM), the angle relative to the vertical (θ_i) that the tip apex of a cantilever moves is determined by the tilt of the probe holder, and the geometries of the cantilever beam and actuated eigenmode i. Even though the effects of θ_i on static and single-frequency AFM are known (increased effective spring constant, sensitivity to sample anisotropy, *etc.*), the higher eigenmodes used in multifrequency force microscopy lead to additional effects that have not been fully explored. Here we use Kelvin probe force microscopy (KPFM) to investigate how

θ_i affects not only the signal amplitude and phase, but can also lead to behaviors such as destabilization of the KPFM voltage feedback loop. We find that longer cantilever beams and modified sample orientations improve voltage feedback loop stability, even though variations to scanning parameters such as shake amplitude and lift height do not.

The development of specialized cantilever probes enabled atomic force microscopy (AFM) [34]. Later, it was realized that the holder tilts the cantilever and the trajectory of the tip apex which both increases the effective static spring constant and causes the phase of Amplitude Modulation (AM) AFM to be sensitive to both the anisotropy and slope of samples [131–134]. For higher eigenmodes i, the angle between the tip apex trajectory and the vertical axis (θ_i) also depends the geometries of the cantilever and eigenmode, so that recent experiments were able to use eigenmodes with different θ_i to probe forces in several directions [135–140]. Bimodal AFM, in which two eigenmodes are driven by excitation of the cantilever base, was used for most of these experiments, but it is only one of many multifrequency techniques [65, 66, 87, 104, 141–150], and the effects of θ_i have not yet been explored for the general multifrequency case.

Sideband multifrequency AFM methods are promising ways to investigate optoelectronic materials and devices at the nanoscale [65, 87, 104, 146–150]. In order to eliminate long-range artifacts and improve spatial resolution, they drive a signal by mixing a modulated tip-sample force with piezo-driven cantilever oscillations. A prominent sideband method is photo-induced force microscopy (PIFM), which has been used for nanoscale imaging of Raman spectra [146], nanoparticle reso-

nances [148], and refractive index changes [150]. However, there is considerable debate about how to extract quantitative data from PIFM scans [148–150] because it is unclear how the force couples into the probe and optical forces themselves are difficult to characterize *a priori*.

Because the electrostatic force is well-characterized and controllable compared to optical forces, it offers an opportunity to test the sideband actuation technique. The FM- and H-KPFM techniques introduced in chapter 2 are examples sideband AFM methods. In a recent experiment, height variation of around 10 nm destabilized the H-KPFM voltage feedback loop, but FM-KPFM scans were stable for variations of over 100 nm [151]. Because FM- and H-KPFM are primarily distinguished by the eigenmode used to amplify the KPFM signal, the cause of their qualitatively different behavior likely originates from the geometry of the eigenmodes. Moreover, the details of cantilever dynamics have been shown to be critical to understanding AM-KPFM [152, 153], a much simpler technique that drives and detects its signal at a single frequency, and which can be used for comparison. In this section, we use KPFM measurements to answer the questions: (a) how does the θ_i of each eigenmode affect the signals of KFPM, (b) why does the KPFM feedback instability differ between H- and FM-KPFM, and (c) how do the effects of θ_i appear in sideband multifrequency force microscopy methods in general?

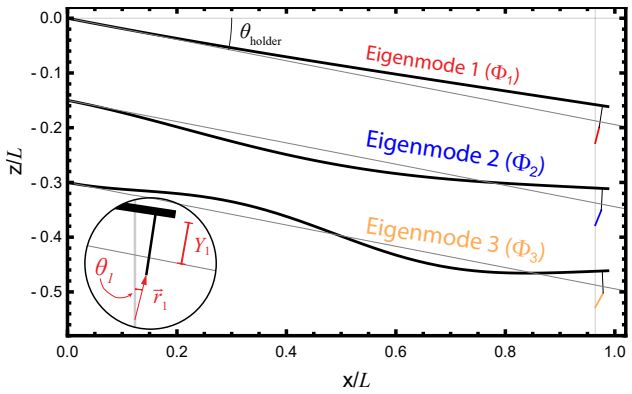

Figure 3.1: The tip apex moves at an angle relative to the vertical for each eigenmode i (θ_i), which depends on the angle of the probe holder (θ_{holder}), the geometry of the cantilever, and the geometry of the eigenmode (Φ_i). The inset shows the tip apex with the first eigenmode excited (i=1), in which the amplitude of the eigenmode (Y_1), the tip apex displacement ($\vec{r}_1$), and θ_1 are labeled.

3.1.1 Defining θ_i

The motion of a cantilever beam can be expressed as a sum of eigenmodes, each a solution to the Euler-Bernoulli beam equation [121, 154]:

$$z_{\text{cant}}(x,t) = \sum_{i=1}^{\infty} Y_i(t)\Phi_i(x), \tag{3.1}$$

where $Y_i(t)$ contains the time-dependence, Φ_i is the shape of the ith cantilever beam eigenmode (normalized so that $\Phi_i(L) = 1$, where L is the length of the cantilever beam), and z_{cant} is the displacement of the cantilever beam (see figure 3.1). To maintain generality, the exact form of Φ_i is not specified until the numerical evaluation of θ_i, at which point the solution for a rectangular cantilever beam is used [121, 154]. Thus the following analysis holds even for non-rectangular cantilever beams and probes with large tip cones, both which may have atypical Φ_i [155, 156].

To calculate the trajectory of the tip apex, the probe is characterized by its tip

cone height h, contact angle δ, and contact position x_t (figure 3.2). The position of the tip apex is the location of base of the tip cone $\{x_\mathrm{t}, Y_i\Phi_i(x_\mathrm{t})\}$ plus the position of the tip apex relative to the base of tip cone, $\{h\cos(\xi(Y_i)-\delta), h\sin(\xi(Y_i)-\delta)\}$, where $\xi(Y_i) = \tan^{-1}(Y_i\partial_x\Phi_i(x_\mathrm{t}))$ is the angle of the vector normal to the cantilever at x_t. Because the probe is held at an angle θ_holder (here, 0.2 radians), the displacement of the tip apex from equilibrium becomes, in the small oscillation limit ($Y_i \ll L$):

$$\vec{r_i} = \mathbf{R}\begin{bmatrix} h(\cos(\xi(Y_i)-\delta)-\cos(\delta)) \\ Y_i\Phi_i(x_\mathrm{t}) + h(\sin(\xi(Y_i)-\delta)+\sin(\delta)) \end{bmatrix}, \tag{3.2}$$

where $\mathbf{R} = \begin{bmatrix} \cos(\theta_\mathrm{holder}) & \sin(\theta_\mathrm{holder}) \\ -\sin(\theta_\mathrm{holder}) & \cos(\theta_\mathrm{holder}) \end{bmatrix}$ is a 2D rotation matrix around the base of the cantilever beam. For a single eigenmode in the $Y_i \ll L$ limit, the tip apex moves in a straight line at an angle with respect to the vertical:

$$\theta_i = \lim_{Y_i/L\to 0} \cos^{-1}\left(\vec{r_i}\cdot(Y_i\hat{z})\right). \tag{3.3}$$

Note that equations 3.2 and 3.3 imply that much of the trajectory of the tip apex is in the $\hat{x}$ direction, even for very small excitations. For example, a 10 nm amplitude excitation of the first eigenmode of the cantilever beam in figure 3.2b causes the tip apex to move ≈ 3.9 nm in the $\hat{x}$ direction and 8.6 nm in the $\hat{z}$ direction. Because the potential energy of an eigenmode must be the same whether the motion of the end of cantilever beam ($\Phi_i(L)$) or the tip apex ($\vec{r_i}$) is considered, an effective spring constant (k_i^eff) for forces acting on the tip apex parallel to $\vec{r_i}$ (perpendicular forces

excite only eigenmodes $\neq i$) can be defined [137]:

$$k_i^{\text{eff}} = \lim_{Y_i/L \to 0} \frac{Y_i^2}{|\vec{r}_i(Y_i)|^2} k_i, \tag{3.4}$$

where k_i is the spring constant for an upward force acting at $x = L$ [120].

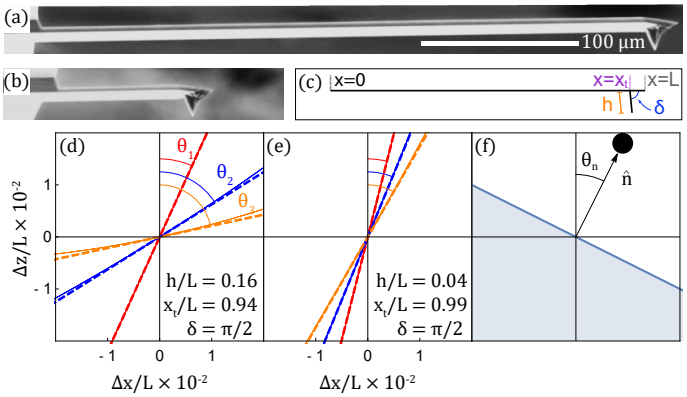

Figure 3.2: Cantilever geometry determines the direction of the tip apex motion. (a,b) SEM images show cantilevers of length 350 μm and 90 μm, respectively (μmasch, CSC37/Pt-B and NSC35/Pt-B). (c) Each cantilever is characterized by its tip cone height h, contact position x_t, contact angle δ, and length L. (d,e) The full calculation of $\vec{r}_i$ (solid line, equation 3.2) and linear approximation (dashed line, equation 3.3) show agreement. For each eigenmode, θ_i is greater for the short cantilever than for the long cantilever. (f) The slope of the sample is characterized by its normal vector ($\hat{n}$) and the angle it makes with the vertical (θ_n).

3.1.2 Lateral motion in multifrequency AFM

The tip apex trajectory affects AFM techniques that use a modulated tip-sample force $\vec{F}_{\text{dir}}$ to actuate the cantilever either directly or through sideband cou-

Table 3.1: Cantilever resonance frequencies

L (μm)	$\frac{\omega_1}{2\pi}$ (MHz)	$\frac{\omega_2}{2\pi}$	$\frac{\omega_3}{2\pi}$	$\frac{\omega_4}{2\pi}$	$\frac{\omega_5}{2\pi}$	$\frac{\omega_6}{2\pi}$	$\frac{\omega_7}{2\pi}$
90	0.25	1.62	4.58	-	-	-	-
350	0.02	0.13	0.37	0.72	1.20	1.79	2.50

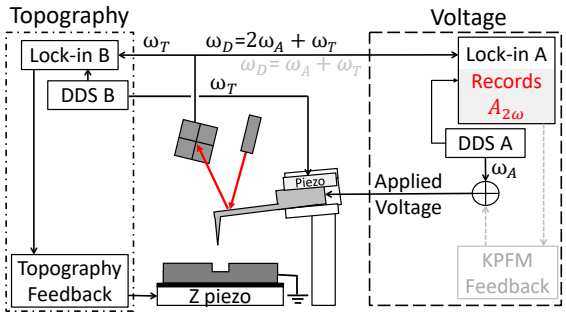

Figure 3.3: An AC voltage, V_{AC}, is applied to the cantilever at frequency ω_{A}, while tip-sample separation is controlled by piezo-driven oscillation at frequency ω_{T} and the sample is grounded. The oscillations at ω_{T} mix with the electrostatic force driven by V_{AC} at frequency ω_{A} to drive the tip apex at the detection frequency, ω_{D}, which is amplified by one of the cantilever's resonance frequencies and detected by a lock-in amplifier. When KPFM feedback is used, the grey signal paths are added to the circuit, and $\omega_{\mathrm{A}} = (\omega_{\mathrm{D}} - \omega_{\mathrm{T}})/2$ is changed to $\omega_{\mathrm{A}} = \omega_{\mathrm{D}} - \omega_{\mathrm{T}}$.

pling while relying on piezo-driven oscillation with amplitude A_{T} at frequency ω_{T} for topography control (here, $\omega_{\mathrm{T}} = \omega_1$ in table 3.1 is used). Sideband techniques generate a signal by modulating a separation-dependent force $\vec{F}_{\mathrm{dir}}$ at frequency ω_{M}, which is then mixed with the piezo-driven oscillations, typically A_{T}. Here, the resonance frequency used for detection determines the modulation frequency $\omega_{\mathrm{M}} = \omega_i - \omega_{\mathrm{T}}$ (table 3.1). By using the force gradient, sideband methods exclude the non-local effects of the cantilever beam that are present when $\vec{F}_{\mathrm{dir}}$ is used for direct actuation, such as in AM-KPFM [87, 104, 149].

To confirm that the cantilever beam's contribution to the total force is small even when higher eigenmodes are used, the force on the beam is computed for both direct actuation ($-\partial U/\partial Y_i$) and sideband actuation ($-\partial^2 U/\partial Y_i^2$), where U is the electrostatic potential energy between the probe and the surface evaluated using the proximity force approximation and the geometry of the longer probe. The contribution from the tip apex is calculated by modeling it as a 30 nm radius sphere

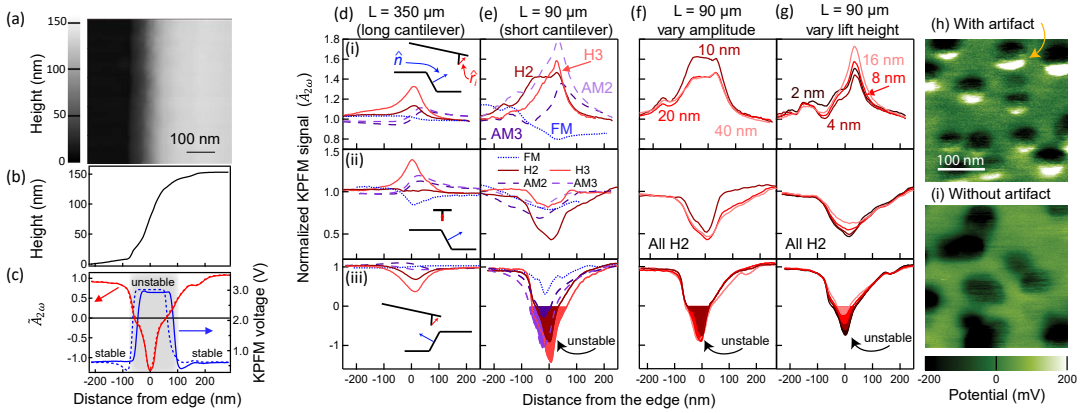

Figure 3.4: (a,b) The height of a trench that is scanned with KPFM (128^2 pixels, 500 nm/s). (c) Where the normalized signal ($\tilde{A}_{2\omega}$, red) becomes negative, the KPFM voltage with feedback on (blue) becomes unstable and approaches the limit imposed on the feedback loop, for both trace (solid) and retrace (dashed). Long (d) and short (e-g) cantilever beams scan across the trench edge in three different orientations: down (i, $\theta_n < 0$), parallel to (ii), and up the slope (iii, $\theta_n > 0$). In (i,ii), $\tilde{A}_{2\omega}$ remains positive for all methods, but in (iii) all methods except FM-KPFM contain a negative portion for the short cantilever beam. (f,g) Varying scan parameters such as A_{T} (used for topography control) and lift height are not sufficient to prevent $\tilde{A}_{2\omega} < 0$. The different scanning modes are labeled by a prefix (eg. 'H' for H-KPFM) and a number indicating the eigenmode used to amplify the signal, except for FM-KPFM, which always uses the first eigenmode. (h) An artifact is present in an H-KFPM scan of Au nanoparticles on indium tin oxide when the signal is amplified by the second eigenmode of the short cantilever beam. (i) When the long cantilever beam is used to scan other Au nanopaticles on the same sample, the artifact is eliminated.

10 nm above the surface. The percent of the signal originating from the cantilever beam using direct actuation is found to be 17-53% for the first seven eigenmodes, while with sideband actuation 0.1-0.2% of the signal originates from the beam. The small contribution from the beam validates the approximation that the electrostatic force acts on the tip apex for sideband actuation of higher eigenmodes.

In the small-oscillation approximation [65, 149], the force driving sideband

oscillation is $\vec{F}_{\text{side}} \cos(\omega_{\text{D}} t)$, where:

$$\vec{F}_{\text{side}} = \partial_d \vec{F}_{\text{dir}} \frac{A_{\text{T}}}{2} \cos(\theta_i - \theta_n), \tag{3.5}$$

in which d is the tip-sample separation, ω_{D} is the detection frequency, and the $\cos(\theta_i - \theta_n)$ factor originates from the angle between the trajectory of the tip apex and the force vector (parallel to $\hat{n}$). The displacement of the tip apex at ω_{D} is then $\vec{r}_j(t) = A_{\text{D}} \cos(\omega_{\text{D}} t)\hat{r}_j$, where eigenmode j is driven and the signal detected by the lock-in amplifier is:

$$A_{\text{D}} = \frac{Q_j}{k_j^{\text{eff}}} \vec{F} \cdot \hat{r}_j, \tag{3.6}$$

for both the sideband and direct driving forces (figure 3.3). A change in the sign of A_{D} corresponds to a phase shift by π radians.

The interplay of θ_j and sample slope can then be observed in the signal A_{D} normalized by the its value on a flat surface ($\tilde{A}_{\text{D}} \equiv \frac{A_{\text{D}}}{A_{\text{D}}(\theta_n = 0)}$):

$$\tilde{A}_{\text{D}}^{\text{dir}} = \frac{\cos(\theta_j - \theta_n)}{\cos(\theta_j)}, \tag{3.7}$$

$$\tilde{A}_{\text{D}}^{\text{side}} = \frac{\cos(\theta_n - \theta_j)\cos(\theta_n - \theta_i)}{\cos(\theta_j)\cos(\theta_i)}, \tag{3.8}$$

where it is assumed that $\hat{n}$ is in the x-z plane and $\theta_i, \theta_j \neq \pm\pi/2$. Note that if $|\theta_i - \theta_n| > \frac{\pi}{2} > \theta_i$, $\tilde{A}_{\text{D}}$ changes sign.

Equations 3.7 and 3.8 predict how the geometry of tip apex motion causes scanning probe methods to be sensitive to sample slope. To test the equations, a silicon trench is fabricated using e-beam lithography to pattern a 2 μm $\times$ 100 μm line on a silicon wafer which is then etched using reactive ion etching (RIE) and coated with 5 nm of chromium for conductivity. The edges of the trench are imaged, in attractive mode [157], trace and retrace images are averaged, and each column of pixels is summed and averaged (figure 3.4a,b).

3.1.3 Frequencies of electrostatic actuation

In the static limit, when an AC voltage is applied to a probe at frequency ω_{A}, the tip-sample electrostatic force has components at three frequencies [66, 87]: $\vec{F}_{\mathrm{es}} = \vec{F}_{\mathrm{DC}} + \vec{F}_{\omega_{\mathrm{A}}}\cos(\omega_{\mathrm{A}}t) + \vec{F}_{2\omega_{\mathrm{A}}}\cos(2\omega_{\mathrm{A}}t)$. Either $\vec{F}_{\omega_{\mathrm{A}}}$ or $\vec{F}_{2\omega_{\mathrm{A}}}$ can be used in equation 3.5 to drive the sideband signal by choosing $\omega_{\mathrm{M}} = \omega_{\mathrm{A}}$ or $2\omega_{\mathrm{A}}$, respectively. The signal then depends on the gradient of the original modulation force [87, 104]. For FM-KPFM, $\omega_{\mathrm{A}} \ll \omega_1$ [87]. Closed loop KPFM measures the contact potential difference between the probe and sample using a feedback loop to nullify a signal driven by the force $\vec{F}_{\omega_{\mathrm{A}}}$. Alternatively, open loop KPFM uses oscillation driven by $\vec{F}_{2\omega}$ combined with the $\vec{F}_{\omega_{\mathrm{A}}}$ signal to estimate the potential difference ΔV from the relationship between the forces $\vec{F}_{2\omega_{\mathrm{A}}} = \vec{F}_{\omega_{\mathrm{A}}} V_{\mathrm{AC}}/(4\Delta V)$ [98, 158]. The relationship between $\vec{F}_{2\omega_{\mathrm{A}}}$ (which drives $A_{2\omega_{\mathrm{A}}}$ according to equation 3.6) and KPFM feedback loop itself can be seen in figure 3.4c: the feedback becomes unstable at locations where $A_{2\omega_{\mathrm{A}}}$ changes sign. Moreover, any change in $A_{2\omega_{\mathrm{A}}}$ makes KPFM susceptible

to topographic cross-talk [84]. The signal is driven by $\vec{F}_{2\omega_A}$ because it reveals the behavior of the KPFM feedback loop, without requiring feedback to be used and is not susceptible to patch potentials or tip change.

3.1.4 Effect of θ_i observed by scanning a trench

The effect of slope is revealed by observing how the normalized signal ($\tilde{A}_{2\omega_A}$) changes as the tip apex approaches an edge of the trench at different orientations, for AM-, FM- and H-KPFM with the first three eigenmodes of each cantilever, and $V_{AC} = 3$ V. In figure 3.4 the trench edge is crossed with three different orientations: (i) the vector from the base of the cantilever beam to its tip apex points down the slope ($\theta_n > 0$, from the higher to the lower level) (ii) parallel to the slope ($\hat{n}$ out of plane) and (iii) up the slope ($\theta_n < 0$). One trend predicted by equation 3.8 is observed: $\tilde{A}_{2\omega_A}$ tends to increase as θ_n increases. However, the decrease of $\tilde{A}_{2\omega_A}$ is greater for the short cantilever beam than for the long cantilever beam. For the short cantilever beam, the $\theta_n < 0$ edge leads to $\tilde{A}_{2\omega_A} < 0$ for every technique except FM-KPFM.

Other scan parameters affect $\tilde{A}_{2\omega_A}$ much less. A_T, used for topography control, is varied from 10 to 40 nm, but the shape of $\tilde{A}_{2\omega_A}$ retains a negative portion as the $\theta_n < 0$ edge is crossed. Similarly, using a two-pass method and varying the lift height from 2 nm to 16 nm does not prevent $\tilde{A}_{2\omega_A} < 0$ at the $\theta_n < 0$ edge. Thus, if KPFM feedback is unstable for geometric reasons, adjustments to the scan settings do not typically stablize it.

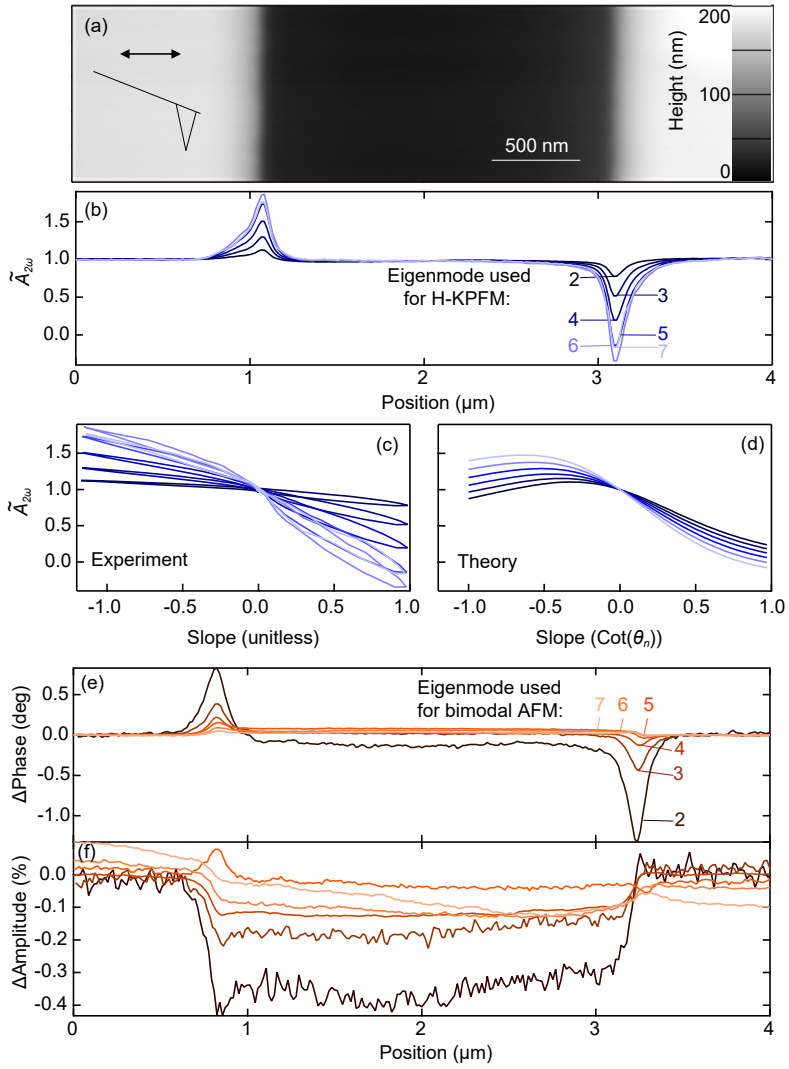

Figure 3.5: (a) A cantilever scans, using H-KPFM, across a 2 μm wide chromium-coated silicon trench (64×256 pixels, 800 nm/s). (b) On the downward slope (left), the normalized signal $\tilde{A}_{2\omega_A}$ becomes larger, but on the upward slope (right), the signal decreases. (c) Measured and (d) predicted values of $\tilde{A}_{2\omega_A}$ are plotted against the local slope of the trench. Higher eigenmodes tend to show a greater change with slope, as predicted from their larger θ_i. Bimodal AFM is also used to scan across the surface, while biased to 3 V. (e) The change in phase shows peaks at the edges, but unlike the H-KPFM case, the relative amplitude of the phase change decreases for higher eigenmodes, because the of increased k_i^{eff}. (f) The amplitude decreases in the middle of the trench, but not at the edges, and changes by $< 0.5\%$.

To test the predictions with a wider range of θ_i, the trenches are scanned again with the long probe in H-KPFM mode using the first eigenmode for topography control and amplifying the $\vec{F}_{2\omega}$ signal with eigenmodes 2-7 (ie. $\omega_{\mathrm{A}} = \omega_{\mathrm{M}}/2 = (\omega_i - \omega_1)/2$, so that $\omega_{\mathrm{D}} = \omega_i$ for $2 \leq i \leq 7$, table 3.1). Because each eigenmode has a slightly greater θ_i than the one before it (ie. $\theta_{i+1} > \theta_i$), equation 3.8 predicts that the effect of sample slope is greater for the higher eigenmodes than the lower ones, and the experiment confirms this trend, although the seventh eigenmode changes less than the sixth (figure 3.5b-d). The experimental data do not all fall on a single line (figure 3.5c), perhaps because the region on the sample from which the $\vec{F}_{2\omega}$ force originates deviates from the single-slope assumption.

For eigenmodes 3-7, the data agree better with equation 3.8, which has no free parameters, than with the null hypothesis that the signal does not depend on slope, thus confirming that the direction of the force affects how it drives the tip apex. However, equation 3.8 tends to underestimate $\tilde{A}_{2\omega_{\mathrm{A}}}$, particularly for slopes < -0.5, which suggests that other factors, such as the tip cone and changes to the piezo-driven oscillation, A_{T}, may also matter. An initial test of effect of slope on piezo-driven oscillation with bimodal AFM shows a change in the phase at the edges of the trench (figure 3.5e,f). Because the sideband excitation technique is similar for different forces, the results here indicate that θ_i affects the whole class of methods.

The direction of the tip apex trajectory depends on cantilever geometry and the eigenmodes used, and influences sideband multifrequency force microscopy methods. It can even change the sign of the signal, which leads to feedback instability in KPFM. The results here show that considerable topographic restrictions exist for

multifrequency methods when short cantilevers are used. Because short cantilevers enable faster scanning than long cantilevers [159], the restriction amounts to a speed limitation for any given roughness. Because the equations above separate the calculation of θ_i (3.1-3.4) from the analysis of the sideband signal (3.5-3.8), either portion can be combined with numerical methods to account for non-rectangular cantilever beams, or non-analytic forces. Knowledge of the effect of geometry will assist in the development of additional multifrequency methods and will make the interpretation of current methods more accurate. In particular, the improved stability of KPFM will enable high resolution voltage mapping of rough or textured surfaces, which will allow for improved nanoscale characterization of optoelectronic structures such as solar cells and for the study of light induced charging effects resulting from hot carrier generation or plasmoelectric excitation of nanostructured metals [148, 151, 160]. Moreover, the above experiments showed us that H-KPFM with the first cantilever eigenmode allows scanning on the spherical surface of Casimir force probes.

3.2 Tunable spatial resolution

The spatial resolution of dynamic force microscopy is limited primarily by three factors: tip geometry, jump-to-contact, and the separation dependence of the tip-sample interaction [64]. The first two of these factors can be controlled by either the choice of cantilever (tip radius, spring constant) or scan parameters (drive amplitude, setpoint). On the other hand, a few techniques have been used to control the signal separation dependence in particular situations, but no general method has

emerged.

A long-range force, like the electrostatic (d^{-1} for tip-plate) or van der Waals force (d^{-2}), interacts with a larger region of the AFM tip than a shorter range force, such as the contact force from the overlap of electron wavefunctions ($\approx d^{-12}$), and so limits the spatial imaging resolution. One successful technique to increase the separation dependence is to immerse a sample in liquid to minimize van der Waals force so that the repulsive contact force dominates tip dynamics [161]. However, this technique requires operation in liquid which lowers the cantilever Q-factor and a liquid environment may not be suitable for all samples. Another technique is to affix a dissimilar particle to the end of the tip (*e.g.* atom, quantum dot, *etc*) [162–164], but stability on rougher surfaces and at ambient conditions has not been tested. Other methods that increase the separation dependence of the signal include frequency modulation or phase detection, which (in the small-amplitude limit) detect the force gradient instead of the force itself [85,147,165]. The idea of imaging force gradients, instead of forces, to increase spatial resolution has been further developed into a sideband technique, that can be used with any force that can be driven at $>$500 Hz [65, 87, 104, 147, 149].

In this section, a general technique is proposed to increase the separation dependence of a signal by mixing the oscillation of the cantilever at one (carrier) frequency with force modulation at another, in order to excite the cantilever at a third frequency, amplified by one of its eigenmodes (figure 3.6). The tunable spatial resolution (TSR) technique presented here is a generalization of sideband actuation that uses the nonlinearity of the tip-surface interaction to control the

spatial resolution. The scheme is demonstrated with Kelvin probe force microscopy [66, 87], and noticeable resolution enhancement is achieved. Concurrent changes to the noise level and the feasibility of extending the TSR technique to measure other forces are discussed.

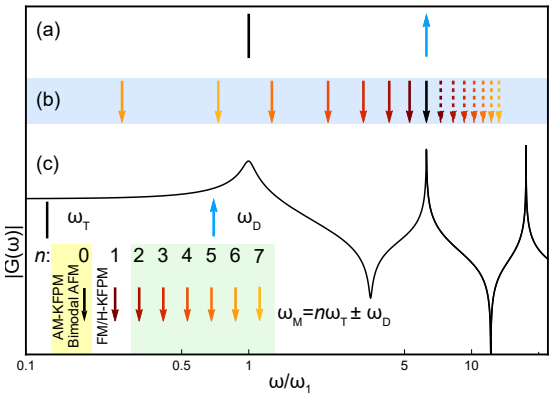

Figure 3.6: Applied and detected signals along the cantilever transfer function. (a) Frequencies are chosen for the carrier signal/topography control (ω_{T}, |) and signal detection (ω_{D},↑). (b) The different frequencies at which the force can be modulated to generate a signal at ω_{D} are determined by the equation $\omega_{\mathrm{M}} = n\omega_{\mathrm{T}} \pm \omega_{\mathrm{D}}$, where n chooses the term of a Taylor series expansion of the force used to generate the signal, which in turn determines its dependence on separation d. The arrows show different choices for ω_{M}. Solid arrows correspond to '$-$', dashed arrows correspond to '$+$', and the colors correspond to different n. (c) The cantilever transfer function $G(\omega)$ is used to amplify the signal.

We introduce a technique to improve the spatial resolution of the scanning force microscopy by altering the effective force on the cantilever. We motivate the technique mathematically by considering the electrostatic force and then demonstrate the technique with Kelvin probe force microscopy (KPFM). The spatial resolution is investigated by scanning a flake of few layer graphene, and the voltage contrast is investigated by measurements of the minimum detectable voltage. The spatial resolution is found to improve by almost a factor of two, while the voltage contrast decreases according to a perturbative model discussed below.

3.2.1 Modeling tunable spatial resolution

Tunable spatial resolution works by controlling the effective d-dependence of the signal. The vertical component of the force between a conductive probe and a conductive surface is $F = -\frac{1}{2}\partial_d C V^2$, where $\partial_d C = \frac{\partial C}{\partial d}$ is the tip-sample capacitance gradient and V is the (height-independent) voltage between the tip and the sample. The time-averaged tip-sample separation is maintained through feedback acting on photothermally driven oscillation of the cantilever at frequency ω_{T}. When the cantilever is interacting weakly with the surface (often called 'attractive mode') [157], its motion is approximately $d(t) = \bar{d} + A_{\mathrm{T}} \sin(\omega_{\mathrm{T}} t)$, where A_{T} is the amplitude of the cantilever and ω_{T} is the frequency of the oscillation used for topography feedback. The force on the cantilever, when Taylor expanded around its equilibrium position, is thus:

$$F_{\mathrm{es}} = -\frac{1}{2}\left(\sum_{n=0}^{\infty} \frac{\partial_d^{(n+1)} C}{n!}\bigg|_{\bar{d}} A_{\mathrm{T}}^n \sin^n(\omega_{\mathrm{T}} t) \right) V^2. \tag{3.9}$$

In KPFM, both a DC voltage (V_{K}) an voltage oscillating at frequency ω_{A} (V_{AC}) are applied to the probe. There is also an inherent contact potential difference, V_0, relative to the surface, so that $V = V_{\mathrm{AC}} \sin(\omega_{\mathrm{A}} t) + V_{\mathrm{K}} + V_0$. Then, V^2 has components at three frequencies: DC, ω_{A}, and $2\omega_{\mathrm{A}}$, as discussed in section 3.1.3. Initially, the force modulation frequency ω_{M} is chosen to be ω_{A}. To estimate the magnitude of the TSR signal, we make two more simplifying assumptions. First, we assume that

$\partial_d^{(n)} C > \partial_d^{(n+1)} C A_{\mathrm{T}}$ so that the signal at each frequency is dominated by the smallest n which contributes to it. Because $\partial_d C \propto d^{-1}$ near the surface, this assumption is equivalent to saying that $A_{\mathrm{T}}/\bar{d} < 1$. Second, we assume that the motion generated by the force at frequencies other than ω_{T} is small because they are not amplified by a cantilever resonance, so that our original equation for $d(t)$ remains valid, even when these extra forces are present. The magnitude of the force at frequency $|n\omega_{\mathrm{T}} \pm \omega_{\mathrm{A}}|$ is then:

$$|F_{n\omega_{\mathrm{T}} \pm \omega_{\mathrm{A}}}| = \frac{A_{\mathrm{T}}^n \partial_d^{(n+1)} C}{2^n n!} V_{\mathrm{AC}} |V_{\mathrm{K}} + V_0|, \tag{3.10a}$$

$$= \left(\frac{A_{\mathrm{T}}}{2\bar{d}}\right)^n |F_{\omega_{\mathrm{A}}}| \leq \frac{|F_{\omega_{\mathrm{A}}}|}{2^n}, \tag{3.10b}$$

where both the identity that $\sin^n(x) = 2^{-n} \sin(n(x - \pi/2) + \pi/2) + O(\sin(mx),\ m < n)$, and the proximity force approximation ($d/R \ll 1$) have been used. The inequality 3.10b is the same for the case when the electrostatic force modulation at $2\omega_{\mathrm{A}}$ is used (*i.e.* $\omega_{\mathrm{M}} = 2\omega_{\mathrm{A}}$).

Now ω_{M} is chosen so that the force to be amplified coincides with one of the eigenmodes of the cantilever (pictured in 3.6 as the second eigenmode), so that:

$$\omega_{\mathrm{M}} = |n\omega_{\mathrm{T}} \pm \omega_{\mathrm{D}}|. \tag{3.11}$$

The proximity force approximation (PFA) is used to predict how stronger distance dependence affects the spatial resolution. It states that near the surface, the force on a spherical probe can be approximated as if it were the force on many individual

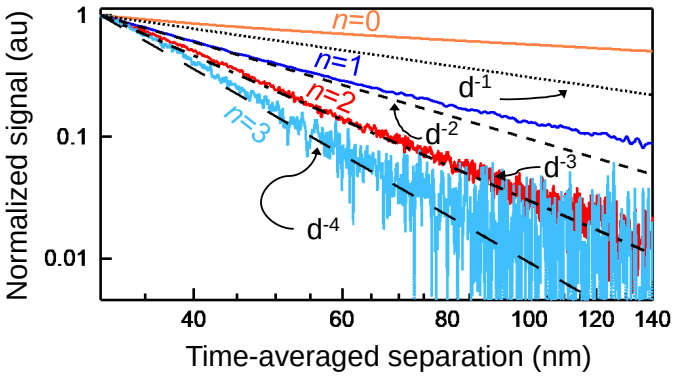

Figure 3.7: The power law that the KPFM signal follows depends on the harmonic (n) used to amplify the signal. When amplified by the nth order term of equation, the signal relies on the (n+1)th derivative of capacitance, so that in the proximity force approximation it follow a $d^{-(n+1)}$ power law. The signals of the first four n are shown as a function of separation for a 5 V driving voltage. Power laws in d are shown for comparison.

plates arranged in the shape of the sphere. In chapter 2, the PFA is used to derive the spatial resolution of a method using the $(n+1)^{\text{th}}$ derivative of capacitance (equation 2.27). Figure 3.7 shows how the effective separation dependence of the signal changes for n=0-3. By approximating the V_{K} at a boundary as a tanh function (section 2.3.3.1), the 10-90 spatial resolution (the distance over which 80% of the apparent voltage change occurs) can be written as:

$$l_{10-90}^{C^{(n+1)}} = \frac{\ln(9)}{2(\partial_x V_{\text{K}}^{C^{(n+1)}}(x))|_{x=0}}, \tag{3.12}$$

$$\implies l_{10-90}^{C^{(n+1)}} \overset{d/R\to 0}{=} \sqrt{2}\ln(9)\frac{(2^n n!)^2}{(2n+1)!}\left(\frac{d}{R}\right)^{1/2}, \tag{3.13}$$

$$\implies l_{10-90}^{C^{(n+1)}} \overset{d/R\to 0}{=} \left(1-\frac{1}{2n+1}\right) l_{10-90}^{C^{(n)}}. \tag{3.14}$$

Thus heterodyning the modulated force with a larger-n term of the Taylor series in equation 3.9 both improves spatial resolution and harms voltage sensitivity.

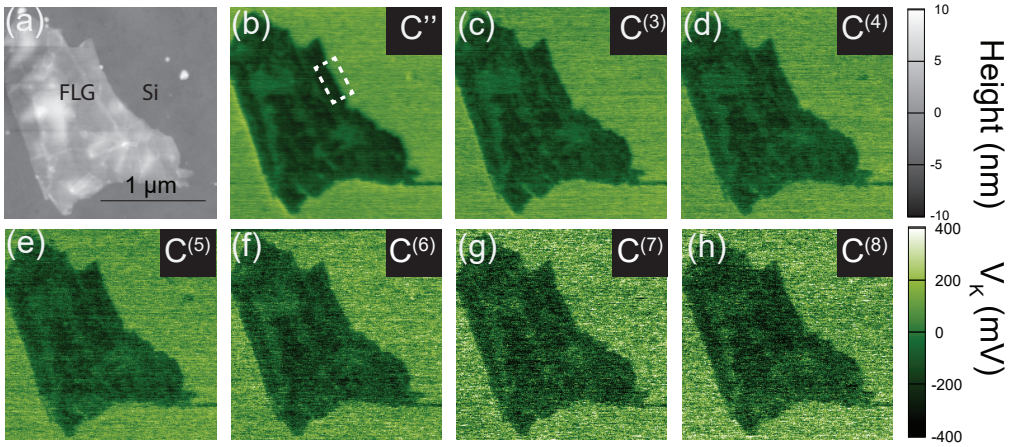

Figure 3.8: A flake of few layer graphene on silicon is scanned with KFPM using successively higher harmonics of the motion. The resolution improves, but voltage sensitivity decreases as higher-order derivatives of capacitance are used. The dashed white box in (b) shows the region later used to estimate spatial resolution.

Although it is not always possible to change the tip radius used for imaging, it is a useful comparison for the changes in resolution discussed above. In equation 3.10b, increasing n by 1 cuts the force, and hence the sensitivity, in half. Because force is proportional to radius in the PFA, this would be equivalent to halving the probe radius. Now, when d«R, the spatial resolution is $\propto \sqrt{R}$ (equation 3.13), so halving the radius leads to a $\approx 29\%$ improvement in spatial resolution. The improvement in spatial resolution due to increasing n is $1/(2n+1)$ (equation 3.14), so the first few improvements are $\approx 33\%, 20\%, 14\%$ and so on. Thus, in the PFA limit, raising n causes a comparable change in both spatial resolution and sensitivity as changing R. Raising n changes only the effective force at the detection frequency, but does not change the time-averaged force on the probe, and so does not prevent jump-to-contact as reducing the probe radius would. However, it is not always possible to change the probe radius. In air the radius of a metal-coated probe is typically limited to ≥ 20 nm, and changing the probe requires unloading the cantilever, which

could disrupt an experiment. For these reasons, TSR is competitive and, in many situations, preferable to choosing a tip with a smaller radius.

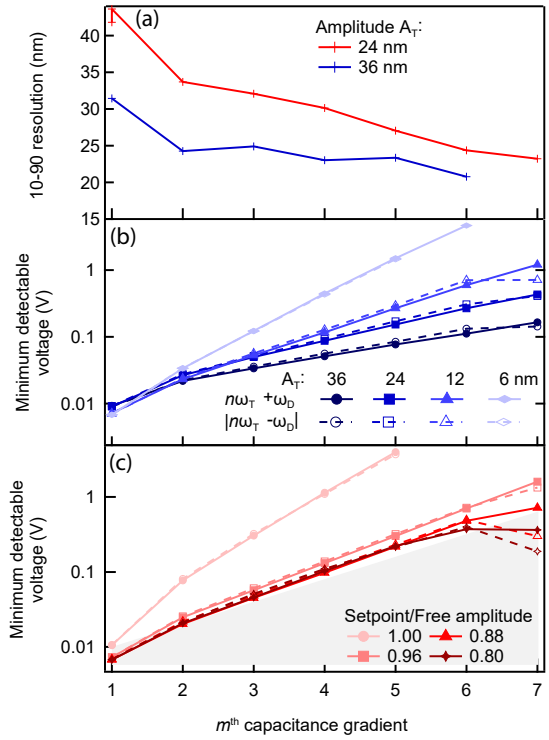

Figure 3.9: (a) Some change in the resolution is observed with TSR-KPFM, but not as much as is predicted by the PFA (equation 3.14), possibly because the boundary itself has an inherent width. (b) The minimum detectable voltages increases for a similar amount for each increase in n, and that amount depends on the A_T. (c) Changing the topography setpoint changes $\bar{d}$, which in turn can drastically change the sensitivity.

The 10-90 spatial resolution (l_{10-90}) is determined by imaging a 200 nm long edge on a piece of few layer graphene (FLG) on doped silicon (the boxed area in figure 3.8). For these measurements, a platinum-coated HQ:NSC35/Pt-A probe (μmasch) is used. The topographical oscillation is excited photothermally, rather than piezoelectrically, for a more stable transfer function. The 10-90 resolution is then calculated by fitting the potential as a function of its distance to a boundary to a tanh function, as discussed in chapter 2. Oscillation amplitudes of 6, 12, 24,

and 36 nm are used for the topographical feedback. For the 6 and 12 nm amplitudes, spatial resolution measurements are not shown, because stable scanning is not achieved. For 24 and 36 nm oscillation amplitudes, noticeable improvement in resolution is measured, though not as significantly as predicted by the PFA (figure 3.9a). The discrepancy could be caused by the oscillation amplitude of the probe (not considered in the PFA), the finite width of the FLG-Si boundary, or by the validity of the PFA at small separations. The V_{m} increase consistent with the $(2\bar{d}/A_{\mathrm{T}})^n$ proportionality of equation 3.10b (figure 3.9b,c). Using a larger shake amplitude reduces the loss in sensitivity, possibly because it allows for a greater $(A_{\mathrm{T}}/\bar{d})$ without jump-to-contact (figure 3.9b). However, the V_{m} measurements are sensitive to the setpoint amplitude at which KPFM is operating. For the same free amplitude (≈ 13 nm), the V_{m} changes drastically as the setpoint amplitude is changed (figure 3.9c).

The minimum detectable voltage (V_{m}) is measured for n ranging from 0 to 6 (figure 3.9). The connections of each lock-in amplifier (LIA) are identical to [65], and the relative phase is tuned between them in the same way. The V_{m} measurements are made by sweeping V_{K} from -1.5 to 1.5 V, across the force minimum, with 20 different relative phases settings between $-\pi$ and π on LIA, each collected for 1 s. The minimizing voltage is then, $V_{\mathrm{m}} = N/\zeta$, where N is the measured noise (in mV) in a 200 Hz bandwidth, and ζ is the KPFM sensitivity, as described in section 2.3.2.

One of the advantages of the TSR method is that it allows amplifying several signals through the same cantilever resonance. For example, open loop (OL) TSR-KPFM is achieved by applying two different AC voltages (figure 3.10). The frequencies used for the two voltages are chosen so that the $F_{2\omega}$ signal from the first

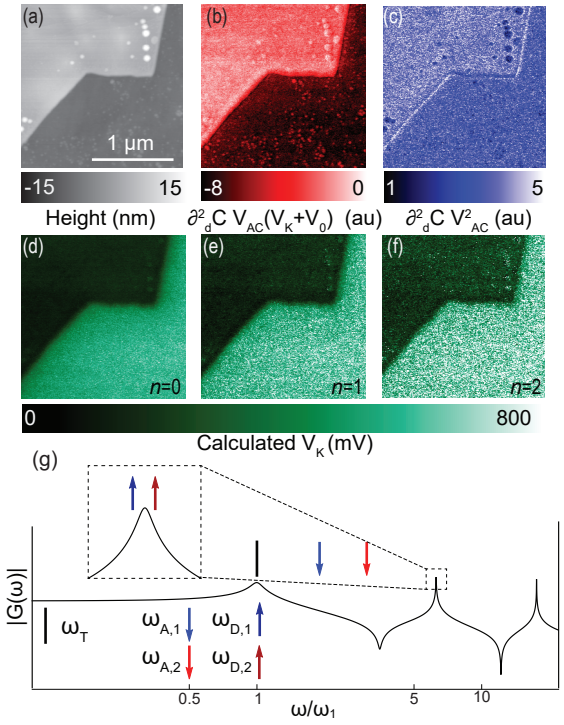

Figure 3.10: Open loop TSR-KPFM is performed on a flake of FLG on Si. (a) The topography shows the FLG in the upper-left corner. Separate AC voltages actuate the signal originating from (b) F_ω and the signal originating from (c) $F_{2\omega}$. The ratio of (b) to (c) can then be related to the potential difference, which is shown in (d-f) for n=0-2. (g) Both signals are amplified by the same eigenmode.

voltage and the F_ω signal from the second are amplified by the same resonance. The potential difference between the tip and sample is then calculated from the ratio of the two signals [98, 99]. The advantage of an OL KPFM implementation is that it avoids the low-frequency bias voltage associated with closed loop KPFM, which can alter surfaces such as semiconductors or batteries.

The TSR technique is possible to implement with any long-range tip-surface force which can be modulated externally. Recent experiments show that it is possible to use the sideband technique, from which TSR is generalized, with magnetic and photo-induced forces as well as the electrostatic force [147, 149]. Moreover it is

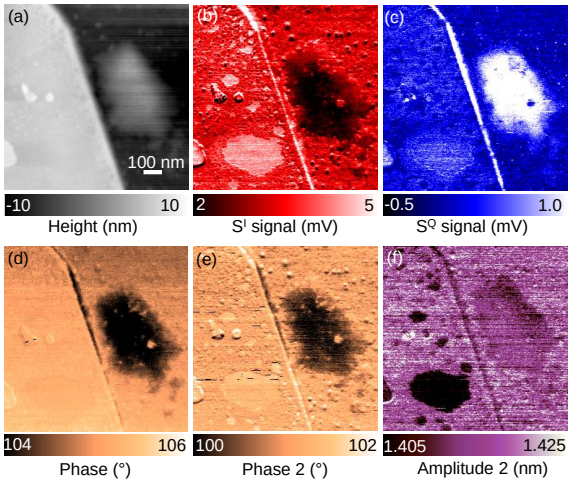

Figure 3.11: (a) The FLG topography is measured with standard amplitude modulation feedback on the oscillation at frequency ω_{T}. The cantilever is shaken at frequency $\omega_{\mathrm{M}} = \omega_2 - \omega_{\mathrm{T}}$ piezoelectrically at an amplitude of ≈1.4 nm. (b,c) The mixing of the oscillations at ω_{T} and ω_{M} generates another signal at ω_2, which is divided into in-phase (S^I) and quadrature (S^Q) components at the lock-in amplifier. (d) The phase of the ω_{T} shows similar contrast to S^I and S^Q (d). (e,f) The phase and amplitude of a second scan using bimodal AFM show similar regions of contrast.

expected that other forces present at the nanoscale, such as van der Waals/Casimir forces, can be modulated as well [49, 50, 166–168]. The total tip-sample force can even be modulated implicitly, by modulating the tip-sample separation [21]. The separation is modulated here by shaking the cantilever directly at ω_{M} to mix the modulated force with the oscillations at ω_{T}. It has been known for some time that the nonlinear tip-sample force excites the cantilever at additional frequencies [169], but the TSR technique clarifies how to amplify the signal. A preliminary test of implicitly varying the tip-sample force is compared to bimodal AFM by scanning FLG (and adhesive residue) on Si (figure 3.11). The resolution enhancement is not clearly observed for implicit force modulation, but developing a procedure to convert the signal to a force, as has been done for other AFM techniques [63, 170, 171], should

clarify what resolution control is possible. Furthermore, because the tip-trajectories of different cantilever eigenmodes are in different directions (previous section), implicitly varying the force with TSR allows one to drive and probe the force along different axes, unlike typical bimodal AFM. The TSR technique presented here will enable better resolution control with modulated tip-sample force. Even though the increase in resolution is small, it will be critical in situations where it is necessary to tease out the effect of probe resolution, such as in the estimation of surface potential autocorrelation functions [109, 172].

Chapter 4: Casimir force measurements in air

4.1 Introduction

The Casimir force has long been a theoretical marvel. The simplicity of its original derivation lends itself to pedagogy [1], while the comprehensiveness of the Lifshitz formulation extends the analysis to arbitrary materials [6], including a prediction [7] that led to the measurement of a repulsive Casimir force nearly fifty years later [10]. The Casimir force is a force between surfaces that originates from electromagnetic fluctuations. Experimental progress has lagged behind theoretical developments, but the force has been measured numerous times [8, 9, 18, 36, 38, 173, 174], between many materials [11, 41, 44, 50, 175, 176], in several geometries [14, 52, 177], and with increasing precision [39, 178, 179].

One branch of Casimir force measurements seeks to harness the force to develop new MEMS devices [180], which has resulted in non-linear MEMS oscillators [40,181] and on-chip Casimir force measurement devices [13, 14]. Several measurements of the Casimir force have been made in ambient conditions, a necessary test for realistic MEMS devices, which preferably can operate in air at room temperature [11,37,46]. In a sense, the Casimir force can be utilized in a MEMS device only to the level of accuracy with which it has been measured (otherwise the device itself would lead

to a better measurement technique). Therefore, the limitations to measurements of the Casimir force in air are also the limitations to any Casimir-based MEMS device than operates in air.

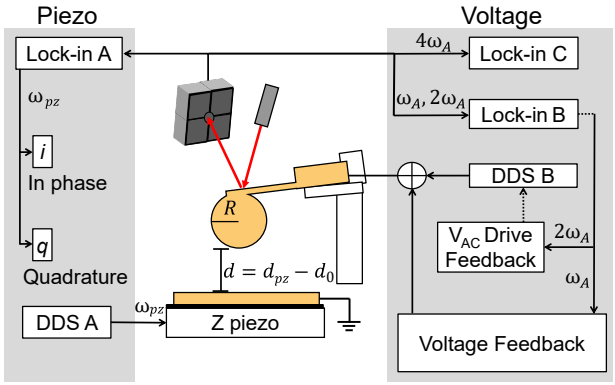

Figure 4.1: An atomic force microscopy setup is used to measure the Casimir force. An optical lever detects deflections of the cantilever to which the sphere is attached. Direct digital synthesizer (DDS) A is used to drive the piezoelectric transducer and shake the gold-coated plate. The cantilever's response to this oscillation is detected using a lock-in amplifier (LIA) and separated into in-phase and quadrature components. DDS B is used to apply an AC voltage to the cantilever at frequency ω_{A}. The oscillations of the cantilever are then detected at frequencies ω_{A}, $2\omega_{\mathrm{A}}$, and $4\omega_{\mathrm{A}}$ with LIAs B and C. During the measurement of the Casimir force V_{AC} is adjusted so that the oscillation at $2\omega_{\mathrm{A}}$ is constant, but during the calibration the voltage is held constant. For both, the signal at ω_{A} is used to estimate and eliminate the minimizing voltage V_0, by applying a DC voltage to the sphere.

Here we test the relative merits of different measurement techniques in air, identify several sources of uncertainty, estimate the uncertainty from each source, and discuss strategies to reduce uncertainty in future measurements. As stated in [21], in addition to measuring the force, a measurement must satisfy three requirements: (i) it must mitigate the contributions of other forces (hydrodynamic, electrostatic, *etc.*), (ii) it must estimate the separation between the sphere and plate, and (iii) it must calibrate the force signal. We characterize how well (i)-(iii) are achieved in an actual measurement, and quantify the amount of uncertainty each

imparts. Furthermore, several other sources of error, such as optical interference, may manifest themselves differently in different experiments, but are common to many force measurement techniques. Other sources of error, such roughness, patch potentials, and limited dielectric information, have been discussed extensively in the literature.

Our ambition here is to combine all the different sources of uncertainty present in Casimir force measurements, in order to provide a total estimate of the uncertainty. For our measurements, uncertainty in separation is found to dominate the error at distances < 110 nm, while interference dominates the error at separations > 170 nm, and the overall calibration error dominates in the region between the two extremes.

4.1.1 Adapting an AFM for Casimir force measurements

All atomic force microscopes (AFMs) contain a microcantilever, a system to control the sample position (typically via a piezoelectric transducer), a system to excite the cantilever (piezoelectrically, electrostatically, photothermally, *etc.*), and a method to detect the motion of the cantilever (optical lever, interferometry, piezoelectrically, *etc.*). Although the uncertainty varies from system to system, there are general trends that different sources of error follow. For example, almost all sphere-plate Casimir force measurements rely on the electrostatic force for the estimation of the absolute separation, and the sphere-plate electrostatic force itself has been studied several times [182, 183]. Various approximations are used for the

electrostatic force, and the force is fit over a different range for most measurements. Thus systematic errors in the sample separation estimation may manifest themselves differently across different measurements, but there are many similarities.

Because the AFM used here (Cypher, Asylum Research) is very similar to the AFMs used in prior Casimir force measurements (figure 4.1), an analysis of the inherent uncertainty helps to predict the uncertainty present in other systems. It actuates the sample and cantilever via piezoelectric transducers, which is common to many force measurement procedures [11, 179]. The motion of the cantilever is detected by an optical lever, a beam of light reflected off of the cantilever and onto a quad-photodiode [36, 37, 46]. The electrical signal is then fed into several lock-in amplifiers (LIAs), which are used to detect the motion of the cantilever at the relevant frequencies. The voltage applied to the probe is the sum of a signal form a direct digital synthesizer (DDS), $V_{\mathrm{AC}} \sin(\omega_{\mathrm{A}} t)$, and another voltage controlled by a feedback loop V_0, while the sample is grounded through a 3.3 kΩ resistor to prevent harming the probe. The plate used in the measurements discussed here is a silicon substrate coated with 5 nm of chromium and 100 nm of gold (e-beam), and the sphere is made of hollow glass (Trelleborg) coated with Cr(3 nm)/SiO_2(50 nm)/Cr(3 nm)/Au(100 nm).

4.1.1.1 Lock-in amplifiers

The LIAs suffer from several artifacts, which is common enough that several groups have started building their own. The signals output from each contain a

small offset voltage (≈ -180 μV), which varies over time. To eliminate the effect of its variation, a null signal is collected from each LIA at each separation, and the null signal is averaged over time to reduce noise. In addition, the driving signal of from each DDS couples directly into the output of the corresponding LIA. Although our LIAs differ from most others, because they are built from field programmable gate arrays, the types of artifacts generated by their imperfections are similar across different systems.

4.1.1.2 An overview of the method

The method here follows the phase-separated amplitude modulation (AM) method developed by de Man *et al.* [21], in which the plate's position is oscillated, and the in-phase and $\pi/2$ delayed (quadrature) response of the cantilever are tracked. The separation is determined using the cantilever's response to an applied AC voltage V_{AC} on the probe at frequency ω_{A}, and observing the 2nd harmonic. The plate is slowly brought towards the sphere at discrete positions. The sphere approaches and retracts from the plate about 100 times over two days.

4.2 Force measurement

All Casimir force measurements must select some signal by which the force is measured. Common choices have included the static or oscillating deflection of either a beam or a torsion pendulum, or a frequency shift. Here, several measurement techniques are discussed, with a particular focus on their suitability in an ambient

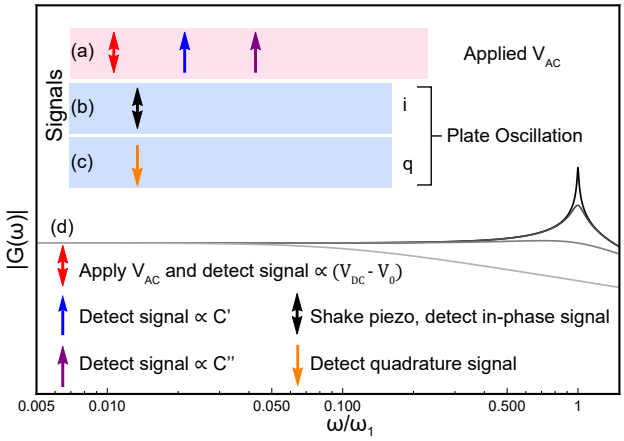

Figure 4.2: The transfer function of the cantilever, $G(\omega)$ describes how forces at different frequencies are converted into cantilever oscillation. (a) An AC voltage is applied, and the oscillation is used to minimize the electrostatic force (red arrow). The 2nd and 4th harmonics (blue and purple arrows) are then used to estimate the separation and sensitivity, respectively. (b) The plate is shaken at $\omega_{\rm pz}$, and the in-phase response is due to the conservative forces between the plate and the sphere. (c) The quadrature response is due to the dissipative forces ($\propto \dot{d}$). (d) The cantilever transfer function far from the surface (black) has a fairly large Q factor (≈ 100), but as it approaches the surface, hydrodynamic damping decreases the Q factor (grey curves).

environment. The amplitude modulation method used in later sections is presented first, followed by deflection and frequency modulation methods.

4.2.1 Amplitude modulation

The amplitude modulation (AM) technique of de Man *et al.* drives cantilever oscillation with the Casimir force directly, by shaking the plate vertically at frequency $\omega_{\rm pz}$ [21]. The AM technique is similar to a new (vacuum) technique that measures the difference in the Casimir force between two materials by spinning them, so that a lock-in can be used to probe the difference of the force between the two materials [176], but instead of changing the material, the separation is varied. The response of the cantilever to the moving plate has two components: an in-phase

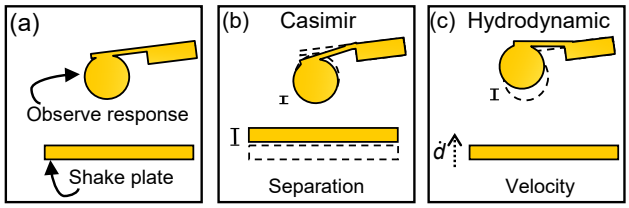

Figure 4.3: (a) The sphere-plate force is probed by shaking the plate and observing the response of the probe. (b) Conservative forces, which depend on position but not velocity, bend the probe proportionally to the plates displacement, so the response they cause is in-phase with the position of the plate. (c) The hydrodynamic force, on the other hand, is proportional to velocity, so that it is $\pi/2$ radians out-of-phase with the plate's displacement.

and a quadrature component (figure 4.3):

$$S^I = -\frac{\gamma}{k}\left(\frac{\partial F_{\rm es}}{\partial d} + \frac{\partial F_{\rm C}}{\partial d}\right)\Delta d, \tag{4.1}$$

$$S^Q = \frac{\gamma}{k} F_{\rm H}, \tag{4.2}$$

where γ is the optical lever sensitivity (V/m), Δd is the shake amplitude, k is the spring constant, $F_{\rm C}$ is the Casimir force, $F_{\rm es}$ is the electrostatic force, and $F_{\rm H}$ is the hydrodynamic force. The proximity force approximation (PFA) is then used to compare the measured signal to the Casimir force between parallel plates:

$$\frac{1}{R}\frac{\partial F_{\rm C}}{\partial d} = 2\pi F_{\rm pp}, \tag{4.3}$$

where $F_{\rm pp}$ is the Casimir force between parallel plates. The procedure used to implement the AM method is described below, along with the errors characteristic to the AM method.

4.2.1.1 The procedure

The entire measurement cycle is divided into a force measurement portion (≈25 min per run) and a calibration portion (≈5 min). During the measurement portion, the sphere begins about 5 μm from the plate and is brought towards it at discrete separations. At each separation, the measurement is performed in two steps. During the first, an AC voltage, V_{AC}, is applied to the sphere at frequency ω_{A} (while the plate is grounded), which in turn drives the cantilever at frequencies ω_{A} and $2\omega_{\mathrm{A}}$. The signal at $2\omega_{\mathrm{A}}$ is input into a feedback loop that controls V_{AC} to maintain a constant amplitude setpoint A_{set}. A second feedback loop applies a slowly varying voltage, V_0, to the sphere in order to minimize the signal at ω_{A}, which in turn eliminates the potential difference between the sphere and the plate. During the first step, the plate is not shaken, but the null signal of the LIA which detects the cantilever's response to the shake is recorded in order to characterize is slowly-varying voltage offset.

The force measurement is performed in the second step. The oscillating voltage V_{AC} is turned off, and the minimizing voltage, measured in the first step, is applied to the sphere, so that the electrostatic force is mitigated. Then the position of the plate is oscillated by a piezo, while the response of the cantilever is detected by the optical lever and recorded by a lock-in amplifier. Null signals of the LIAs that detect the electrostatic force are also collected during the second step.

The calibration portion follows a similar approach/retract procedure, collecting data in two steps at each separation, except a constant $V_{\mathrm{AC}} = 8$ V is used to

drive the electrostatic force, in order to excite the $4\omega_A$ harmonic. During the calibration run, the cantilever remains >200 nm from the surface, so that the large electrostatic force does not cause jump-to-contact. The $4\omega_A$ harmonic is combined with the $2\omega_A$ harmonic to estimate γ and k (see 4.3 for details). The measurements here use $\omega_{pz}/2\pi$=211 Hz and $\omega_A/2\pi$=77 Hz.

4.2.1.2 Excluding the hydrodynamic force

When the plate is oscillating at over 100 Hz, the hydrodynamic force is comparable to or larger than the Casimir force at separations greater than 100 nm. However, the hydrodynamic force is proportional to velocity, which is $\pi/2$ radians out of phase with the position. A lock-in amplifier separates the in-phase from the quadrature signal in order to separate the hydrodynamic force from the Casimir force (figure 4.3). The delay between the direct digital synthesizer and plate must be measured in order to set the reference phase to sufficient accuracy, because the hydrodynamic force enters into the Casimir force signal $\propto \sin(\Delta\theta_{ref})$, where $\Delta\theta_{ref}$ is the error in the reference phase. The reference phase is set to within 0.2 degrees by the method discussed in section 4.2.1.5.

4.2.1.3 Ratcheting

Because the Casimir force signal is proportional to Δd (equation 4.1), increasing the shake amplitude can vastly improve the signal-to-noise ratio and permit measuring the Casimir force at larger separations. However, using a larger ampli-

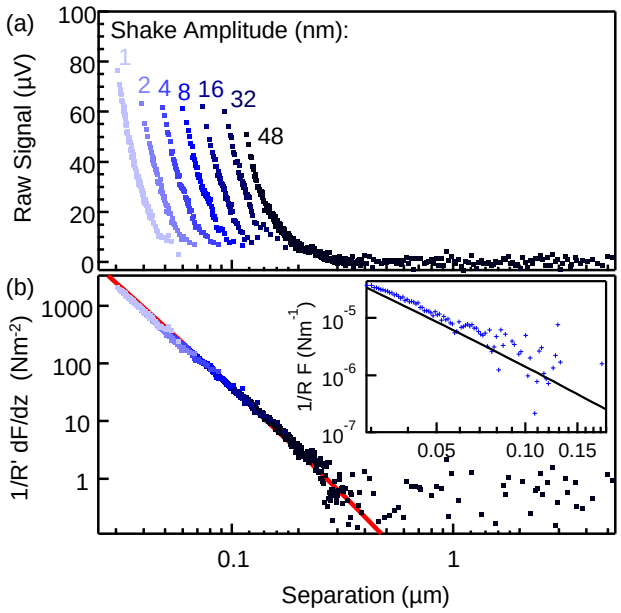

Figure 4.4: (a) To increase the sensitivity of the distance modulation measurement technique, while also avoiding errors associated with the strong nonlinearity of the force, the amplitude is varied across the measurement. (b) The data collected at each shake amplitude are combined for the final estimate of the force gradient. The data are shown binned into groups of 200 individual measurements. The red line shows the calculated Casimir force gradient. The inset shows the force as measured by the deflection technique, and the black line shows the calculated Casimir force.

tude both limits the minimum achievable separation and can lead to a systematic overestimate of the Casimir force $\propto (\Delta d/d)^3$ [184]. However, the Casimir force signal is smaller than the noise from thermal motion at a single separation in one measurement cycle, and so a typical proportional/integral feedback loop would either have gain too small to change the amplitude quickly enough, or would be too noisy to get a clear force signal.

To maximize the signal while mitigating the errors associated with large shake amplitudes, a ratcheting technique is introduced. As the tip approaches the surface, it begins with a 48 nm shake amplitude at a separation of $\approx$5 μm. At about 150 nm from the surface, the raw force signal reaches a threshold, and the shake amplitude

decreases to 32 nm. At a slightly closer distance, the signal hits the threshold again, and the amplitude drops to 16 nm. The process repeats until a 1 nm shake amplitude is achieved at the closest separation (figure 4.4a). With retraction, the process is reversed. The amplitude starts at 1 nm and then becomes larger after the signal falls below a threshold.

4.2.1.4 Interference

Because the optical lever used to detect the motion of the cantilever is coherent, an interference pattern appears in the response signal of the cantilever to the shaking plate. Some small amount of the optical beam falls partially off of the cantilever (*e.g.* Airy disks), and that light has a different path length to the detector than the light reflected directly off the cantilever [185]. As the cantilever is brought towards the surface, the interference condition at the photodiode changes. The interference artifact is common to AFMs that use optical lever detection [185], and has been mentioned before in Casimir force measurements as a factor that limits accuracy at large separations [46].

In order to minimize the optical interference in the Casimir measurements presented here, two different optical sources are tested, a diode laser (860 nm) and a superluminescent diode (SLD) [186], which limits the coherence of the light (by increasing its frequency spread). The test is preformed using the same procedure as the force measurement. The cantilever approaches the surface once with the laser and once with the SLD (figure 4.5). The SLD is confirmed to decrease the

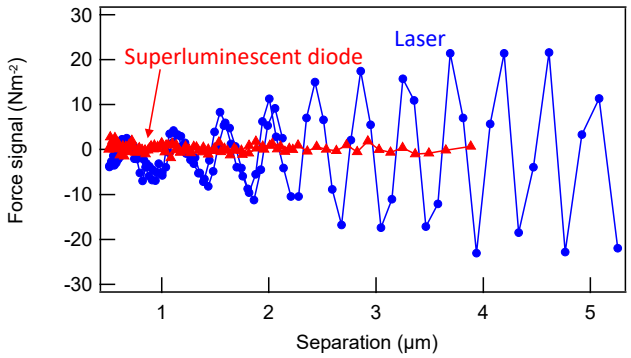

Figure 4.5: The interference effect is analyzed by comparing the calibrated force/area signal at distances larger than 500 nm. The interference is linear in shake amplitude like the Casimir force itself, and so it is reported, after calibration, in $\mathrm{N/m^2}$. Here, the laser causes interference fringes on the order of $\pm 10\ \mathrm{N/m^2}$ (red), but the superluminescent diode (SLD) produces fringes with a magnitude of about $1\ \mathrm{N/m^2}$. Thus, the SLD detector reduces the error imparted by interference by a factor of 10.

interference artifact in the force signal by about an order of magnitude relative to the laser. Even so, the interference from the SLD is apparent in later force data at the level of about $1\ \mathrm{N\ m^{-2}}$.

The uncertainty due to the interference is estimated by fitting the data to sine waves at separations > 500 nm. The primary wavelength in the interference is half the wavelength of the source, but the fit also includes the wavelengths of the next three harmonics (so that $\lambda/2, \lambda/4, \lambda/6$, and $\lambda/8$ are included). During the fitting, only one of harmonics is permitted to vary at a time. The amplitudes of all the harmonics are summed to estimate the uncertainty imparted by interference. Although the fits characterize the uncertainty of the measurement well, in so much as the amplitude of oscillations observed tends to be about what the fit predicts, attempts to use the fits to remove the interference after measurement removed minimal uncertainty because the four spatial frequencies do not completely describe the

interference, and the interference may change its amplitude at separations where the Casimir force is present, as it does between 2 and 4 μm in figure 4.5. The interference artifact varies by a factor of ≈ 4 between measurements, and tends to be less if the beam is further from the surface.

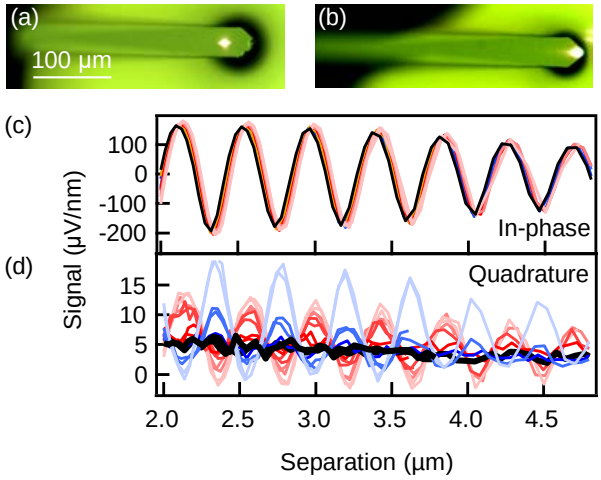

Figure 4.6: (a) During force measurements, the detection laser is focused at least 15 μm away from the edges of the cantilever, in order to minimize interference. (b) By focusing the detection laser at the tip of the cantilever, the interference is greatly increased. (c) Because the interference only appears in the in-phase channel of the lock-in amplifier, it can be used to precisely characterize the phase of the lock-in amplifier, to within about 0.2 degrees, so that the hydrodynamic force can be excluded from the Casimir force channel more completely (0-5 degree reference phases shown).

4.2.1.5 Setting phase

While interference is problematic in the force measurement, it can be utilized to set the reference phase of the lock-in amplifier that records the response of the cantilever to the shaking plate (figure 4.6). First, note that the interference is proportional to the position of the plate, so the interference appears in the same channel as the Casimir force, and is excluded from the channel containing the hydrodynamic

force. The reference phase is adjusted so that the interference falls entirely in the in-phase channel of the lock-in amplifier. Because of the delay between the direct digital synthesizer and the z-piezo, the phase is not known initially. Other methods that determine the reference phase by adjusting it while recording the output of a known signal are disrupted by the LIA offset. The interference method of setting the phase removes the effect of the LIAs output voltage by observing the phase over many separations.

4.2.2 Frequency modulation

The highest precision claimed in measurements of the Casimir force comes from frequency modulation (FM) measurements in vacuum [39, 179], in which the probe sphere is attached to an oscillator. The resonance frequency of the oscillator then changes as the force gradient on the sphere changes. The frequency shift is given by:

$$\Delta\omega = -\frac{\omega_1}{2k}\frac{\partial F}{\partial d}, \tag{4.4}$$

where ω_1 is the resonance frequency of the first eigenmode. No Casimir force experiments using the FM technique have been reported in environments other than vacuum. Our attempts toward an FM measurement in ambient condition and the artifacts found in that environment are discussed below.

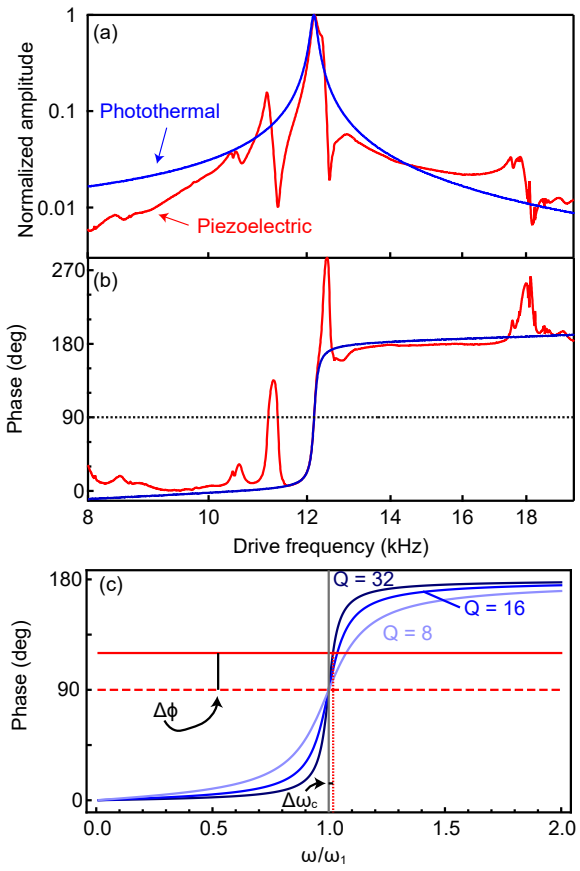

Figure 4.7: The transfer function of the cantilever is measured with both piezoelectric and photothermal drive. Both the amplitude (a) and the phase (b) of the piezoelectric drive show significant oscillations relative to photothermal actuation. If the phase curve crosses the 90 degree line more than once, instabilities occur in frequency-modulation measurements, in which the cantilever's apparent resonance frequency jumps from one crossing to another, without any change to the cantilever's actual resonance frequency. It should be noted that even though the photothermal actuation produces a transfer function much more similar to the transfer function of the undriven cantilever, it still differs from the ideal cantilever transfer function because of the thermal time constant. (c) For a small initial frequency misalignment $\Delta\omega_c$, there is an associated phase misalignment, $\Delta\phi$. The Q-factor decreases as the sphere approaches the surface, so that, while $\Delta\phi$ remains roughly constant, the frequency misalignment grows, $\propto 1/Q \propto 1/d$.

Because FM-AFM is a fairly mature field [165], experiments with FM-AFM were the first to identify a major source of error: piezo actuation [187–190]. When the transfer function of a cantilever is measured from its thermal motion, or from photothermal actuation, it has several resonance peaks but is otherwise quite smooth. On the other hand, the transfer function of the entire piezoelectric transducer/cantilever system is quite jagged and unpredictable, and even changes significantly over time (figure 4.7a). In vacuum, appearance of the piezo transfer function is masked by the very large Q factor of the cantilever, but its effects are still present, even if reduced [189]. The uncontrolled nature of the piezoelectric transfer function causes several problems: (1) There are multiple nearby frequencies which satisfy the 90 degree phase shift condition that is used by the feedback to track the resonance frequency of the cantilever, (2) the piezo drive voltage necessary to maintain constant piezo oscillation depends strongly on the drive frequency, and (3) the transfer function cannot be described by a harmonic oscillator, which makes it difficult to deduce the exact resonance frequency. Having multiple frequencies that satisfy the feedback condition can lead to 'jumps' in $\Delta\omega$ which do not correspond to any real change in the force and inhibit data analysis (figure 4.8a).

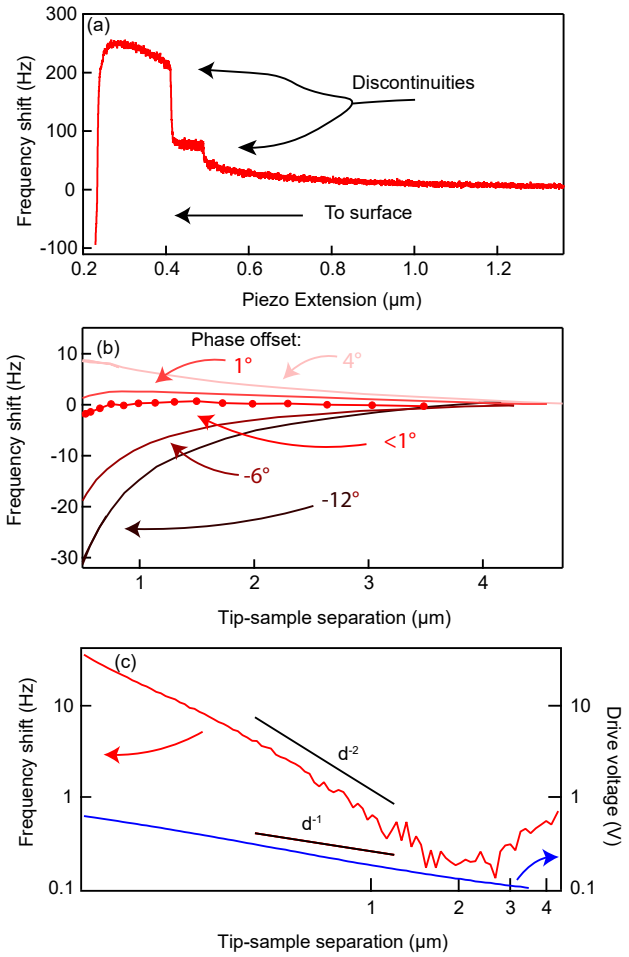

Figure 4.8: Several errors are common to frequency modulation force measurements in air. (a) When there to be multiple frequencies for which the phase of oscillation is 90 degrees, the feedback loop can then jump between these different frequencies, so that the value of the frequency shift is no longer related to the force gradient. (b) Any initial error in the estimated resonance frequency (equivalent to error in the initial phase estimate) grows $\propto 1/d$ as the sphere approaches the surface. (c) Even if the initial frequency error is set to be negligibly small, an error appears in the frequency offset channel $\propto 1/d^2$.

The second and third conditions are not quite as prohibitive on their own, but enlarge the impact of other errors. The frequency at which a cantilever is driven in an FM measurement is the resonant frequency itself, plus some small offset that depends on the accuracy of the fitting $\omega = \omega_1 + \Delta\omega_c$. Trying to estimate $\Delta\omega_c$ directly from the piezoelectric transfer function leads to errors on the order of 100 Hz, but using the thermal motion of the cantilever over several minutes enables the reduction of $\Delta\omega_c/2\pi$ to a few Hz. The error in $\Delta\omega_c$ is equivalent to an error in the setpoint of the phase, so that the phase is $90° + \Delta\phi$, where 90 degrees is the phase of the cantilever exactly on resonance (figure 4.7c). The phase, then, is the measured quantity used by the feedback loop to control ω_1. When the separation between the sphere and the plate changes, so does the hydrodynamic damping, which leads to a change in the Q-factor [191]:

$$Q = \omega_1^{-1}\left(\Gamma_0 + \frac{6\pi\eta R^2}{d}\right)^{-1}, \tag{4.5}$$

where Γ_0 is the damping of the probe far from the plate, and η is the dynamic viscosity. The phase of the cantilever's oscillation is:

$$\phi = \arctan\left(\frac{\omega\omega_1}{Qk(\omega_1^2 - \omega^2)}\right), \tag{4.6}$$

so that:

$$\omega(\phi) = -\frac{\omega_1\cot(\phi)}{2Qk} + \sqrt{\frac{\omega_1^2\cot^2(\phi)}{4Q^2k^2} + \omega_1^2}. \tag{4.7}$$

Setting $\phi = \pi/2 + \Delta\phi$ and assuming $\Delta\phi \ll 1$,

$$\omega(\pi/2 + \Delta\phi) \approx \omega_1(1 + \frac{\Delta\phi}{2kQ}). \tag{4.8}$$

A frequency offset error $\Delta\omega_{\text{err}}$, resulting from the phase error, can be defined. It has a d^{-1} dependence near the surface:

$$\Delta\omega_{\text{err}} \approx \omega_1^2 \frac{6\pi\eta R^2}{2kd}\Delta\phi. \tag{4.9}$$

Thus, $\Delta\phi$ causes an artificial frequency offset. Over several different FM measurements, the phase offset is varied from 12 degrees below resonance to 4 degrees above resonance. The frequency offset follows a power law, the amplitude of which depends strongly on $\Delta\phi$. Because there is no force which is expected to have that behavior, it is be attributed to equation 4.9. Note that even in the smallest phase offset achieved ($<$ 1 degree), the artifact remains noticeable.

If $\Delta\phi$ is small enough, another artifact appears with a d^{-2} dependence. Because the LIA that detects the cantilever oscillation is electronically coupled (unintentionally) to the direct digital synthesizer DDS that drives the shake piezo, the output signal of the LIA contains a small component related to the DDS drive signal. Because the output of the LIA is used to determine the measured phase, we can write $\phi_{\text{LIA}} \approx \phi + \mathfrak{a}V_{\text{shake}}$, where $\mathfrak{a}$ describes the coupling[1]. Up to equation 4.9, the analysis is identical, but now it is assumed that $\Delta\phi$ is zero far from the surface,

[1]Linear coupling is used as a reasonable model, even though the actual coupling is more complicated.

but includes the LIA error so that $\Delta\phi = \mathfrak{a}V_{\text{shake}}$. Note that the phase error is similarly coupled to the shake amplitude A. When it is further assumed that V_{shake} is controlled to maintain a constant A (i.e. $V_{\text{shake}} = \mathfrak{b}A/Q$), and $\mathfrak{b}$ is the frequency dependent ratio between the driving voltage and amplitude response, the artifact becomes:

$$\Delta\omega_{\text{err}} \approx \omega_1^2 \frac{6^2\pi^2\eta^2 R^4}{2kd^2}\mathfrak{a}\mathfrak{b}A. \tag{4.10}$$

Unlike equation 4.9, which can be corrected by improving the estimate of ω_1, there is no simple way to mitigate equation 4.10, except by improving the isolation of the LIA. Figure 4.8c shows the frequency shift and drive voltage for a measurement in which the initial frequency offset is minimized. The d^{-2} power law is similar to that predicted above, and further tests are carried out on the sample used to exclude the possibility that patch potentials caused the appearance of the d^{-2} signal ([109] and chapter 5). Ergo, it is concluded that the LIA coupling (which can be observed independently of the frequency offset it causes) is the source of the artifact.

Additional options to eliminate the effect of the LIA coupling remain. One possibility is to hold V_{shake} constant and let the amplitude vary, but that leads to a similar artifact. If $\mathfrak{a}$ were known exactly, the artifact could plausibly be subtracted, but there is no reason to suspect that the coupling does not also contain higher-order terms whose behavior is only masked by the magnitude of the artifact created by the linear term. The artifact of equation 4.10 does not necessarily make FM Casimir force measurements impossible in air, it only clarifies the necessity of decoupling

electronics from one another to a degree not possible in our current setup. Many of the artifacts discussed here should affect measurements in vacuum less.

4.2.3 Deflection measurements

Several experiments in air have measured the Casimir force through the detection of the cantilever deflection of the cantilever [36, 37, 46]. At any one height, the deflection $\mathfrak{D} = F(d)/k$, but low-frequency $1/f$ noise dominates the signal, which leads to a trade-off: acquiring force curves faster excludes more low-frequency drift, but also leads to more correlation between the error at nearby separations. Moreover, increasing the speed at which the data are collected causes the hydrodynamic force, which is proportional to velocity, to be present in the data at higher levels. In addition, repeated contact with the surface during measurements can damage the tip. While damage does not always occur, and can be observed after the measurement by AFM or SEM, it can be difficult to identify when during a measurement the probe is damaged.

Here, during the course of the measurements, deflection data is acquired in addition to amplitude modulation data. In the deflection data, the force is observed out to separations of ≈ 100 nm. In principle, it should be possible to observe the Casimir force over a longer range than the force derivative because is follows a d^{-3} instead of a d^{-4} power law. However, the inability to lock-in on the deflection harms the signal-to-noise, because of the large $1/f$ noise at low frequencies. The force measured through deflection can be seen in the inset of figure 4.4b.

4.3 Calibration and separation estimation

The calibration and separation estimation in Casimir force measurements are most often performed with the electrostatic force, although the hydrodynamic force has been used as well in liquids, where Debye screening limits affects the electrostatic force [192]. In the low Reynolds number limit, the hydrodynamic force is proportional to d^{-1}, so it seems as though it might also be possible to use it to estimate the tip-sample separation in air, as it has been used in liquid [20]. The difficulties with using the hydrodynamic force are twofold: (1) the hydrodynamic force is nearly two orders of magnitude weaker in air than in water, so the signal to noise of its detection is smaller and (2) the slip length[2] at ambient pressures is quite large ($\approx$ 50 nm [193]), and while it can be included in the fit, the extra free parameter further reduces the accuracy of the separation estimation. Thus, calibration with the electrostatic force is the focus of this section.

4.3.1 The electrostatic force

The electrostatic force between a plate and a sphere is:

$$F = -\frac{C'(V + V_0)^2}{2}, \tag{4.11}$$

[2]The slip length is the separation from the surface below which the separation-dependence of the hydrodynamic force becomes more gradual.

where V is the applied potential between the plate and the sphere, V_0 is the minimizing potential, and $C' = \partial C/\partial z$, where C is the sphere-plate capacitance,

$$C' = 2\pi\epsilon_0 R \sum_{n=1}^{\infty} \frac{\coth(\alpha) - n\coth(n\alpha)}{\sinh(n\alpha)}, \tag{4.12}$$

and α is defined by the equation $\cosh(\alpha) = 1 + d/R$. The voltage applied to the probe has two components: $V_{\rm AC}$ and V_0, so that the total applied voltage is $V = V_{\rm AC}\cos(\omega_{\rm A}t) + V_0$. We can separate the electrostatic force on the cantilever on the sphere into three terms:

$$F_{\rm es} = F_{\rm DC} + F_a + F_b, \tag{4.13}$$

where the individual forces are separated according to the frequency of the voltage:

$$F_{\rm DC} = -\frac{C'(t)}{2}\big((V_0 + V_0)^2 + \frac{V_{\rm AC}^2}{2}\big), \tag{4.14}$$

$$F_a = -C'(t)V_{\rm AC}(V_0 + V_0)\cos(\omega_{\rm A}t), \tag{4.15}$$

$$F_b = -\frac{C'(t)}{4}V_{\rm AC}^2\cos(2\omega_{\rm A}t), \tag{4.16}$$

where it is noted that C' itself depends on t implicitly, because the sphere-plate separation varies with time.

Signals generated by the latter two forces, F_a and F_b, are crucial to the measurement procedure. The signal generated by F_a is used as the input to a feedback loop which measures V_0, akin to the loop used in Kelvin probe force mi-

croscopy [66]. The intricacies of the V_0 estimation procedure have been discussed extensively in the literature relating to patch potentials [183,194], and in the literature of KPFM [82–84], and so here they are only discussed briefly. The force F_b causes the cantilever to oscillate, which in turn generates a signal with $S_{2\omega_A} = \gamma \frac{C'}{4} V_{AC}^2 / k$.

To determine the separation and sensitivity, the measured values of $S_{2\omega_A}(d)$ are fit to the a function of the form:

$$\frac{S_{2\omega_A}}{V_{AC}^2} = \frac{\mathscr{B}}{2} \frac{C'\left(\frac{d_{pz}-d_0}{R}\right)}{R}, \tag{4.17}$$

in which the two free parameters are the sensitivity ($\mathscr{B} = \gamma R/2k$) and the absolute position offset (d_0). The relative piezo displacement is typically measured accurately, for example, by a linear differential transformer, so that the the electrostatic force can be fit assuming that relative displacements over a measurement are exact, and only the absolute sphere-plate separation (d_0) is unknown. Both γ and k are both assumed to be frequency-independent, because all the frequencies used are much lower than the resonant frequency of the cantilever. The electrostatic force data is fit over a large range (generally ≈100 nm to ≈5 μm) to minimize the correlated errors between the fit parameters [3].

[3] For example, if the fit were performed only over 300-400 nm, there would be lots of variance in the possible $\mathscr{B}$ and d_0 values that could be fit to the data. Increasing d_0 and $\mathscr{B}$ both by a factor of two would lead to about the same fit quality. However, when the fit is performed from 0.1-5 μm, the two fit parameters are independent.

4.3.2 Systematic uncertainty in V_0

The first major source of uncertainty in V_0 comes from using F_a to determine V_0. From the analogy with KPFM, it is known that the voltage which minimizes the electrostatic force is not the same as the voltage that minimizes the electrostatic force derivative, because the cantilever (rather than the tip) contributes the majority of the electrostatic force signal, but the tip contributes most of the force derivative signal [87]. For Casimir force measurements, the spherical probe has a much larger radius than an AFM probe (40 μm vs 30 nm), so the cantilever contributes a much smaller portion of electrostatic force.

The second source of uncertainty is present because an AC voltage (rather than DC) is applied to the probe. The AC voltage applied to the probe can inductively couple into the drive piezo, which leads to an extra signal fed into the voltage feedback loop (section 2.2.2). The additional signal combined with the separation-dependence of the electrostatic force leads to a distant-dependent artifact in V_0 [82]. Any generic offset of the output of a lock-in amplifier, in fact, leads to such an error. The voltage artifact is proportional to $1/C'$, and knowledge of C' permits an estimate of the voltage error. If all the separation-dependence of V_0 is attributed to the extraneous voltage, then estimates can be made of the original offset and the residual electrostatic force that remains because of the extraneous voltage. For the forces here we estimate that the offset in the signal is less than 10 μV, which would lead to an error in V_0 of less than 10 mV at separations where the Casimir force is measured.

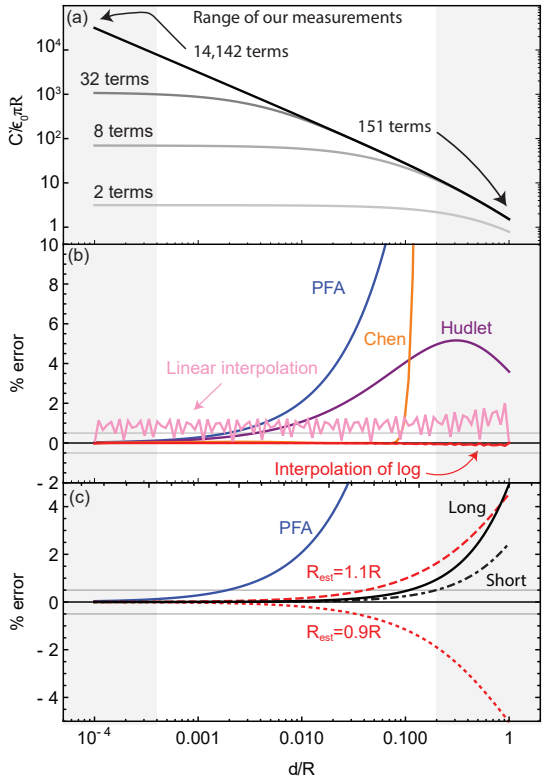

Figure 4.9: (a) The full sphere-plate capacitance gradient (C') is an infinite sum. For $d/R > 1$, less than ten terms are required, but in the small d limit, thousands of terms are required to reach accuracy within 1% of the C'. The highlighted central region shows the range of data pertinent to the Casimir force measurements discussed in this thesis. (b) Several approximations exist for the sum: the proximity force approximation (PFA) has been the traditional choice, the approximation of Chen *et. al.* [175] (orange) extend the PFA as a power series in d/R, the Hudlet *et. al.* approximation [127] (purple) gives the correct behavior in both the large and small-d limits, and deviates from the sum by at most 5%. Interpolation decreases computational demands, while eliminating the systematic errors associated with the approximations. For linear interpolation (pink) and logarithmic interpolation (red), the exact force is calculated at 43 points and then plotted from interpolation for 100 different points. (c) The logarithmic interpolation (black) outperforms the PFA even when the estimated sphere radius is over- (dashed) or under-estimated (dotted). The cantilever alters C' by less than 2% in the pertinent range for the spheres with 40 μm radii (black).

4.3.3 Approximations and fitting

The computational demands of equation 4.12 have caused several approximations to be used, the most prominent of which is the proximity force approximation for C':

$$C'_{\mathrm{PFA}} \approx \frac{2\pi\epsilon_0 R}{d_{\mathrm{pz}} - d_0}. \tag{4.18}$$

The other common approximation in Casimir force measurements was developed by Chen *et al* [175] to improve the estimate of the separation. It starts with the PFA and then expands $C' - C'_{\mathrm{PFA}}$ as a Taylor series in d/R around $d = 0$ out to the seventh term, so that the error is vastly reduced for $d/R \leq 0.08$. Unfortunately, for $d/R > 0.08$, the Chen approximation diverges even more quickly than the PFA with increasing d/R, and the divergence only becomes worse with more terms. Another approximation to the exact C' is the Hudlet *et al.* approximation [127]:

$$C'_{\mathrm{Hudlet}} \approx \frac{2\pi\epsilon_0 R^2}{(d_{\mathrm{pz}} - d_0)(d - d_0 + R)}. \tag{4.19}$$

Although it has not been used for Casimir force measurements before, it is noteworthy because it approximates the exact solution well in both the near and far limits, and diverges from the exact C' by less than 6%.

All the aforementioned approximations are inadequate for our experiments, particularly because the capacitance at short range is most affected surface rough-

ness, or a water layer, or surface states [195]. The computational difficulty of the infinite sum is not in the evaluation of the sum itself, which takes less than a minute to solve to better than 1% accuracy on a laptop, but the fact that it has to be summed for every iteration of the fitting procedure. If instead the force is calculated once for a number of points, the data for those points can be saved and interpolated for later fits. The simplest interpolation is to linearly interpolate the calculated $C'(d/R)$ versus d/R, which works quite well and is within 2% of the actual C' over the whole range of the electrostatic fits, better than any of the other approximations. Still, it imparts more error than is preferable, particularly at separations below $d/R = 0.01$, where it is worse than the PFA.

To improve the interpolation, we note that C' is approximately linear on a log-log plot. Hence, $\log(C')$ vs $\log(d/R)$ is linear enough for interpolation, hereon called the logarithmic interpolation. It deviates from the exact C' by less than 0.5 % over the whole range of the fitting, which is less than any of the previous approximations or the linear interpolation, even though the full equation 4.12 sum is only calculated for 43 separations. Because the interpolation itself is limited to the values between the minimum and maximum value of d/R, it can be helpful for fitting to use equation 4.18 for separations below the lowest interpolated value and the $n = 1$ term of equation 4.12 for separations above the largest interpolated value. Then however the fitting algorithm chooses to direct its iterations, the function is well defined.

One possible advantage of the PFA is that lumps the spring constant k and the radius R into one term, decreasing the number of sources of uncertainty. However,

the value of of R is available from, for example, an SEM or AFM image of the probe. One might be concerned that error in R would impart more error into the fit than the R-agnostic PFA. However, figure 4.9c shows that the effect of either over- or under-estimating the value of R by 10% affects the estimate less adversely than the use of the PFA.

4.3.4 Determining k and γ

Higher harmonics driven by the non-linearity of the electrostatic force are used to separate the k from γ. To calculate them, we expand C' to 1st order in a Taylor series:

$$\begin{aligned} C'(t) &= C'(d) + C''(d)A\cos(2\omega_{\mathrm{A}}t) + ... \\ &= C' - C''\frac{C'}{4k}V_{\mathrm{AC}}^2\cos^2(2\omega_{\mathrm{A}}t). \end{aligned} \tag{4.20}$$

Then, inputting the Taylor series into F_b, forces at higher frequencies are found:

$$\begin{aligned} F_b = &-\frac{C'}{4}V_{\mathrm{AC}}^2\cos(2\omega_{\mathrm{A}}t) \\ &-\frac{C'C''}{16k}V_{\mathrm{AC}}^4\cos^2(2\omega_{\mathrm{A}}t). \end{aligned} \tag{4.21}$$

The $\cos^2$ of the second term can then be expanded, so that the electrostatic force on the cantilever at frequency $4\omega_{\mathrm{A}}$ can be calculated up to first order as:

$$F_{4\omega_{\mathrm{A}},1} = -\frac{C''C'}{32k}V_{\mathrm{AC}}^4\cos(4\omega_{\mathrm{A}}t). \tag{4.22}$$

Using the PFA approximation for the capacitance in equation 4.22,

$$F_{4\omega_A,1} = -\frac{\pi^2 \epsilon_0^2 R^2}{8kd^3} V_{AC}^4 \cos(4\omega_A t), \tag{4.23}$$

which is the same value found by de Man *et al.* when the PFA is assumed from the beginning [21].

Note that $F_{4\omega_A,1}$ depends on k independent of γ, so the signal that it generates, $S_{4\omega_A}$, can be used to separate the two parameters. To do so, the electrostatic force is driven with $V_{AC} = 8$ V on approach, so that both the $S_{2\omega_A}$ and $S_{4\omega_A}$ signals are generated. The determination of d_0 is performed with the $S_{2\omega_A}$ data to estimate the overall prefactor ($\mathscr{B}$) and d_0. Using the d_0 found from the first fit, the $S_{4\omega_A}$ signal is fit to equation 4.23. Because it is small far from the surface, the relative phase of $S_{4f\omega_A}$ (unlike all other signals used) is not set before the measurement, so in-phase and quadrature components are measured and fit to functions of the form $\mathfrak{B}/(d-d_0)^3$ separately. Then the phase of the signal is estimated and the two components are added in quadrature. Then $\mathfrak{B}$ can be used to separate k and γ:

$$k = \frac{\epsilon_0 \pi R}{4} \frac{\mathscr{B}}{\mathfrak{B}}, \tag{4.24}$$

$$\gamma = \frac{\mathscr{B}^2}{2\mathfrak{B}}, \tag{4.25}$$

where $\mathscr{B}$ comes from the C' fit (equation 4.17).

4.3.5 Systematic errors in separation determination

4.3.5.1 Drift

Drift both imparts error to each individual determination of the sensitivity and separation and also hinders the integration of multiple data sets. To address drift in our experiments, first the separation is determined for each run. Then the drift within a run is estimated to be the change in d_0 from the two runs before it and the two runs after it. Approaches during which the drift is too non-linear to be corrected by this technique are then excluded from the rest of the analysis. For the measurement shown in this chapter, none of the approaches showed prohibitive drift, and the average drift is about 3 nm/hr.

4.3.5.2 Cantilever bending

The cantilever bends as it approaches the surface, changing the surface separation. The bending itself is often used for Casimir force measurements, though here it can only be used out to about 100 nm, because of the fairly stiff cantilevers being used. Still the bending amounts to as much as 3 nm at the closest approach. To correct for it, the static deflection is recorded at each height, and a phenomenological power law is fit to the data to describe it. The deflection signal (μV) is converted into a separation by multiplication by γ^{-1}. Then the recorded piezo extensions are adjusted to account for the cantilever being closer to the surface by the amount it bends. Although a fairly small correction, it imparts uncertainty into the final

separation estimate proportional to the uncertainty in the γ, which is observed to vary by $\approx 10\%$ over a measurement in section 4.3.5.8.

4.3.5.3 Water layer

A thin water layer forms on most surfaces exposed to ambient conditions. Because of the large DC permittivity of water (ϵ_{H_2O}=80), even a nm-thick water layer can significantly affect the capacitance. The capacitance per unit area between two parallel plates a separation d apart with a water layer of thickness $\mathfrak{t}$ on one of the surfaces is:

$$C_{\rm pp}(\mathfrak{t}) = \frac{\epsilon_0}{d + \mathfrak{t}(\frac{1}{\epsilon_{H_2O}} - 1)}. \tag{4.26}$$

Thus, the relative increase due to the water layer is:

$$W(\mathfrak{t}) \equiv \frac{C_{\rm pp}(\mathfrak{t})}{C_{\rm pp}(\mathfrak{t}=0)} = \frac{1}{1 + \frac{\mathfrak{t}}{d}(\frac{1}{\epsilon_{H_2O}} - 1)} \tag{4.27}$$

where ϵ_{H_2O} is the DC permittivity of water, and $C_{\rm pp}$ is the capacitance between parallel plates. Now, because the water layer is very thin relative to the radius of the sphere, the PFA is used to calculate the affect of water on the sphere-plate fit, so that C' with a water layer becomes:

$$C'(\mathfrak{t}) \approx C'(\mathfrak{t}=0)W(\mathfrak{t}), \tag{4.28}$$

where the equation is exact in the PFA limit.

Unfortunately, the thickness of the water layer can vary over the course of a measurement unless humidity is controlled, and $\mathfrak{t}$ can vary across a single sample, particularly at grain boundaries. Moreover, estimates of $\mathfrak{t}$ on gold vary widely depending on the type of measurement and the exact deposition process for the gold [47, 196, 197]. Without modeling or *in situ* measurement, the water leads to uncertainty in d_0 of at least a nanometer. The voltage applied between the sphere and the plate can also increase $\mathfrak{t}$ [198].

4.3.5.4 Second-order oscillation

The non-linearity of the electrostatic force not only leads to oscillations at higher harmonics, but also leads to higher-order corrections to the $S_{2\omega_A}$ signal. Using the PFA, the signal is [21]:

$$S_{2\omega_A} = -\frac{\gamma\epsilon_0\pi R V_{AC}^2}{2kd} - \frac{\gamma\epsilon_0^2\pi^2 R^2 V_{AC}^4}{2k^2d^3} - O(V_{AC}^6), \tag{4.29}$$

$$= -\frac{\gamma\epsilon_0\pi R V_{AC}^2}{2kd}\left(1 + \delta + ...\right), \tag{4.30}$$

where $\delta = \frac{\epsilon_0\pi R V_{AC}^2}{kd^2}$. Now estimating the effect of the second-order oscillation on the capacitance comes down to estimating δ. Note that during the measurement run, V_{AC} is controlled by a feedback loop to produce a constant signal, S_{set}. Then, it is

possible to solve for δ, assuming it is much less than one:

$$\delta \approx \frac{\epsilon_0 \pi R}{kd^2} \frac{2kdS_{\text{set}}}{\gamma \epsilon_0 \pi R} \tag{4.31}$$

$$\approx \frac{2S_{\text{set}}}{\gamma d}. \tag{4.32}$$

Now, with a typical cantilever (table 4.1) and $S_{\text{set}} = 1$ mV, $\delta \approx 0.014$ at 100 nm. Thus the correction is only a very small portion of the overall signal, however, the slow d-dependence makes it difficult to avoid the error without correcting for it. Note that these oscillations have a similar source as equation 4.22, and can in principle be estimated by measuring the $4\omega_{\text{A}}$ signal (however, our AFM setup does not have sufficient channels).

Table 4.1: Typical probe

Name	$\frac{\omega_1}{2\pi}$ (kHz)	L (μm)	W (μm)	R (μm)	k (N/m)	$1/\gamma$ (nm/V)	Q
CSC38-A	10	250	33	40	0.1	700	100

4.3.5.5 Feedback oscillations

If the proportional gain is set too high on either the V_0 or V_{AC} feedback loops, the applied voltages can begin to oscillate, because the filters on the lock-in amplifiers are inadequate to completely eliminate the low-frequency noise from coupling into the feedback loops, even combining 2nd-order low-pass and notch filters. The voltage oscillations tend to be at the frequency ω_{A} and effectively decrease the applied voltage.

The effect on the effective applied voltage is measured by recording V_0, V_{AC}

and the applied voltage $V_{\mathrm{AC}}\cos(\omega_{\mathrm{A}}t)+V_0$ as time series data at 5 kHz, as well as the time-averaged lock-in data. For large proportional gain, oscillations are seen in both the V_0 and V_{AC} channels. The amplitude of the oscillations is proportional to the proportional gain on the respective feedback loops, and is about 10 degrees out of phase with the original applied voltage. It is possible to mitigate the source of these oscillations by decreasing the proportional gain. Because the additional oscillations are predictable, it is also possible adjust for them in data where they are present with out imparting much error by adjusting the applied voltage by the amount of the oscillations. However, it is preferable to maintain a low enough gain so that such oscillations do not occur.

4.3.5.6 Roughness I

Roughness appears twice in the error analysis, first in the discussion of the error in the separation determination and calibration and second in the direct evaluation of the force. The importance of roughness pertains to the error it imparts into the measurement, rather than how it changes the force on average, which can be calculated fairly accurately.

Many different roughness corrections have been developed for Casimir force measurements. The first corrections were perturbative and assumed that the surface could be described by an average height with some standard deviation [199]. Other corrections realized that the correlation length of the surface roughness leads to a spectrally-dependent change to the Casimir force [200]. After it was realized that

surface roughness follows a very skewed probability distribution, new statistical methods were developed to account for the irregularity of the distribution [201]. Finally, the dependence on the particular orientation of the sphere was noted, and a PFA-based technique was developed to estimate the uncertainty in the force from the uncertainty in the relative orientation of the sphere (the spheres are typically much rougher than the plate) [202].

Here, the uncertainty due to roughness is estimated using the oriented-PFA procedure akin to the one pioneered by Sedmik *et al.* [202]. However, whereas the focus of the earlier paper is on the contribution of micron-scale spherical deformations to measurements of the Casimir force, here 10-100 nm-scale roughness is the focus, because all spherical topographies measured with the AFM presented here appear similar when a best-fit sphere is subtracted. Because one expects spheres placed on cantilevers to be randomly oriented, their similarity indicates that, due to the large z-range of the AFM scans, it is not long-range spherical deviations that are being measured, but instead what is observed is due to the tip-shape of the scanning probe [203]. Note that an apparatus for measuring microsphere roundness is currently under development [204].

To prepare AFM topography scans of the spheres for a roughness analysis, the topography is first fit to the shape of sphere (with the radius and center as free parameters), and the fit is removed. The resulting image still has some systematic long-range distortions. To correct for the distortions, the image is median filtered with a filter size much larger than the short-range roughness (> 100 nm). The median-filtered image is then subtracted from the raw image so that only short-

range roughness remains.

A point is chosen to be the point of closest approach on the sphere, and the measured topography is placed onto a model sphere of the appropriate radius. The PFA is used to compute the roughness correction. The force on a rough sphere is computed as its variation from smooth sphere. For the regions on the sphere where the topography is known, the force from the smooth sphere is subtracted and replaced with the force from the rough sphere, on a pixel-by-pixel basis:

$$F_{\mathrm{r}}(d) = F_{\mathrm{s}}(d) - \sum_{i,j} \left[F_{\mathrm{pp}}(h_{\mathrm{s}}(d, x_{i,j})) - F_{\mathrm{pp}}(h_{\mathrm{r}}(d, x_{i,j})) \right], \tag{4.33}$$

where $\sum_{i,j}$ is a sum over all the pixels in an image, F_{r} and F_{s} are the forces from the rough sphere and a smooth sphere, respectively, in the PFA limit, F_{pp} is the force between each pixel and the plate below it, and $h_{\mathrm{s}}(d, x_{i,j})$ and $h_{\mathrm{r}}(d, x_{i,j})$ are the separation between the surface of the sphere and the plate at that particular pixel for a smooth and rough sphere, respectively, when the point of closest approach is d away from the plate. Note that this formulation of a roughness PFA correction can be used to calculate either the electrostatic or Casimir force, as in [202], and works similarly well with force gradients (figure 4.10).

4.3.5.7 Surface states

The assumption that the macroscopic equation for capacitance is adequate for describing plate-plate and sphere-plate capacitance at the nanoscale has not been

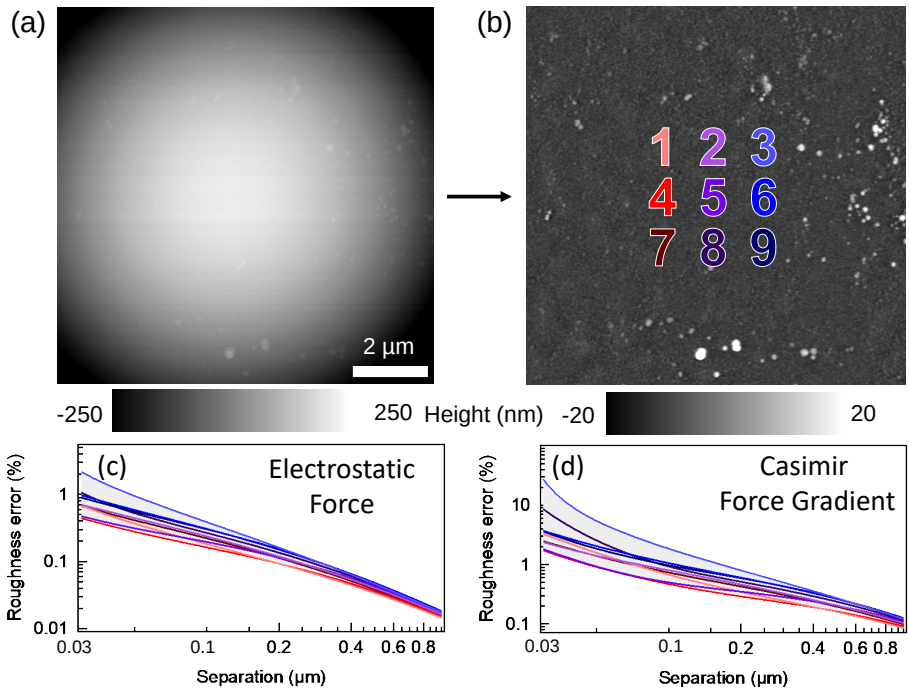

Figure 4.10: (a) To calculate the uncertainty due to roughness, an AFM image of the sphere is fit to a sphere, and the fit is removed. After the fit is removed, a 64 × 64 pixel median filter is used to separate the roughness from any imaging artifacts. (b) Several points are chosen on the roughness image to act as possible points of closest approach. (c) Then the electrostatic force for the sphere with roughness relative to a smooth sphere is calculated for each of the different points, and the grey area shades the region between the maximum and the minimum of the nine locations. (d) The Casimir force gradient for a rough sphere relative to a smooth sphere is also calculated for the nine points, and shows a much larger uncertainty because of the stronger separation-dependence of the force.

stringently tested. For materials where this assumption has been tested (e.g. silicon and germanium), naively fitting a measured electrostatic force to the macroscopic form of the capacitance can lead to distance offsets (for silicon) between 60 and 600 nm, depending on preparation, which were attributed to surface states [195]. The offset for gold is likely less, but the presence of water or other adsorbates may complicate the surface states.

4.3.5.8 Stability of electrostatic calibration

To understand the stochastic error and drift in the electrostatic calibration, the calculated absolute position offset d_0, the spring constant k, the optical lever sensitivity γ, and the force gradient sensitivity are recorded for each approach (figure 4.11). Over the ≈ 36 hours of measurements shown, d_0 drifts by about 110 nm (or 3 nm/hr). Both k and γ vary by about 10% over time, and their variation is mostly stochastic. The force gradient sensitivity, on the other hand, shows systematic drift, but changes by less than 1%. While the stability of these calibrations shows that they are very precise, one must be careful, as they may hide systematic errors.

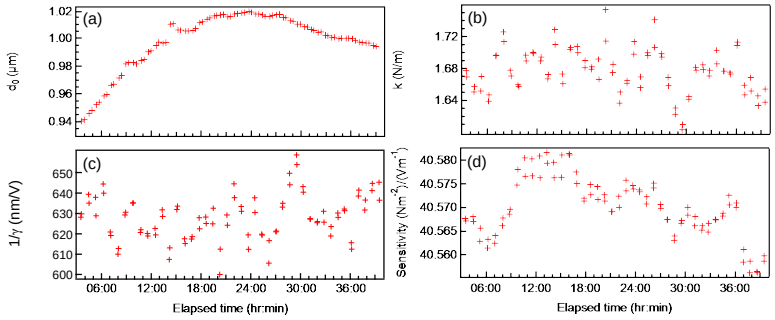

Figure 4.11: (a) The position of the plate, d_0 drifts over time, at a rate of about 3 nm/hr on average. For each run, a line is fit to d_0 versus time, including the two previous runs, the two subsequent runs, and the run itself. The drift is then deduced from the fit and the linear drift correction is applied. (b,c) The estimate of the spring constant and $1/\gamma$ vary by about 10% over the measurement, but (d) the calculated sensitivity, which is the product of the two, varies much less.

4.3.6 Uncertainty from the electrostatic calibration

Most of the above sources of error tend to cause the surface to appear closer than it is. The exceptions is bending, which causes the true separation to deviate from the piezo displacement. Moreover, these different sources of uncertainty can

cause correlated error. The uncertainty in the water layer thickness is quite large from previous experiments, so we posit a 0-1.5 nm water layer on each surface, which in turn leads to a ± 1.5 nm uncertainty in the separation of the two metal surfaces if determined from C', because $\epsilon_{\mathrm{H_2O}} \gg \epsilon_{\mathrm{air}}$. The other sources contribute less, mostly through uncertainty in γ. Thus, bending contributes about ± 0.2 nm of uncertainty, while second-order oscillations also contribute about ± 0.3 nm of separation uncertainty (based on fitting with vs without the correction), so that the total uncertainty in position is about ± 2 nm. Surface states and long-range surface deformation could further increase the separation uncertainty, but they have been left out of the present analysis in the absence of adequate methods of quantifying them.

4.4 Total uncertainty

4.4.1 Fundamental limits to the measurement range

Understanding the fundamental limits to AM Casimir force measurements helps to frame the effects of other sources of uncertainty. Jump-to-contact (JTC) limits how close to the surface Casimir probes can approach, and for measurements in which the shake amplitude is less than the separation (*e.g.* for deflection measurements, or the amplitude modulation measurements discussed here), the criterion for JTC is $k < \partial F/\partial d$ [64, 205]. The minimum possible separation is then limited by

the JTC, so that when the dominant force is the Casimir force [1]:

$$d_{\min} \gtrapprox \left(\frac{\hbar c \pi^3}{120}\frac{R}{k}\right)^{1/4}. \tag{4.34}$$

A typical probe (table 4.1) should be able to measure up to about 43 nm from the surface, which approximately agrees with experiment. Because of the d^4 power law in the force, equation 4.34 is fairly insensitive to k. For example, if k is increased by an order of magnitude to 1 N/m, $d_{\min}$ only decreases to 24 nm, less than a factor of two. To approach closer to the surface requires a combination of much smaller R and larger k.

Thermal noise limits the furthest separation at which the force can be measured. The minimum detectable force that can be detected with the AM method described above is $F_{\min} = k n_{\rm d}\sqrt{B}/\gamma$, where $n_{\rm d}$ (V Hz$^{-1/2}$) is the noise amplitude density at the detector, and B is the detection bandwidth. In the experiments discussed here, the $n_{\rm d}$ is dominated by the detector, but the fundamental limit to sensitivity is the cantilever's thermal motion. Because the oscillation frequency is much less than the resonant frequency, only the first eigenmode of the cantilever is considered. When thermal noise is dominated by the cantilever's motion [119]:

$$n_{\rm d} = 2\gamma\sqrt{\frac{k_{\rm B}T}{k\omega_1 Q}}. \tag{4.35}$$

Then the minimum detectable force is:

$$F_{\min} = 2\sqrt{\frac{kk_{\mathrm{B}}T}{\omega_1 Q}}\sqrt{B}, \tag{4.36}$$

which, when the properties of a typical cantilever are used, is ≈ 10 fN. However, in our technique the force derivative rather than the force is measured. The minimum detectable force gradient is:

$$F'_{\min} = 2\sqrt{\frac{kk_{\mathrm{B}}T}{\omega_1 Q}}\frac{\sqrt{B}}{\Delta d}, \tag{4.37}$$

where Δd is the oscillation amplitude of the plate. The maximum separation is found by finding the separation at which the force equals the minimum detectable force gradient (employing the Casimir formula and PFA once more):

$$d_{\max} = \left(\frac{\hbar c\pi^3 R}{240}\frac{\Delta d}{\sqrt{B}}\sqrt{\frac{\omega_1 Q}{kk_{\mathrm{B}}T}}\right)^{1/4}. \tag{4.38}$$

The appearance of Δd suggests that it is possible to increase $d_{\max}$ arbitrarily, but of course Δd must always be significantly less than d, so that the sphere does not hit the surface, and to avoid systematic errors associated with the non-linearity of the force [184]. The fairly generous bound $\Delta d < d/3$ then gives:

$$d_{\max} < \left(\frac{\hbar c\pi^3 R}{720}\frac{1}{\sqrt{B}}\sqrt{\frac{\omega_1 Q}{kk_{\mathrm{B}}T}}\right)^{1/3}. \tag{4.39}$$

For typical cantilevers with $B \approx 100$ mHz, the furthest detectable force should occur

at $d_{\max} < 1.5$ μm. Note that the effective power law that the sensitivity follows falls from d^{-4} to d^{-3} when Δd is allowed to vary, showing how ratcheting (section 4.2.1.3) increases the range over which the force may be measured.

Measurements of the Casimir force by the AM technique of de Man *et al.* are thus fundamentally limited to separations between ≈ 40 nm to 1.5 μm, or about one and a half orders of magnitude, which is comparable to the largest ranges probed by previous measurements [9]. Using several probes with varying R and k may increase the range a bit more, but the $(R/k)^{1/4}$ and $(R/k^{1/2})^{1/3}$ coefficients in the minimum and maximum separation imply that variations in either parameter minimally affect on the range of separations that can be measured. The remaining sections discuss the sources of uncertainty that prevent measurements from achieving the range set by fundamental limitations.

4.4.2 Characteristics of different uncertainties

The uncertainty in the measurement is divided into several groups (as shown in figure 4.12), depending on how each affects the measurement. First is the calibration uncertainty, which includes uncertainty in the measurements of k,R, and γ, as well as uncertainty in the calibration of the piezo actuation. While variation between different techniques[4] for calibrating k can be as large as 17% [206], similar electrostatic calibration experiments on colloidal probes suggest that the error in k from using electrostatic calibration is at the $\approx 5\%$ level [207].

[4]Techniques used to estimate k include analyzing the cantilever's thermal motion, or measure the change in the cantilever's resonance frequency when it is used to pick up particles of a known mass.

Uncertainty in the absolute position of the sample relative to the probe is one of most problematic sources of error in Casimir force measurements because of the strong separation-dependence of the force. The uncertainty in the measured F' is calculated from the uncertainty in the position (± 2 nm) multiplied by F''. All the separation uncertainties of section 4.3 are summed together as absolute values, because correlations are expected.

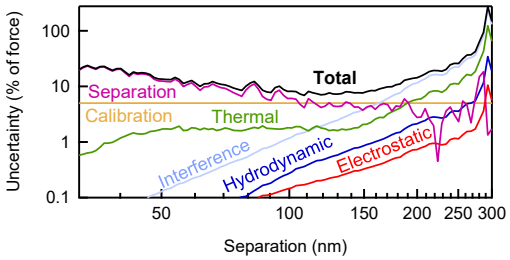

Figure 4.12: The expected uncertainty in the Casimir force measurements is calculated from several sources of error. At short range, separation determination and roughness dominate the error, at large separations interference, the hydrodynamic force and thermal motion dominate, and calibration errors (sensitivity, estimate of piezo motion, etc.) dominate only for the intermediate separations.

Some amount of the hydrodynamic force is present in the Casimir force data, and that is a product of the how well the reference phase is calibrated, and how strong the hydrodynamic force is. The uncertainty originating from the hydrodynamic force is estimated by multiplying the measured hydrodynamic force by $\sin(\Delta\theta_{\text{ref}})$, where $\Delta\theta_{\text{ref}}$ is the uncertainty in the reference phase.

Even though using a superluminescent diode decreases the effect of interference by an order of magnitude, interference remains a major source of uncertainty in the measurements. The interference varies greatly in both phase and magnitude between the different spheres. The magnitude of the interference is estimated by

the technique described above in section 4.2.1.4.

Stochastic noise is estimated dividing the standard deviation of the data within a small separation range ($\approx$ 1 nm) by the square root of the number of data collected within that range. For a single approach, stochastic noise is likely to be one of the largest sources of error, but after $\approx$50 approaches, it is no longer the largest source of uncertainty. Here, the stochastic noise comes primarily from the photodetector, which could be improved, but there is always at least some stochastic noise due to the thermal motion of the cantilever.

The electrostatic force is present because of an artifact in the minimizing voltage detected by the KPFM feedback loop. The uncertainty in the electrostatic force is calculated from the largest possible voltage artifact consistent with the measured V_0 data, as discussed in section 4.3.2.

4.4.3 Total measurement uncertainty

To understand how the difference sources of error contribute to the force measurement at different separations, the uncertainties are added in quadrature to calculate the total uncertainty in the measurement at separations from 50 nm to 300 nm (figure 4.12). At short separations, separation and roughness uncertainty are the greatest, while at large separations, interference, thermal noise, and the hydrodynamic force dominate the uncertainty. The force sensitivity is limited to $\approx$ 2 pN,[5] about two orders of magnitude larger than the fundamental limitation of this

[5]The sensitivity is approximated from the smallest clearly observable force: smallest force $\approx$(minimum $\frac{1}{R}\frac{\partial F}{\partial d}$)$\times(\Delta d) \times (R) \approx$(1 Nm^{-2})$\times$(48 nm)$\times$(40 μm).

measurement method, which indicates that significant reductions in uncertainty are possible.

4.4.4 Reducing measurement uncertainty

Based on the above analysis, there are two routes to reduce the uncertainty in the Casimir force measurements. The tactics used to reduce the uncertainty near the surface must improve the separation determination, while far from the surface, interference, thermal noise, and the hydrodynamic force must all be reduced.

4.4.4.1 Near the surface

At small separations, the Casimir force can be measured well above the thermal noise level. To improve the measurement, it is necessary to improve the separation determination. Because many factors contribute to the uncertainty in the separation as determined by the electrostatic force, it would be infeasible to address them all at once. Some, such as the presence of a water layer, could be addressed with improved characterization of the samples, but others, such as second-order oscillations, are intrinsic to the AC electrostatic separation determination technique. Therefore, the clearest tactic is to develop new ways of determining the separation and comparing them. The most direct way to measure the position of the surface is through contact measurements, although when roughness is present there is significant uncertainty in the relation between the distance-upon-contact and the relative position of the two surfaces for typical spheres. However, for sufficiently smooth surfaces the

difference vanishes. A few of the systematic errors depend explicitly on the AC nature of the detection force. By using DC voltages and measuring static deflection, those errors could be avoided. Likewise, if an electrostatic signal proportional to C'' rather than C' were used, as is used for H-KPFM (chapter 2), long-range deformations would contribute less uncertainty (although roughness would contribute more). In addition, the hydrodynamic force, which has been used successfully for separation estimation in liquids [20] could be tested in air, although the slip length is considerably larger (≈ 50 nm versus < 10 nm) [193, 208].

4.4.4.2 Far from the surface

While the measurements discussed here observe the Casimir force about as close to the surface as is possible (limited by jump-to-contact, equation 4.34), the force is predicted to be observable out to a separation about three times larger than it is observed. Therefore, at large separations there is potentially more value to decreasing the uncertainty. The hydrodynamic force can be made smaller by shaking the plate at a lower frequency, by improving the accuracy of the reference phase, or by using smaller spheres. The interference is harder to eliminate because the SLD used is already designed to minimize coherence. One possibility would be to measure the position of the cantilever with light at several wavelengths. Other possibilities include measuring the force with the optical lever at a few different positions along the back of the cantilever to change the path length of the interference, or controlling the focus of the light onto the cantilever. Different detection techniques, such as

using laser doppler vibrometry [209] or a piezoelectric cantilever [210], could also eliminate the artifact. The uncertainty from thermal noise can be reduced by taking more data or using a larger shake amplitude.

4.5 Uncertainty from the force calculation

The uncertainty in Casimir force gradient measurements comes not only from the measurement error, but also from uncertainty about the sample being measured, which includes uncertainty in optical properties [29,30,211], patch potentials [15,19, 109,126,212], and roughness [37,200–202]. Because of these factors, the calculated force has some uncertainty itself. For example, if the orientation of the sphere were known exactly, it would be possible to calculate the exact force on the rough sphere. However, there is some uncertainty in the orientation of the sphere. The uncertainty in the orientation of the sphere then leads to uncertainty in the calculation of the force (equation 4.18). The percent deviation from the estimate is plotted at 1-σ, e.g. at 30 nm separation, $\approx 68\%$ of the orientations give a calculated force within $\pm 4\%$ of the average. We note that this is not the same as the percent change of the force. The median force gradient increase due to roughness is 10% stronger, and about 68% of the sphere orientation are within a $10 \pm 4\%$ change. Of the different uncertainties in the measured force, the uncertainty in the gold's optical properties is the limiting uncertainty over most of the range, but at the shortest separations, roughness is the larger source of error (figure 4.13).

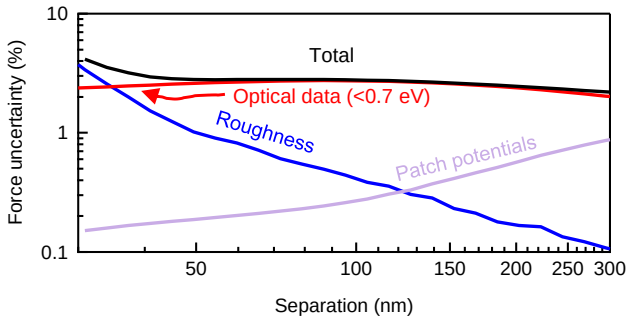

Figure 4.13: The uncertainty in the force calculation comes from several sources of error. Over most of the range, uncertainty in the dielectric constant at low frequencies is the largest source of uncertainty, but at the shortest separations, roughness becomes the largest. Patch potentials, which cause an additional force between the plate and sphere, cause less uncertainty.

4.5.1 Sample dielectric function

Uncertainty in the dielectric function of the interacting surfaces leads to uncertainty in the calculated Casimir force. Because $\epsilon_{\text{air}} \approx 1$, the two gold surfaces contribute most of the uncertainty to the Casimir force measurement. Because tabulated optical data used on its own leads 5-15% uncertainty in the force [29, 211], the dielectric response is measured with ellipsometry of an evaporated 100 nm Au film on a glass slide in the 0.73 to 6.3 eV range (figure 4.14). The ellipsometry data are then compared to the tabulated Palik data [213]. Because of the agreement with the ellipsometry data at high energies, the Palik data at energies above those collected with ellipsometry are used. The tabulated dielectric data agree with the measurement less well at low energies, and so the response there is extended with the Drude model. Pirozhenko *et al.* [29] lists the Drude model parameters for several different samples of gold. By comparing to measured ellipsometry data to the Drude parameters, the data from ellipsometry are determined to be most similar to

a plasma frequency $\omega_p = 8.84$ eV and $\omega_\tau = 0.042$ eV or $\omega_p = 7.50$ eV and $\omega_\tau = 0.061$ eV (figure 4.14). The force is computed using the UMD/Palik combined optical data together with each set of reference parameters, and the standard deviation of the difference between the two calculations is used as the uncertainty from the optical properties [23].

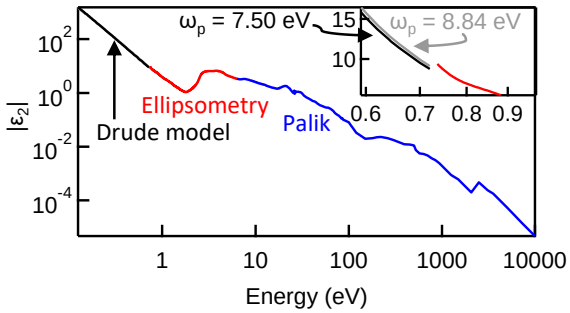

Figure 4.14: The dielectric data used to estimate the Casimir force is computed from ellipsometry data in the range 0.73 to 6.3 eV combined with Palik reference data at higher energies and the Drude model at lower energies.

4.5.2 Patch potentials

The force from patch potentials on gold tends to be about 1% or less, but it has become a major concern in Casimir force experiments, because it tends to follow a similar separation-dependence to the Casimir force. A few experiments have used various types of Kelvin probe force microscopy to calculate the patch potential force that would be felt between two spheres force [109, 214]. For the estimation of uncertainty presented here, the calculated patch potential forces from [109] are used, and discussed in chapter 5.

4.5.3 Roughness II

Roughness also adds uncertainty to the calculated force. Atomic force microscopy is used to measure the roughness on both the sphere and the plate, and if the relative positions of sphere and plate were known, then the predicted forces can be calculated directly from the topography images. However, there is uncertainty in the exact orientation of the sphere because the point of closest approach is known only to within about 3 μm, and the exact position above the plate is unknown as well. Because the sphere tends to be much rougher than the plate, the focus of the roughness uncertainty is based on how uncertainty in the orientation of the sphere begets uncertainty in the roughness profile of the interacting surfaces [202]. The same technique is used to calculate roughness corrections to the electrostatic force in section 4.3.5.6. To compute the roughness uncertainty, the Casimir force gradient is calculated for 49 different points on the sphere profile, and the uncertainty is computed as the the range around the most likely estimate within which $\approx$68% of the calculated roughness corrections fall. Note that the distribution of corrections is extremely irregular. The average correction is about 10% at 30 nm, but for two orientations, the sphere would have already made contact with the surface.

4.6 Conclusions

A measurement of the Casimir force has been presented, as well as several experiments designed to characterize the uncertainty in Casimir force measurements. Some of the sources of uncertainty are characteristic of only ambient environments

(water layers, drag, *etc.*), but many of the sources of error, such as interference artifacts and irregular transfer function from piezoelectric actuation uncertainty (FM) apply to other environments as well. Comparing the measurements shown and characterized here to the force that should be observable by a thermal-noise limited measurement shows that the largest reduction of uncertainty is possible between 400 nm and 1.5 μm. In that range, an interference pattern currently masks any force, but detecting the cantilever with multiple wavelengths of light, or with non-optical methods should greatly reduce the interference artifact. At separations in the 30 - 400 nm range, the data are consistent with the best-fit power law to the force gradient calculated by the Lifshitz theory, which is $\approx d^{-3.5}$. Higher accuracy will assist the search for materials which can be used to electronically modulate the Casimir force, which would have many uses in microelectromechanical systems [180].

Chapter 5: Patch potentials in Casimir force measurements

Patch potentials are predicted to cause a pressure between conductive surfaces and to introduce a small systematic error into Casimir force measurements [19]. The Casimir force has been measured in various setups including torsion pendulums [9], atomic force microscopes [36], and microelectromechanical systems [38,39]. Even in early measurements, patch potentials were suspected to cause an additional attractive force [9], although it was not directly observed. In more recent measurements, the force-minimizing voltage (V_0) was found to be distance dependent [182] and was attributed to patch potentials.

Theoretical models have been developed to quantify the pressure from patch potentials between parallel plates [19] and its effect on Casimir force measurements [19, 126]. A perplexing situation has arisen in the field of Casimir physics where some experimental data has supported a theory based on use of the plasma model for conductivity [39], while other data has supported a Drude model [178]. The competition between the Drude and plasma models has focused attention on patch potentials [15,128], as they may be a path to resolving the conflicting evidence from different experiments.

Electrostatic patch potentials complicate many other measurements as well

[215]. Recent examples include increased noise in gravitation measurements [212, 216], heating in ion traps [217], metal whiskers that short electonic circuitry [218], barrier height modification for Rydberg atom ionization [219, 220], and limited conductivity in graphene on SiO_2 [172]. In some cases, Kelvin probe force microscopy (KPFM) is used to measure the surface potential (SP) in order to diagnose experimental artifacts originating from electrostatic patches. Similarly, amplitude-modulated (AM) KPFM has been used to investigate patches originating from the crystal structure of copper [73]. The potential contrast increased upon decreasing relative humidity, a phenomenon which suggested that in ambient conditions, the average patch size grows, but the voltage difference between patches decreases [128].

Recently, Kelvin probe techniques have been used to measure the SP of gold in Casimir force experiments [214, 221]. The measurement of the SP on a gold-coated silicon nitride membrane *in situ* with a modification of frequency-modulated (FM) KPFM is reported in [221]. The measured force agreed with that calculated in [126] for two samples. The measurement, however, was limited in spatial resolution by the size of the probe (4 mm), and was not able to resolve the smallest patches. Another recent experiment [214] measured the SP on a gold plate in a nitrogen environment, which had been used previously in vacuum-based Casimir force measurements [222, 223], and was used to estimate the sphere/plate equivalent electrostatic pressure assuming both surfaces were covered with the measured potential. The estimated pressure was over an order of magnitude less than the discrepancy between the measured pressure and the pressure calculated by the Drude model.

In this chapter, we analyze our SP measurements in light of a recent patch

model [15] and show that patch potentials contribute a systematic error in Casimir force measurements, which likely increases the measured force between these materials by an amount of the same order of magnitude as the difference in the Casimir force when calculated using the Drude or plasma models for conductivity. Humidity is found to have a noticeable affect on patch potentials. Finally, patch potentials are measured on spheres used for Casimir force measurements, and the residual patch potential force is evaluated.

Note that the first section of this chapter is adapted from a paper published in the *Journal of Physics: Condensed Matter* [109].

5.1 Patch potentials from different deposition techniques

Measurements of the Casimir force require the elimination of the electrostatic force between the surfaces. However, due to electrostatic patch potentials, the voltage required to minimize the total force may not be sufficient to completely nullify the electrostatic interaction. Thus, these surface potential variations cause an additional force, which can obscure the Casimir force signal. In this section, we inspect the spatially varying surface potential (SP) of e-beamed, sputtered, sputtered and annealed, and template stripped gold surfaces with Heterodyne Kelvin Probe Force Microscopy (H-KPFM). In this section, FM feedback is used to control the H-KPFM topography loop, unlike the rest of the thesis, in which AM feedback is used. We find that patch potentials vary depending on sample preparation, and that the calculated pressure can be similar to the pressure difference between Casimir force calculations

employing the plasma and Drude models.

5.1.1 Theoretical considerations

A method has been developed to describe the pressure due to patch potentials in terms of the patch correlation function between parallel plates [19], which is given by:

$$\mathfrak{C}_{i,j}(\vec{x}) = \iint d^2\vec{x'}\, V_i(\vec{x'})\, V_j(\vec{x'} + \vec{x}), \tag{5.1}$$

where $\vec{x}$ and $\vec{x}'$ are the spatial coordinates, and $V_{i,j}$ are the potentials, with average removed, on each plate. The correlation function is converted to a radial form, $\mathfrak{C}(r)$, and is averaged over all angles at each position r. To calculate the force, the correlation function is transformed into k-space [15]:

$$\mathfrak{C}_{i,j}[k] = 2\pi \int_0^\infty dr\, r\, \mathfrak{C}_{i,j}(r)\, J_0(kr), \tag{5.2}$$

where J_0 is a Bessel function. The pressure between two parallel plates resulting from patches is:

$$P_{1,2}(d) = \frac{\epsilon_0}{4\pi} \int_0^\infty dk \frac{k^3}{\sinh(kd)^2} \left[\mathfrak{C}_{1,1}[k] + \mathfrak{C}_{2,2}[k] - 2\mathfrak{C}_{1,2}[k]\cosh(kd)\right], \tag{5.3}$$

where d is the distance between the two plates [15,19]. Here, we consider the pressure between plates with the same autocorrelation, but vanishing cross-correlation, so

that:

$$P(d) \approx \frac{\epsilon_0}{2\pi} \int_0^\infty dk \frac{k^3}{\sinh(kd)^2} \mathfrak{C}[k]. \tag{5.4}$$

5.1.2 Computational methodology

Once the potential is determined by KPFM, the mean of the potential image is subtracted. The x-y autocorrelation function of the SP is calculated, binned into a radial autocorrelation function, and normalized to the number of pixels summed over at each distance. Because our scan size is limited, the $\mathfrak{C}(r)$ is truncated for $r > \frac{L}{2}$ (by analogy to the Nyquist-Shannon sampling theorem [224, 225]). This procedure may slightly reduce the calculated pressure, but at longer distances $\mathfrak{C}(r)$ is sampled less and so is not representative. The radial autocorrelation function is numerically integrated to calculate $\mathfrak{C}[k]$. The pressure between parallel plates is calculated from equation 5.4.

5.1.3 Multiple deposition techniques

We prepared e-beam deposited, sputtered, sputtered and annealed, and template stripped gold (TSG) samples in order to determine how patch potentials vary with preparation. Gold was deposited to 100 nm thickness for all samples. One sample was e-beam deposited (Denton) at 3 μTorr with a 10 nm Cr sticking layer onto a polished silicon wafer, which was epoxied to a metallic puck pior to depo-

sition (EPO-TEK E4110). The other samples were sputtered (AJA International, Inc.) in a 2.5 mTorr argon environment onto a polished silicon wafer. Two were sputtered with a 20 nm Cr sticking layer, and their silicon substrates were epoxied to the pucks. The third was sputtered onto a silicon wafer directly, and a puck was epoxied to the exposed Au surface so that it could be template stripped [173, 226]. All three sputtered samples were heated for 6 hours at 80 °C to solidify the epoxy. One of the samples with a Cr sticking layer was annealed at 200 °C in ambient atmosphere for an additional 3 hours. The TSG sample was mechanically removed from the silicon immediately before scanning.

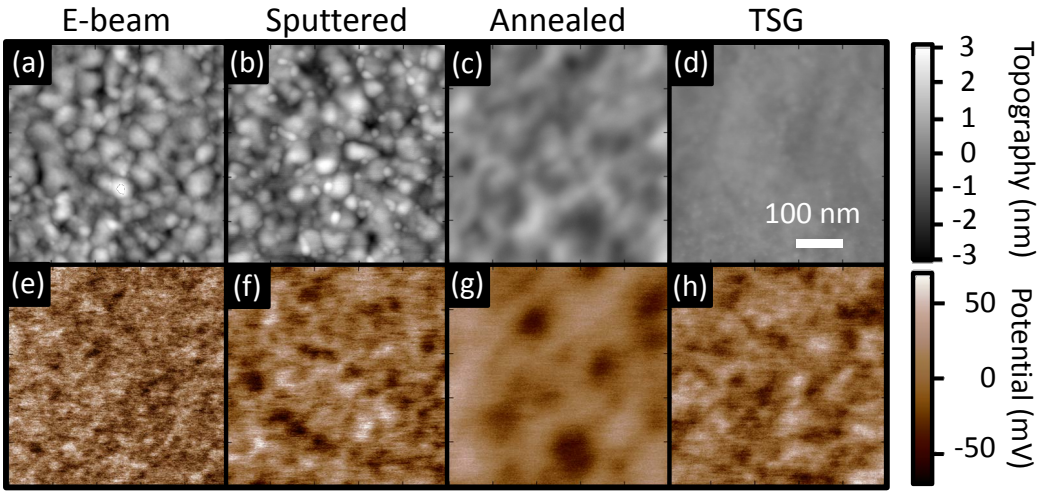

Figure 5.1: Surface potential of gold for e-beamed, sputtered, annealed, and template stripped gold (a-d) respectively. The topography recorded simultaneously (e-h).

The spatial distribution of the surface potential we observe differs significantly from sample to sample; however, the amount of the variation remains similar. figure 5.1 shows 500 nm scans of the surfaces, both the potential and topography. The e-beamed sample has the smallest patches, while the patches on the sputtered and

TSG samples are of similar size. The largest patches are found on the annealed sample.

The topography also varies significantly. Both the e-beamed and sputtered samples have similar roughness, while the sputtered and annealed sample shows less topographical variation. The TSG sample is the smoothest, as expected [173].

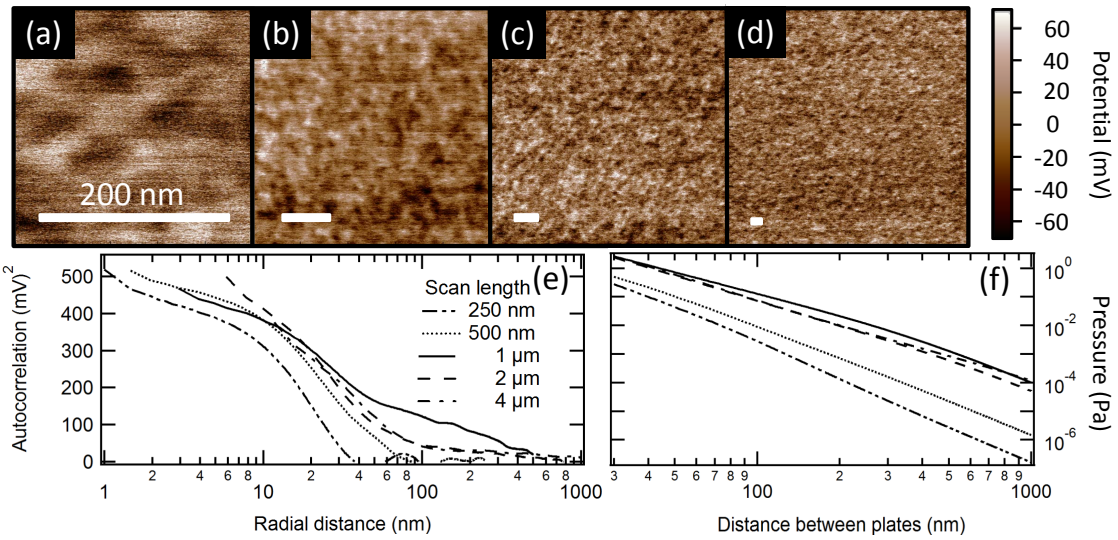

Figure 5.2: The measured patch potentials on a sputtered gold surface maintain the same general shape and distribution as the size of the scan is increased from 250 nm (a) to 1 μm (b), 2 μm (c), and 4 μm (d). However, the calculated autocorrelation function falls off much more quickly for increasing r in small scans (e) which leads to a smaller calculated pressure (f).

To understand how scan size affects the calculated pressure between plates, we investigate how $\mathfrak{C}(r)$ changes with scan size. Here we focus on the sputtered sample. figures 5.2 (a-d) and figure 5.1b show scans of the sputtered gold sample ranging from 250 nm to 4 μm. All scans are 1024 x 1024 and recorded at 0.3 Hz. The frequency offset was chosen from - 40 Hz (4 μm) to - 70 Hz (250 nm), in order to maximize resolution while maintaining stability. The general patch shape and size are consistent as the scan size is varied.

In some of the scans there is an abrupt difference between scan lines, a phenomenon which has been attributed to charge transfer at the tip [68]. Because we are concerned with the potential of the surface and not of the tip, the scan is 0th order flattened (the average of each scan line is subtracted) to mitigate the effect of any change in $V_{\rm tip}$. This procedure slightly decreases the amplitude of $\mathfrak{C}(r)$ for all the scans. However, for the smallest scans, it also introduces anticorrelations which were not seen in the larger scans. For this reason, we do not include any 500 or 250 nm scans in the pressure calculations of the subsequent sections. To observe the effect of 0th order flattening, compare the images in figure 5.1 to those in figure 5.2 (unflattened). A recent analysis of the spheres used in Casimir force measurements showed that flattening can remove low-frequency spectral data from an AFM image and affect the calculated autocorrelation function [202], particularly at long distances. Here, we remove $V_{\rm tip}$ variations in order to avoid an overestimate of the pressure.

5.1.4 Comparing surface potential pressure to plasma and Drude models for the Casimir force

We calculate the pressures from the 1, 2, and 4 μm scans and compare them to the plasma-Drude Casimir pressure difference. Before computing pressures, the surface potential measurements are 0th order flattened, as discussed above, and 3x3 median filtered in order to remove stochastic noise [225].

The Casimir pressure for parallel gold plates is calculated at 300 K, using the

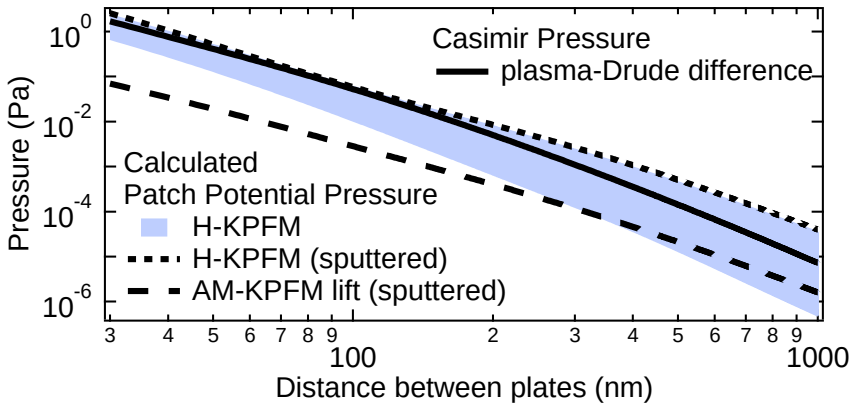

Figure 5.3: The pressure difference between the plasma and Drude models for the Casimir force ($P_{\text{difference}} = P_{\text{plasma}} - P_{\text{Drude}}$, solid black line) falls between the minimum and maximum patch potential pressures calculated from the e-beamed, sputtered and TSG surfaces (blue band). AM-KPFM (dashed line) predicts a much smaller force than H-KPFM (dotted line) for the same area (1 μm^2). All pressures displayed here are attractive.

plasma and Drude models with $\tilde{\gamma} = 0.035$ eV and $\tilde{\omega}_{\text{p}} = 9.0$ eV [2, 227] without the addition of optical data at other frequencies, both for simplicity and because optical properties vary based on preparation [30]. Although most Casimir force experiments are performed in a sphere/plate geometry, the calculation here remains in a parallel plate formulation, as the proximity force approximation is not sufficient to convert the patch potential pressure to a sphere/plate geometry [128].

The patch potential pressures computed from different samples varies by over an order of magnitude at a separation of 1 μm and by a factor of 4 at 30 nm (figure 5.3). The plasma-Drude pressure difference remains between the smallest and largest pressures calculated from the scans of the e-beamed, sputtered, and TSG surfaces with scan length of 1 μm over all distances from 30 nm to 1 μm.

5.1.5 Modeling patch potentials for Casimir force measurements

The potential variation and patch size distribution can be obtained from our measurements and used in simple patch potential models when the exact SP is unknown. Here we compare our measurements to the quasi-local model [15] (QLM), which takes the patch size distribution and V_{RMS} as inputs. In [15] it was suggested that in vacuum conditions, the grain size determines the patch potential size, while in ambient conditions, patch potentials result from adsorbates, and thus are larger in size but of less magnitude. The size of patches that we found in an image do not seem to correlate directly to the grain size of the material, as established from an AFM image. For example, in figure 5.1, the e-beam and sputtered samples have very similar topography, while the length scales of their patch potentials differ.

The surface potentials measured here, in ambient conditions, show variation on both small (30 - 100 nm) and large (300 - 1000 nm) scales, although the latter variation is of less magnitude and more sensitive to flattening. The smallest patches are of the same size as the tip radius, so it is likely that still smaller patches exist on the surface. Both preparation and scan size influence V_{RMS}, but in general it falls between 15 and 28 mV (after a 3x3 median filter to remove noise).

Two ranges of patch size are incorporated into the QLM to replicate the two observed scales of correlation. In [15], the QLM for one patch size gives

$$\mathfrak{C}(r) = \frac{2V_{\mathrm{RMS}}^2}{\pi} \int_r^\infty dl \Pi(l) \left[\cos^{-1}\left(\frac{r}{l}\right) - \frac{r}{l}\sqrt{1-\left(\frac{r}{l}\right)^2} \right], \tag{5.5}$$

with the probability distribution,

$$\Pi(l) = \frac{\Theta(l - l_{\min})\Theta(l_{\max} - l)}{l_{\max} - l_{\min}}, \tag{5.6}$$

where Θ is the Heaviside function, $l_{\min}$ is the smallest patch diameter and $l_{\max}$ is the largest. Here, multiple patch sizes are incorporated into the QLM by giving each different patch size range a different V_{RMS}. Correlations coming from both large patches with diameters $l_{\min}^{\mathrm{large}} < l < l_{\max}^{\mathrm{large}}$ and potential variation $V_{\mathrm{RMS}}^{\mathrm{large}}$ and small patches with diameters $l_{\min}^{\mathrm{small}} < l < l_{\max}^{\mathrm{small}}$ and potential variation $V_{\mathrm{RMS}}^{\mathrm{small}}$ are incorporated into $\mathfrak{C}(r)$. If the large and small patches are uncorrelated,

$$\mathfrak{C}(r) = \mathfrak{C}^{\mathrm{large}}(r) + \mathfrak{C}^{\mathrm{small}}(r). \tag{5.7}$$

This model allows the creation of autocorrelation functions where long-range correlations are present (to allow for adsorbates and contamination often unavoidable), while still considering the short-range correlations which cause most of V_{RMS} and gives a better approximation of the measured autocorrelation functions (figure 5.4a).

A simulation of patch potentials was used to conclude that patch potentials did not contribute to a measured force in [179]. Because the force-minimizing voltage, V_0, varied with distance in the simulation when patch potentials were present, the lack of a distance dependent V_0 led the authors to conclude the patch potential force was zero. The range of SP values ($\pm$ 90 mV) was similar to our observations,

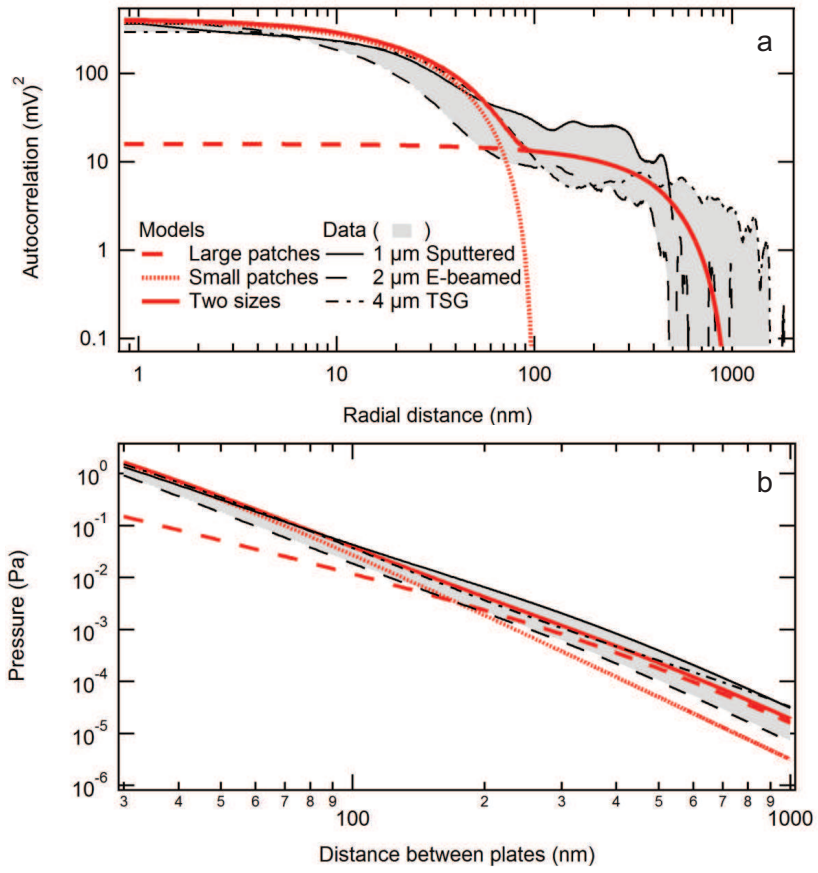

Figure 5.4: In the quasi-local model, neither small patches nor large patches alone match the $\mathfrak{C}(r)$ data from experiments; however, their combination, by equation 5.7, does (a). The parameters are, for small patches: $l_{\min} = 10$ nm, $l_{\max} = 100$ nm, $V_{\mathrm{RMS}} = 20$ mV, while for large patches: $l_{\min} = 500$ nm, $l_{\max} = 1\,\mu$m, $V_{\mathrm{RMS}} = 4$ mV using the uniform size distribution as in [15]. Consequently, two patch sizes also better approximate the calculated pressure from the measured data as well (b).

however, their spatial form differed. The potentials were modeled as square patches of side length s on a grid with spacing $l > s$. Outside the squares, the SP took on a uniform value. In our experiment, patches varied continuously, and there were small long-distance correlations not present in the simulated model. Distance dependence of V_0 is suppressed when the area of interaction ($2\pi Rd$, where R is the sphere radius, and d is the sphere/plate separation) is much larger than the average patch [126, 128, 228], here found to be about 100 nm across. Thus, V_0 distance

dependence may not be observed even if patches still contribute to the force for $d \gg \frac{r_{\text{patch}}^2}{2R}$, where r_{patch} is the typical patch radius.

5.2 Resolution of patch potential measurements

The tunable spatial resolution technique developed in section 3.2 is used to evaluate how well the patch potentials are being resolved. A 1 μm^2 region of gold on an e-beam deposited sample is scanned with TSR-KPFM, using signals amplified by $C^{(2)}$, $C^{(3)}$, and $C^{(4)}$, where $C^{(2)}$ is equivalent to H-KPFM used at the beginning of the chapter. The resolution improvement shows that the patches have a slightly larger potential difference between them than is estimated with H-KPFM alone. Because there is still some difference between the $C^{(3)}$ and $C^{(4)}$ signals, it is expected that further improvements to resolution would show that even with these signals, the patches are not completely resolved. At larger separations ($r > 20$ nm), the $\mathfrak{C}(r)$ shows a reduction for $C^{(3)}$ and $C^{(4)}$, perhaps because even with the $C^{(2)}$-dependent signal of H-KPFM, the resolution causes one patch to blend into another. However, the measurements with $C^{(3)}$ and $C^{(4)}$ agree closely with one another in the 50-80 nm range, it is expected that they are resolving the patch size accurately. The improved resolution increases the calculated force at separations < 70 nm, and decreases it at larger separations. However, we expect that the force estimate only decreases because the 1 μm^2 scan size is too small to observe the largest patches (see figure 5.2).

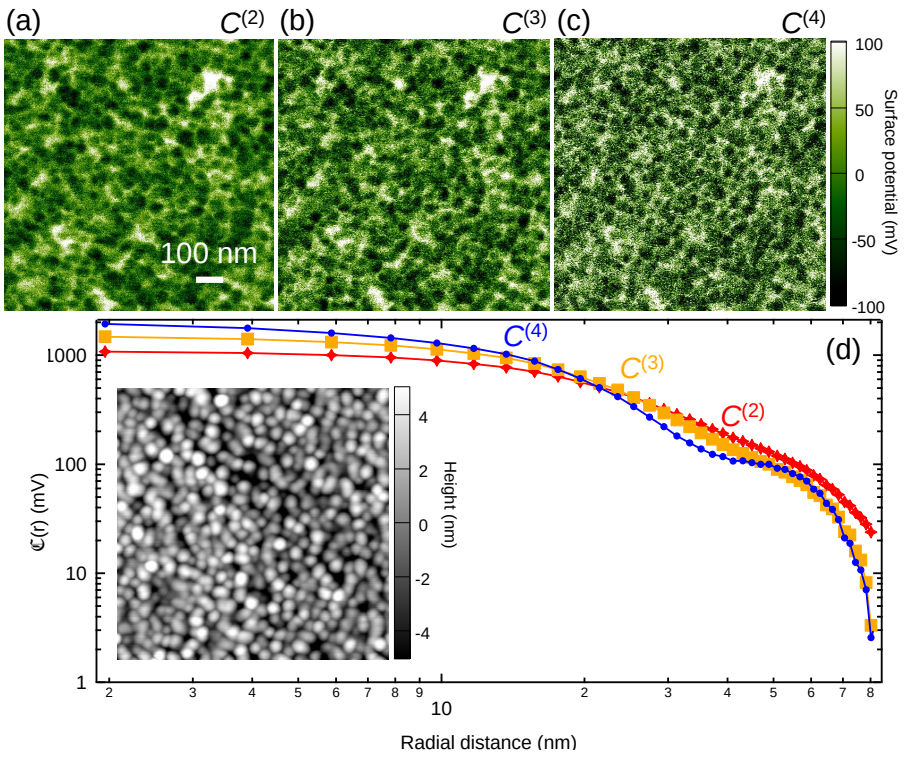

Figure 5.5: (a-c) TSR-KPFM is used to scan the same $(1\ \mu\text{m})^2$ region of a gold film as the spatial resolution is increased, by utilizing higher order derivatives of C (section 3.2, 512^2 pixels, 0.6 μm/s). (d) As the resolution is increased, $\mathfrak{C}(r)$ increases by about a factor of 2 for $r < 20$ nm, but decreases at larger r, showing that improving resolution helps to resolve the smallest patches. The inset shows the topography.

5.3 Humidity and patch potentials

In this section, the effect of humidity on patch potentials is determined by measuring the patch potentials directly with H-KPFM while the humidity is decreased. Because patch potentials are observed to occur at two different length scales on gold surfaces (figure 5.4), it is necessary to understand the origin of each of the length scales in order to control the patch potential force in Casimir force measurements. Behunin *et al.* [15] predict that adsorbates mask patch potentials in air. Because water molecules are likely to be the primary adsorbates, varying humidity is one way

to investigate their hypothesis. Moreover, because water layer thickness is identified as one of the major sources of error in determining the surface separation in section 4.3.5.3, spatially varying patch potentials from humidity indicate that the thickness of the water layer is not uniform.

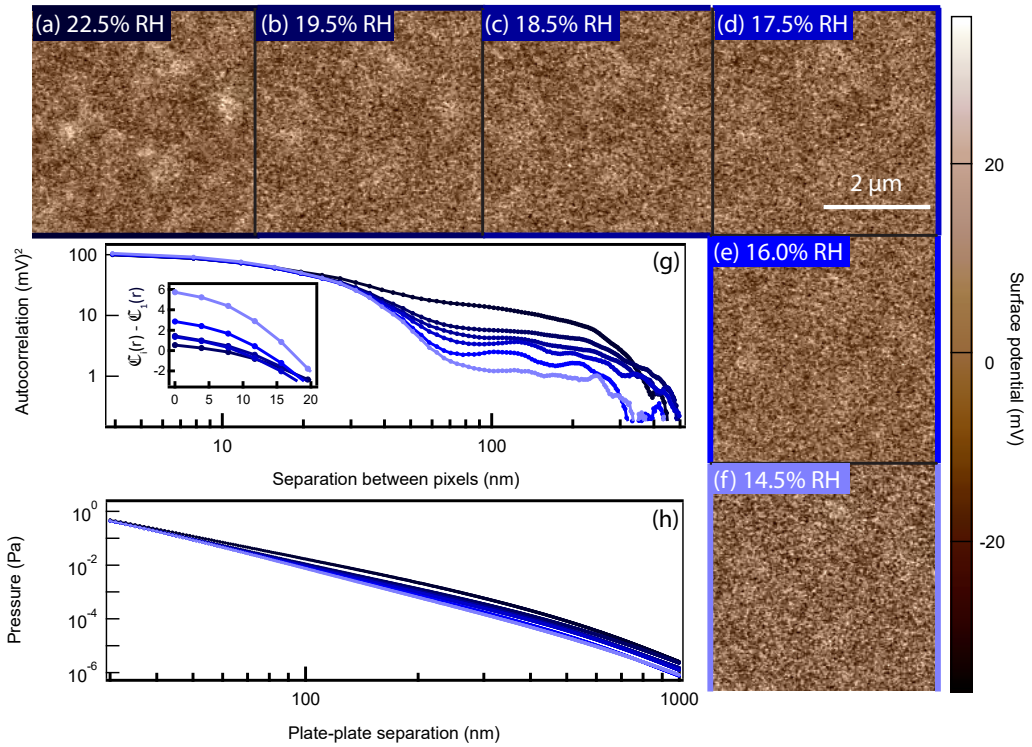

Figure 5.6: H-KPFM is used to scan the same $(4\ \mu\text{m})^2$ region of a gold film as the humidity is decreased (1024^2 pixels, 4 μm/s) (a-f). The autocorrelation function decreases by about an order of magnitude for $r > 80$ nm (g). The $\mathfrak{C}(r)$ are colored to correspond to the different humidities. The inset shows the difference between each $\mathfrak{C}(r)$ function and the original $\mathfrak{C}(r)$ at small r, where the autocorrelation function grows with decreasing humidity. The calculated patch potential force also depends on humidity (h).

Control of humidity is achieved by flowing dry air into the AFM scan chamber. While the air is flowing nine H-KPFM scans (six shown in figure 5.6), which each required half an hour, are recorded. Simultaneously, the humidity level is recorded with a humidity logger (Lascar). Because the humidity is changing during the

scans, they are organized by the humidity in the chamber when each scan starts (figure 5.7). The autocorrelation functions do show two sizes of patches (figure 5.6g).

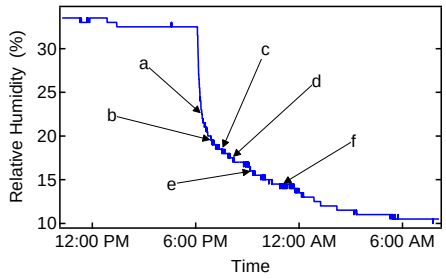

Figure 5.7: The humidity is controlled by flowing dry air into the AFM chamber. The time that a KPFM scan shown in figure 5.6 is started is indicated by an arrow.

The observation that $\mathfrak{C}(r)$ decreases with decreasing humidity by about an order of magnitude at large r suggests that water molecules are primarily responsible for the larger patch size, and that the water layer thickness varies across the sample. To the contrary, at short separations, $\mathfrak{C}(r)$ increases by a few percent with decreasing humidity. The increase is consisted with the idea in [15] that adsorbates screen the electric fields from some patches intrinsic to the gold surface. Note that the change in the screening is likely underestimated, because it occurs at a length scale comparable to the spatial resolution of H-KPFM.

5.4 Scanning on spheres

There are three distinct obstacles to measuring the patch potentials on the spherical probes. First, because the cantilever is held at 11 degrees below the vertical, the region on the sphere that is closest to the plate during a measurement is not the same region as is scanned when the probe is lying flat. Second, because

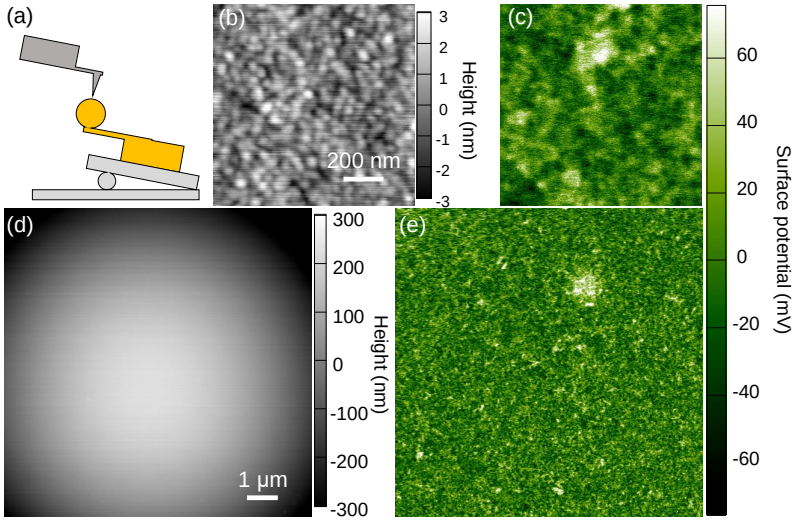

Figure 5.8: (a) The sphere is placed on a tilted surface to be scanned. (b,c) The topography and surface potential of a 1 μm^2 region on the sphere surface show patches similar to those on the plate. (d,e) A larger scan of the potential on the sphere shows the region that contributes much of the patch potential force.

the spring constants and resonant frequencies of the Casimir force probes are very low compared to those of the probes used for H-KPFM, the Casimir probes respond more to low-frequency excitations. Third, the curvature of the spheres causes multi-frequency AFM techniques to lose sensitivity away from the center of the sphere (see section 3.1). The first obstacle is overcome by building a stand to hold the Casimir probe at an 11 degree angle while it is being scanned. The second is overcome by using H-KPFM probes with resonance frequencies much larger than the resonance frequency of the Casimir probe. The third is overcome by using lower eigenmodes of the cantilever, most often the first, for signal detection. The variations of H-KPFM discussed in chapter 2 are used while topography control is maintained using a frequency slightly greater than the first eigenmode to stay in 'attractive' mode [157].

One of the first observations while scanning spheres is that many of spheres have patches much larger than those on the plate (figure 5.9). The origin of the

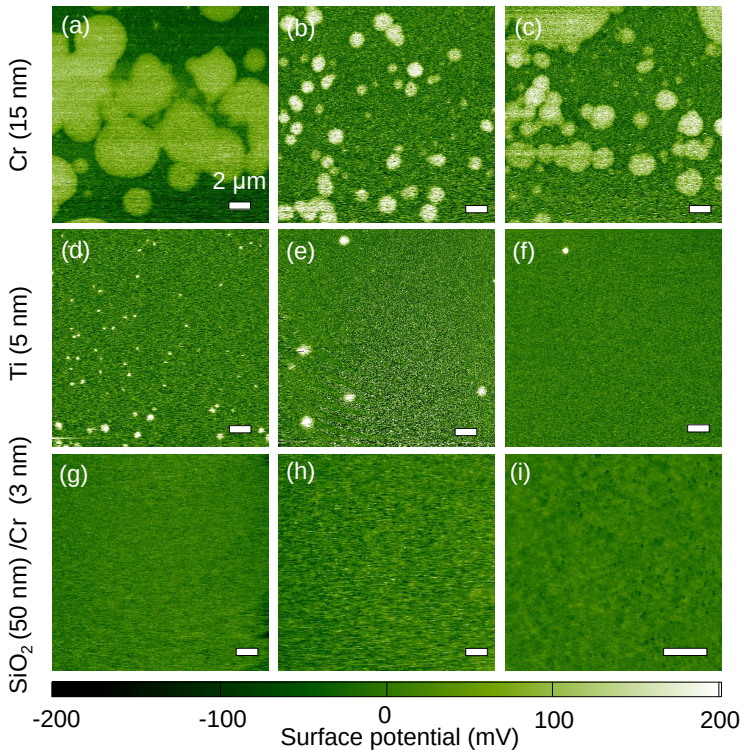

Figure 5.9: (a-c) Using a Cr sticking layer for the gold on glass results in micron scale patches. (d-f) A titanium sticking layer causes sub-micron patches. (g-i) Using a SiO_2 boundary layer between the glass and the gold mitigates the patches. The three columns show three different spheres with each sticking layer.

patches is investigated by changing the sticking layer on the spheres (Trelleborg SI-100). All the depositions begin by cleaning the sphere with contact mode AFM to remove dust/debris, followed by a acetone, isopropyl alcohol, and DI water rinse. The depositions are performed in an e-beam evaporator (Denton). The first deposition uses a 15 nm Cr sticking layer, the second uses 5 nm Ti, and the third uses Cr (3 nm) /SiO_2 (50 nm)/Cr (3 nm), before depositing 100 nm gold on top. Micron-scale patches are observed on the surface of the spheres with the Cr sticking layer, but the patches are reduced to sub-micron sizes with Ti. On the spheres that incorporate an SiO_2 blocking layer, the patches become too small to be observed. Because scan-

ning electron microscopy measurements with electron scattering diffraction show the presence of Ca on the spheres, the reduction in patches may be due to blocking Ca ions from entering into the gold.

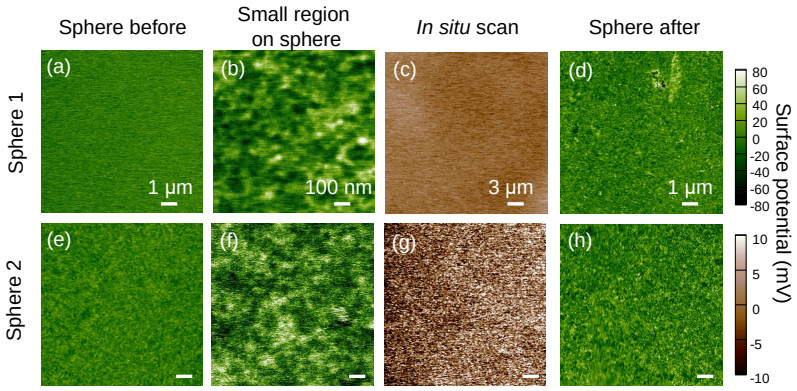

Figure 5.10: Two spheres are scanned with KPFM before a Casimir force measurement, to observe patches at large (a,e) and small (b,f) length scales. Before and after the force measurement, an *in situ* KPFM scan is performed (e,g). Another KPFM scan of the spheres after the measurement shows some change to the potential for one sphere (d), but the change is less clear for the other (h).

In order to understand the stability of the patches during a force measurement, H-KPFM scans of the spheres are recorded both before and after (figure 5.10). One 100 μm^2 image is recorded to evaluate the potential over the whole region of interaction. One 1 μm^2 scan is recorded in order to characterize the smallest patches. Once the probe with the sphere attached is loaded above the plate, it is used as the KPFM probe in order to measure the patches on the plate *in situ*, as in [221]. One sphere with a Cr sticking layer showed significant change to its patches from before to after the measurement, which indicates that in some situations patch dynamics may influence the measurement (figure 5.11). Some preprocessing (flattening, median filtering) is used to reduce the effects of line noise on the KPFM scans, but the preprocessing also means that the calculated forces may underestimate the total

electrostatic force, particularly from patches comparable to the scan size.

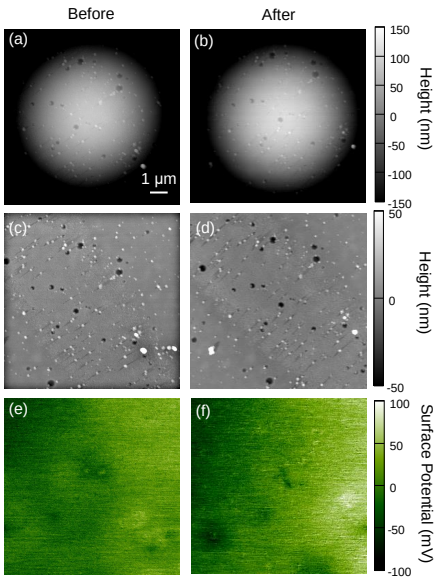

Figure 5.11: (a-d) The sphere topography changes little from before to after a force measurement. The top row shows the raw topography images. In the second row, the roughness is shown. (e-f) The potential on a sphere with chromium sticking layer, on the other hand, shows a noticeable increase in variation from before to after a force measurement.

The clearest signature of patch potentials in a Casimir force measurement is a minimizing potential, V_0 that varies with separation [126]. The PFA (equation 2.24) is used to calculate how the minimizing potential changes for the spheres used in the measurements (equation 4.33) [202]. The lower half of the sphere is modeled as a surface of parallel plates, each consisting of one pixel, above a larger, grounded plate (assumed to be a grounded equipotential). A point of closest approach is chosen for some point on the potential map, which is placed onto a sphere. The region of the sphere not covered by the image is assigned the voltage V_{macro}, which, for the calculations here, is taken to be the average of the KPFM image. To find the minimizing voltage, the force derivative with respect to the applied voltage is set

equal to zero, and then solved for the applied voltage. At each separation d, the voltage which must be applied to the sphere to minimize the electrostatic force is:

$$V_0 = -\left(V_{\text{macro}} + \frac{d}{2\pi R} \sum_{i,j} (V_{i,j} - V_{\text{macro}}) \frac{A_{i,j}}{h_{i,j}^2} \right), \tag{5.8}$$

where $h_{i,j}$ is the separation of the i,jth pixel of the sphere from the plate and $A_{i,j}$ is the area of the pixel. The V_0 are calculated for 49 points on a 16 μm^2 grid around where the point of closest approach on the sphere is expected to be. The calculation extends out to separations of 1 μm, because at larger separations V_{macro} becomes the dominant factor in determining V_0. The calculated V_0 are compared to the measured values in figure 5.12. The value of V_0 at closest separation is subtracted, because the variation in V_0 with distance conveys the information about patch potentials. The measured V_0 includes separation-independent offsets from the electronics connecting the sphere to the plate. The V_0 of sphere 1 is consistent with the calculated values up to the noise level. For sphere 2, the observed change in V_0 is several times larger than any of the calculated values.

Because the primary problem caused by patch potentials is the force gradient they impart into the signal, it is also investigated. The residual force gradient due to the measured patch potentials is determined from KPFM scans of the sphere both before and after the measurement using the PFA (equation 1.5) and equation 5.4. The calculated patch potential forces from the spheres are compared directly to the measured force (figure 5.13). For both spheres, the calculated electrostatic force gradient is less than the measured force gradient, which indicates that it is not

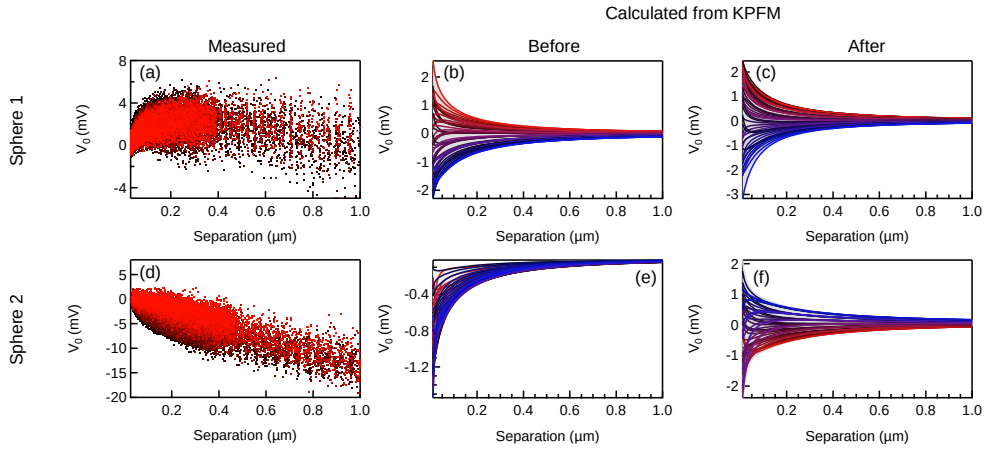

Figure 5.12: (a,d) The minimizing voltage (V_0) is measured during each Casimir force measurement. The data are recorded over many approach/retract cycles (changing from dark to light red over time). The V_0 is computed for 49 possible orientations of each sphere from both the (b,e) before and (c,f) after KPFM scans. Each line corresponds to one possible sphere orientation.

the electrostatic patch potential force gradient, but the Casimir force gradient that is being measured.

Even though the patches on the spheres can be significantly different from the patches observed on the plates, they can be controlled so that the contribution of the patches to the total force is much less than the Casimir force. The SiO_2 boundary layer is not necessary for the plate, because the plate already has a native oxide layer and Ca is probably not even present in the Si wafer. It is suspected that Ca diffuses out from the glass and into the gold when the boundary layer is absent, based on the composition of the glass. The diffusion of atoms from an interface into the bulk could be a problem in other precision measurements as well. For example, Wang *et al.* [229] discuss an experiment in which the isoelectronic technique[1] is used to mask the work function difference between two materials of different mass (gold and silicon), but

[1]In the isoelectronic technique, two different materials are coated with the same metal layer to eliminate electrostatic and Casimir force contrast between them [212].

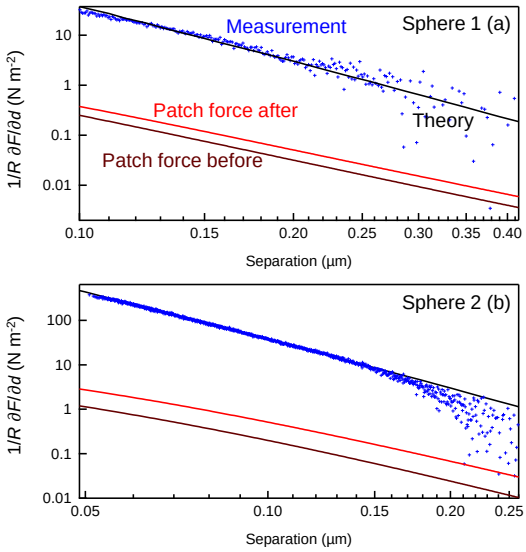

Figure 5.13: The measured force (blue, binned) is compared to the calculated Casimir force (black) and the calculated patch force (dark or light red) for both spheres (a,b). The patch force calculated from KPFM is much less than the measured force.

find that the electronic contrast is not eliminated by the gold coating until it is several hundred nanometers thick and annealed. The authors attribute the extra electrostatic force to patch potentials, which happen to align themselves with the masses below the isoelectronic surface. One possible explanation for the observation of the unusual patches is that ions, either from one of the masses or from residue from the fabrication procedure, are diffusing onto the surface. The experiments in this chapter show that some patch potentials can be effectively identified by KPFM and controlled through the use of a boundary layer. Due to developments pertaining to KPFM in liquids [230], a similar study of patch potentials should be feasible in liquid environments, which might have very different electrostatic patch potentials [192].

Chapter 6: Measurement of the Casimir force between two spheres

6.1 Overview

Many theoretical predictions regarding the Casimir force rely on complex interaction geometries, but measurements have traditionally been limited to sphere-plate or plate-plate configurations. Prior attempts to extend Casimir force measurements to new geometries either relied on intricate nanofabrication or slight modifications of the sphere-plate geometry. Here, measurements of the Casimir force between two gold spheres are alternated with topographical scans in the x-y plane in order to maintain alignment of the centers of the two spheres to within about 400 nm ($\approx$1 % of the sphere radii). Deviations from the proximity force approximation are bounded using 9 sphere-sphere and 3 sphere-plate measurements with spheres of varying radii.

6.2 Geometry in the theory of the Casimir force

The original derivation of the Casimir force between parallel plates results from the change of the quantum vacuum energy of electromagnetic modes in a metallic cavity as the separation between two walls changes [1]. The first calcula-

tions of the force for curved surfaces relied upon the proximity force approximation (PFA), in which each small portion of a curved surface interacts with a small portion of another surface [2, 28]. The inherent conflict between the global perspective of the original derivation and the local perspective of the PFA led to much theoretical work. Sharp edges lead to some of the strongest corrections to the PFA [53, 231, 232], while smoother surfaces allow a perturbative treatment [27, 233, 234]. Several new geometries have been proposed for nanoelectromechanical devices which utilize the Casimir force, including non-contact gears [54] and geometrically-controlled repulsion [53, 235, 236]. Even with modern algorithms, searching for corrections and identifying new geometries is computationally intensive and analytical results are specific to a few geometries for perfect conductors. Some analytical results for perfect conductors exist for geometries including: two spheres, nanoscale gratings on plates, crossed cylinder, a wedge above a plates, and a cone above a plate [231, 232, 234]. Measurements in new geometries would test and help guide such theoretical developments.

6.3 Prior experiments in new geometries

Despite the well-motivated theoretical investigation into exotic geometries, most experiments still rely on the sphere-plate geometry [8–11, 237], because it is insensitive to rotations and horizonal motions of the sphere. Other measurements have used a plate-plate configuration [18, 177, 238], which was used for the original derivation of the theory [1,6], but the relative angle between the two plates is difficult

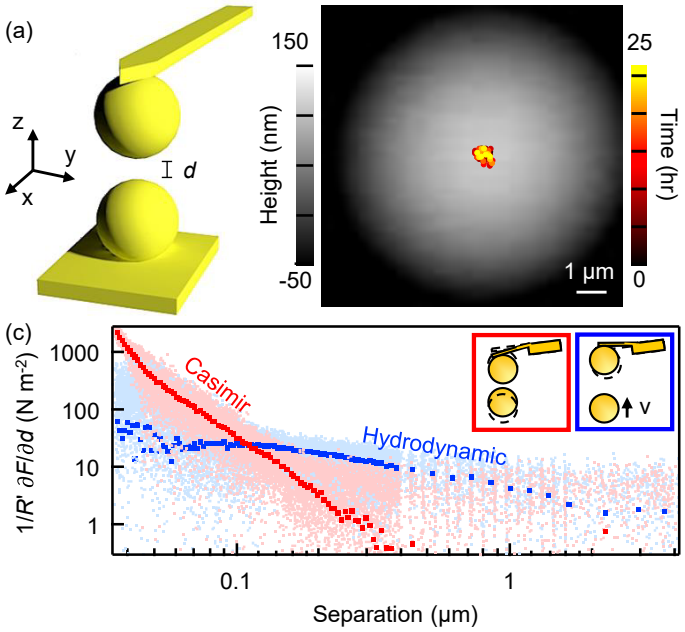

Figure 6.1: (a) One gold-coated sphere is held directly above another. (b) AFM scans are used to position the top sphere directly above the bottom sphere (scan speed:10 μm/s, 64×64 pixels). (c) During the force measurement, the hydrodynamic drag is separated from the Casimir force through the phase of the force signal. All the individual measurements (light) are shown ($\approx$ 20,000 points), as well as 200 point bins (dark). The inset shows the cantilever response to the Casimir (red) and drag (blue) forces.

to control and limits the precision of such experiments.

Two techniques have emerged to push Casimir force measurements into new geometries. The first begins with a sphere-plate geometry, but textures one or both surfaces, so that the alignment advantages of the sphere-plate configuration are maintained while effects beyond the PFA are probed [51, 52, 239]. The second involves fabricating two interacting surfaces out of a single crystal to ensure the alignment of the surfaces [13, 14]. However, measurements are limited to materials for which sufficient nanofabrication techniques exist. Some of the most interesting geometries, such as the needle-and-hole, for which a repulsive force is predicted [53], and sphere-sphere (figure 6.1a), for which a proportionally greater deviation from

the PFA is expected [26, 240, 241] require *in situ* alignment. The force between latex spheres in liquid has been measured by aligning the spheres using their optical interference pattern so that the horizontal distance between the two sphere centers was less than 0.1 R', where $R' = (R_1^{-1} + R_2^{-1})^{-1}$ is the effective radius of the two sphere system [242, 243]. The electric double-layer force dominated the measured force in one of the experiments [243], while in the other the Casimir force was separated from the electric double-layer force after the measurement through curve fitting, and a dispersive force was measured out to a separation of ≈30 nm [242].

6.4 Sphere-sphere measurement method

Here we present Casimir force measurements between two gold-coated spheres. To align the two spheres, The top sphere is attached to an AFM cantilever (Mikromasch USA) and is raster-scanned, while oscillating, over the bottom sphere. A piezoelectric transducer controls the height of the bottom sphere, so that the oscillation amplitude of the cantilever, and thus the separation, is maintained while an image is recorded (figure 6.1b). A fit to the resulting image allows for lateral alignment of the two spheres to within 400 nm, or about 0.02 R'. Misalignment between the two spheres results in three primary effects (described further in section 6.7): (1) the absolute separation of the two spheres can change by up to 1 nm, (2) the force sensitivity can change by up to ±0.3%, and (3) a discrepancy on the order of 0.05 nm may exist between changes to sphere-sphere separation and piezo displacement. A change in the absolute separation (1) is accounted for by increasing

expected separation uncertainty to ±3 nm (section 4.3). Changes to the sensitivity (2) are taken into account by increasing the calibration uncertainty to ±5.3%. The uncertainty imparted by (3) is small enough to be ignored. A commerical AFM (Cypher, Asylum Research) is used, and environment is maintained at 303.15±0.05 K and 14.5±9% relative humidity.

The Casimir force measurement procedure developed for ambient pressures by de Man *et al.* [11, 21] is utilized to estimate the separation, to calibrate the spring constant, and to eliminate hydrodynamic and electrostatic forces from the Casimir force measurement channel. Measurements are recorded at about ≈400 individual separations in each direction for each sphere-sphere configuration from 4 μm to 30 nm as the top sphere approaches and retracts from the bottom sphere. At each separation, the measurement is split into two steps, each of which take 0.7 s. The electrostatic measurement is performed first to minimize the electrostatic force and estimate the separation, and the force measurement itself is performed in the second step.

The electrostatic force is used to estimate the absolute tip sample separation, d_0, and the sensitivity as described in section 4.3. An AC voltage, V_{AC} is applied at frequency $\omega_{\mathrm{A}}/2\pi = 77$ Hz to the top sphere, while the bottom sphere is grounded. A second voltage, V_0, is applied by feedback to the top sphere in order to minimize the cantilever oscillation signal at ω_{A}, which in turn minimizes the electrostatic force, akin to a Kelvin probe feedback loop [21]. Then V_{AC} also generates a signal at $2\omega_{\mathrm{A}}$, called $S_{2\omega_{\mathrm{A}}}$. The magnitude of V_{AC} is controlled by a second feedback loop in order maintain a constant $S_{2\omega_{\mathrm{A}}}$. The absolute separation is estimated by fitting

capacitance d-gradient for an entire approach/retract sequence of measurements to the exact sphere-sphere capacitance gradient [244]. While fitting the capacitance gradient to estimate the height, the bending of the cantilever ($<$ 3 nm) is taken into account, and a water layer of 1.5$\pm$0.75 nm is included, as described in section 4.3.5.3. The water layer increases the Casimir force itself primarily at separations $<$ 10 nm [48].

The force gradient itself is measured by the amplitude modulation technique described in section 4.2. The bottom sphere is shaken with an amplitude Δd at frequency $\omega_{\rm pz}/2\pi$ = 211 Hz, and a lock-in amplifier records the response of the cantilever. We note that in sphere-sphere measurements, the hydrodynamic force is significantly less than in sphere-plate measurements, and so imparts less error. The shake amplitude is reduced from 48 to 1 nm on approach, to maximize the sensitivity at large separations, while also minimizing any artifact from the non-linearity of the Casimir force [184]. After the force measurements, the sphere again approaches and retracts from the surface, while electrostatic measurements are made with $V_{\rm AC}$ = 8 V to calibrate the optical lever sensitivity and the spring constant from the electrostatic signal at $4\omega_{\rm A}$.

The topography, force gradient measurement, and calibration cycle is repeated for about 24 hours for each sphere pair resulting in about 50 force-distance measurements per sphere-sphere experiment. A total of nine sphere-sphere and three sphere-plate measurements are recorded, with three different top spheres and three bottom spheres. The sphere radii (hollow glass, Trelleborg SI-100) range from 29-47$\pm$0.3 μm, and are epoxied to either a cantilever or a silicon substrate, and coated

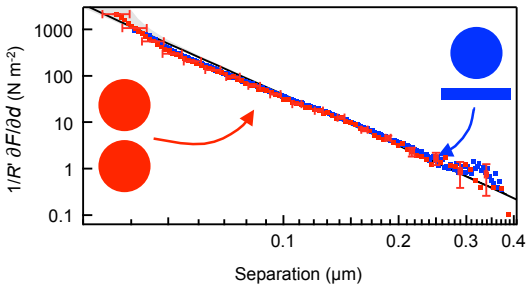

Figure 6.2: Representative measurements of the Casimir force for both sphere-plate (blue) and sphere-sphere (red) measurement geometries are compared to the calculated gold-gold Casimir force with a 4.9 nm RMS perturbative roughness correction (black). The gray region shows the uncertainy in the roughness correction, due to the uncertainty in the orientation of the spheres, as discussed in section 4.5.3.

(Denton E-beam) with Cr(3)/SiO_2(50)/Cr(3)/Au(100 nm). The silicon plate is coated with Cr(5)/Au(100 nm). Roughness is estimated from AFM scans on all surfaces after the deposition.

6.5 Comparing sphere-sphere and sphere-plate data

The data collected from the sphere-sphere measurements are first compared to data from sphere-plate measurements made using the same top sphere. The force gradient is normalized by R' to compare the measurements (figure 6.2). The Casimir force between the gold surfaces is computed by combining ellipsometry data over the range 0.74-6.3 eV with reference optical data [213] at higher frequencies and the Drude model with ω_p=8.84 eV and a 42 meV relaxation parameter at the lowest frequencies (as discussed in section 4.5.1) [227]. The AFM images of the surface are then used to estimate uncertainty in the roughness correction to the force gradient [201].

All the sphere-sphere measurements are shown in figure 6.3, together with the

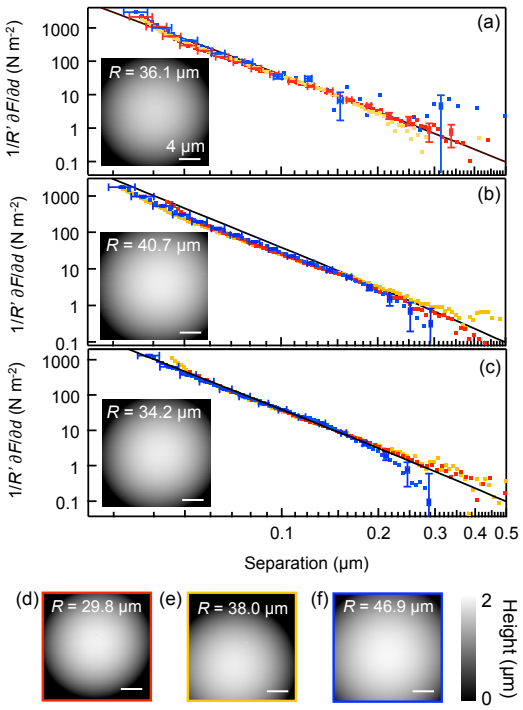

Figure 6.3: Casimir force measurements are performed between three bottom spheres (a-c) and three probes (insets). The measurements with each top sphere are presented in (d)-(f), where the different marker colors correspond to measurements on the different bottom spheres. The error bars in (d-f) indicate the uncertainty in the ambient water layer thickness (x-axis), and the uncertainty from the stray light effect (y-axis).

calculated Casimir force. At the shortest separations, roughness causes the force measurements to bend sharply upward, and at separations beyond 200 nm, stray light interference affects some of the data. Stray light appears as an artifact that is partially-periodic with separation, and is proportional to shake amplitude. Even though a superluminescent diode is used to minimize the stray light effect, it is present in some of the sphere-sphere data up to about 0.5 N m^{-2} (although it differs between measurements) and at about twice that level in the sphere-plate data due to increased reflection off the plate. Possible reasons that measurements with the top sphere in figure 6.3e show a smaller force at separations < 100 nm are that the

sphere has a deformity not captured by the roughness measurement [202], or that the slightly smaller k has led to an increase one of separation determination errors listed in 4.3.

6.6 Bounding corrections to the proximity force approximation

The PFA allows the force gradient between two spheres to be computed approximately from the force per unit area for parallel plates. However, theory predicts the presence of deviations from the PFA [27, 234]. To first order, the deviation is proportional to $1/R'$. The combination of sphere-sphere and sphere-plate measurements gives effective radii (R') that vary from 13-46 μm. The wide range of R' values allows the procedure of Krause *et al.* [237] to be used to put bounds on deviations from the PFA of the form:

$$\frac{1}{R'}\frac{\partial F}{\partial d} = 2\pi F_{\rm pp}\left(1 + \frac{\beta' d}{R'} + ...\right), \tag{6.1}$$

$$\approx (2\pi F_{\rm pp}\beta' d)\left(\frac{1}{R'}\right) + 2\pi F_{\rm pp},$$

$$= m\left(\frac{1}{R'}\right) + b, \tag{6.2}$$

where $F_{\rm pp}$ is the Casimir force per area between parallel plates, β' is a parameter defined in [237] to characterize how the force gradient differs from the force gradient predicted by the PFA, $m = 2\pi F_{\rm pp}\beta' d$ is the slope of the line and $b = 2\pi F_{\rm pp}$ is its intercept. Corrections to the PFA are expected to have the form of equation 6.1 because calculations of the correction with perfect conductors have shown such

a correction [234]. Moreover, numerical calculations show that for real materials, the form of the correction should be the same if β' is allowed to vary slightly with distance [27]. Intuitively, the $\propto R'^{-1}$ correction originates from the fact that the PFA is a better approximation for interacting surfaces with a larger R'.

All twelve measurements are combined to put bounds on β'. For each measurement, the data are binned at several separations, with bin widths that are 2% of the separation, *e.g.* one bin is 100±1 nm. All twelve force gradient measurements at one separation are then plotted versus $1/R'$ (figure 6.4). A line in the form of equation 6.2 is fit to the force gradients at each separation. Then β' is calculated from the fits:

$$\beta' = \frac{m}{bd} \,, \tag{6.3}$$

where m and b are determined from the line fit.

Of the the possible techniques to search for corrections to the PFA, the estimate of β' is more robust to several types of error than a direct comparison to the calculated Casimir force gradient. First of all, systematic uncertainty in the separation (due to, for example, a water layer) leads to a relatively smaller error than direct comparison of the force to theory, because the β' varies less with separation than the force itself [27]. Second, the phase and amplitude of the stray light, which leads to a systematic artifact in any one single measurement configuration, are effectively random between configurations, and so the total error stay light imparts is reduced. Finally, any overall systematic offset in the calibration common to all 12 sets of data

does not affect the estimate of β'. The error in β' for each separation is propagated from the error in each individual force measurement, which is in turn calculated from: uncertainty in the separation, uncertainty from roughness, uncertainty from calibration, uncertainty in the amount of the hydrodynamic force coupled into the Casimir force signal channel, uncertainty in V_0, and uncertainty in the interference effect as described in section 4.4.

To put our bounds on β' in the same form as Krause *et al.*, we find that $\beta' = -6 \pm 27$ is within 2-σ confidence interval of the calculated β' at all of the measured separations. Recent theoretical work has shown that calculating β' for real materials at finite temperature causes β' to be dependent on separation, contrary to the 0 K, perfect conductor limit [27], and so a separate estimate of β' is also shown for each separation (figure 6.4b). Stronger bounds on β' will be possible by extending the range of radii used in the measurement. The largest possible radius that can be used is limited by the ability to separate the hydrodynamic force from the Casimir force (the former scales as R^2, the latter as R). The smallest possible radius must still be large enough to contribute much more of the Casimir force gradient than the cantilever used to support it. Combining sphere-sphere and sphere-plate measurements to bound β' increases the range of the required line fit and should, all else being equal, increase the strength of the bound. If a large enough range of radii were used, it should also be possible to look for higher-order corrections to equation 6.1. As discussed above, the measurement of β' is less strongly affected by systematic errors than direct measurements of the Casimir force, and so should facilitate comparison between experiment and theory. Because β' is more sensitive

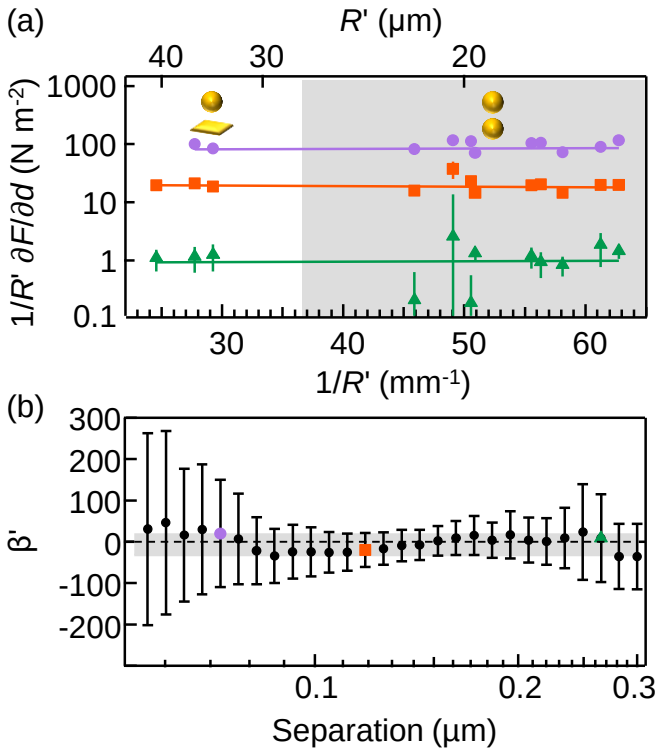

Figure 6.4: (a) For each separation, a line is fit to the measured forces gradients versus $1/R'$, where R' is the effective radius. Then, in equation 6.2, the slope of the line is $2\pi F_{\mathrm{pp}}\beta' d$ and the intercept is $2\pi F_{\mathrm{pp}}$. The graphics depict sphere-plate measurements on the left and sphere-sphere measurements on the right (shaded). (b) A value of β' is calculated from each line fit, and limits are placed on β' (grey box), chosen so that any β' within falls within the 2-σ confidence interval of the β' estimate at every separation.

to temperature and low-frequency conductivity that the Casimir force itself, in the range that is possible to measure with an AFM, it permits a second test in addition to direct force measurement to probe experimental oddities reported in the literature.

By combining topographical alignment with Casimir force measurements, the Casimir force between two spheres has been measured in the range 30-400 nm. The alignment method can be used to align any objects that may present interesting geometries for Casimir force measurements in air. The method can be adapted to liquid and should also be able to be adapted to vacuum conditions, though care will

be necessary to keep the spheres from contacting one another when drag is minimal. Once the objects are aligned any type of force can be measured: critical Casimir, hydrodynamic, thermal, etc. Even though the bounds on β' are significantly weaker than those set with the sphere-plate geometry, the ambient conditions in which these new bounds have been set indicate that it will be possible to incorporate geometrically controlled Casimir forces into MEMS devices.

6.7 Quantifying errors unique to the sphere-sphere geometry

A few sources of error not present in sphere-plate measurements (chapter 4) appear in sphere-sphere measurements due to lateral displacement the two spheres. The simplest way to describe the effect of lateral displacement between the two spheres is to consider the triangle outlined in figure 6.5a, which is described by:

$$[R_1 + R_2 + d']^2 = [R_1 + R_2 + d]^2 + \mathscr{L}^2, \tag{6.4}$$

where R_1 and R_2 are the radii of the top and bottom spheres, $\mathscr{L}$ is the displacement of the bottom sphere relative to the top sphere, $d = d_{\rm pz} - d_0$ is the shortest separation between the spheres when aligned along the $\hat{z}$-axis, d' is the separation between the two spheres when displaced by distance $\mathscr{L}$, $d_{\rm pz}$ is the piezo extension relative to its initial position, and d_0 is the piezo extension when the spheres are aligned and in contact. When the spheres are aligned, changes to $d_{\rm pz}$ directly change the separation between the spheres, but when they are misaligned, that is not longer the case. For the misaligned case, d_0' is defined to be the piezo extension for which the spheres

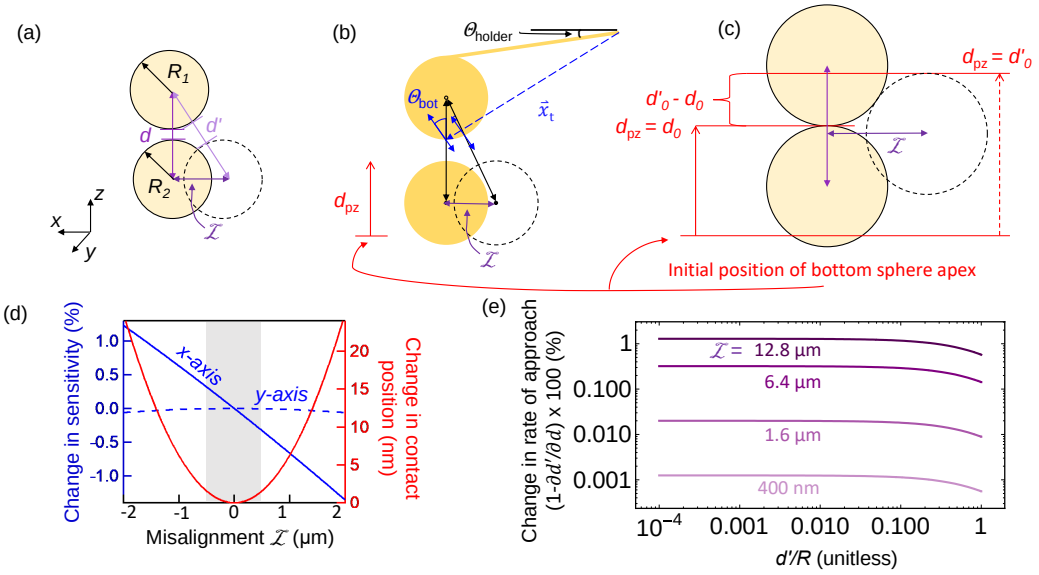

Figure 6.5: (a) The alignment of the two spheres is described in terms of the radii of the top and bottom spheres (R_1 and R_2), the lateral displacement of the centers, $\mathscr{L}$, the separation between the spheres if they were aligned along the $\hat{z}$-axis, d, and the separation between the spheres when displaced, d'. (b) The displacement affects the direction of the force on the top sphere and thus the sensitivity. (c) The piezo extension at which the spheres make contact when they are misaligned, d'_0, differs from the aligned contact position, d_0. (d) Both the sensitivity and the position at which the spheres make contact depends on the lateral displacement of the spheres. Because the change in sensitivity depends on the direction of displacement, labels indicate the axis along which the displacement $\mathscr{L}$ occurs. The displacements of the recorded measurements fall within the shaded region. (e) The rate of approach varies by a few thousandths of a percent when the bottom sphere is displaced by $\mathscr{L}$, which leads to an error that is much smaller than the separation uncertainty.

come into contact. In calculations below, $R = 40$ μm is used for both spheres.

6.7.1 Effective spring constant

The most consequential new source of error comes from changes to the effective spring constant (figure 6.5b). Because the Casimir force detection occurs at a frequency much below the resonant frequency of the cantilever, the cantilever's response to a force is approximated as a simple harmonic oscillator, with an effective

spring constant k for forces perpendicular to the sphere trajectory (equation 3.4). [1] Because deflection of the cantilever is detected, and because the bending mode is much more sensitive than the torsional mode, the torsional spring constant is neglected. However, the force applied to the bottom of the sphere is in a different direction than the sphere trajectory, so an effective sensitivity, B', is defined. One of the benefits of calibrating the measurement with the electrostatic force is that it is collinear with the Casimir force, and so no overall correction needs to be applied to the spring constant. However, when measuring the force between spheres, it is possible that the sensitivity changes over the course of a measurement if the spheres become misaligned.

To estimate the size of the misalignment effect, we treat the cantilever-sphere probe with a rigid-arm model. The cantilever has length L, is tilted by the holder to angle θ_{holder}, and the top sphere is effectively a 'tip' with height $2R_1$, so that the position of the bottom of the sphere relative to the base of the cantilever is (figure 6.5b):

$$\vec{x}_{\text{bot}} = L\cos(\theta_{\text{holder}})\hat{x} - (L\sin(\theta_{\text{holder}}) + 2R_1)\hat{z}. \tag{6.5}$$

The motion of the bottom of the top sphere is then perpendicular to this direction,

[1] The spring constants of higher eigenmodes are neglected because they are much greater than k and so minimally affect the response of the cantilever (equation 3.4).

so that the angle of the sphere's motion relative to the vertical is:

$$\theta_{\text{bot}} = \arctan\left(\frac{L\sin(\theta_{\text{holder}}) + 2R_1}{L\cos(\theta_{\text{holder}})}\right), \tag{6.6}$$

and displacements will be along the vector $\vec{r}_{\text{bot}}$:

$$\hat{r}_{\text{bot}} = \sin(\theta_{\text{bot}})\hat{x} + \cos(\theta_{\text{bot}})\hat{z}. \tag{6.7}$$

The cantilever's response to a force in direction $\hat{F}$ is then $\propto |\hat{F}\cdot\hat{r}_{\text{bot}}|$. Because the signal is generated by shaking the bottom sphere along the $\hat{z}$-axis, the force that drives the cantilever from the piezo shake Δd is $\propto |\hat{F}\cdot\hat{z}|$. The ratio of the sensitivity of the displaced probe, $B'(\vec{\mathscr{L}})$ to its aligned sensitivity is calculated in order to determine the percent change in sensitivity:

$$\frac{B'(\vec{\mathscr{L}})}{B} = \frac{|\hat{F}\cdot\hat{r}_{\text{bot}}||\hat{F}\cdot\hat{z}|}{|\hat{z}\cdot\hat{r}_{\text{bot}}|}. \tag{6.8}$$

The percent change in the sensitivity is calculated from the above ratio. The other sources of error depend only on the magnitude of displacement, not its direction, so the magnitude $\mathscr{L}$ is used to characterize displacement again.

6.7.2 Separation offset

The change in the position of contact due to lateral displacement leads to a second source of sphere-sphere error (figure 6.5c). The piezo extension, d_{pz}, at which

the spheres are in contact changes by the amount $d_0' - d_0$ when the bottom sphere is displaced laterally by $\mathscr{L}$. Using equation 6.4, the change in the position of contact can be found:

$$d_0' - d_0 \approx \frac{1}{2}\frac{\mathscr{L}^2}{R_1 + R_2}. \tag{6.9}$$

Thus, a lateral displacement causes the top sphere to seem further from the bottom sphere, and the dependence is quadratic in $\mathscr{L}$. The separation offset is plotted in red in figure 6.5d. The lateral displacement leads to a separation that is up to ± 1 nm, which is about 3% of the separation at closest approach.

6.7.3 Effective piezo displacement

The third source of sphere-sphere error originates from the difference between d and d'. When $\mathscr{L} = 0$, the position of the bottom sphere, controlled by the piezoelectric transducer, changes at the same rate as the separation between the two spheres. However, when $\mathscr{L} \neq 0$, the separation between the two spheres d' changes more slowly than the position of the piezo. To quantify the rate of approach, $\frac{\partial d'}{\partial d}$, we take the derivative of d' with respect to d, using equation 6.4:

$$\frac{\partial d'}{\partial d_{\mathrm{pz}}} = \frac{\frac{d'}{R_1+R_2} + \sqrt{1 - (\frac{\mathscr{L}}{R_1+R_2})^2}}{\sqrt{\left(\frac{d'}{R_1+R_2} + \sqrt{1 - (\frac{\mathscr{L}}{R_1+R_2})}\right)^2 + (\frac{\mathscr{L}}{R_1+R_2})^2}}. \tag{6.10}$$

In the $\frac{d'}{R_1+R_2} \ll 1$ limit, the effective piezo displacement becomes a constant,

$\partial d'/\partial d_{\mathrm{pz}} \approx \sqrt{1-(\frac{\mathscr{L}}{R_1+R_2})^2}$. The difference of the effective piezo displacement from one, $1-\partial d'/\partial d_{\mathrm{pz}}$, is plotted in figure 6.5e. For 400 nm misalignment, the most extreme value expected in the measurements, $1-\partial d'/\partial d_{\mathrm{pz}} \approx 0.001\%$, which amounts to about a 0.05 nm offset over the whole electrostatic measurement range ($\approx 5\ \mu$m).

Chapter 7: Epilogue

In the preceding chapters of this thesis, the effects of geometry and patch potentials on Casimir force measurements have been tested. The first two chapters characterize and develop KFPM, which is used later to measure patch potentials in Casimir force measurements. In Chapter 2, the spatial, temporal, and voltage resolution of heterodyne Kelvin probe force microscopy technique (H-KPFM) is measured and compared to earlier implementations of KPFM. H-KPFM is shown to achieve a spatial resolution of ≈ 40 nm, a voltage contrast of ≈ 20 mV with a 200 Hz detection bandwidth, and scan speed of up to 32 μm/s. H-KPFM is also found to avoid a number of artifacts, which afflict AM-KPFM. Chapter 3 discusses how cantilever dynamics can be utilized to improve H-KPFM. The first section discusses how the tip-trajectory of an AFM cantilever affects the KPFM signal and can even change its sign, and how judicious choice of the cantilever can mitigate its effect. The second section discusses how spatial resolution can be controlled by using higher derivatives of the tip-sample force to amplify the KPFM signal.

The subsequent chapters discuss measurements of the Casimir force. The force measurement method is introduced and characterized in Chapter 4. The technique is shown to have a 2 pN force sensitivity when all the current sources of error (opti-

cal interference, the hydrodynamic force, *etc*) are present, and could feasibly reach a 10 fN sensitivity if all the sources of uncertainty except thermal noise are eliminated. KPFM is used measure patch potentials and investigate their preparation-dependence in Chapter 5. Patch potentials are measured on both the sphere and the plate in order to characterize the total electrostatic force in the measurements. The patch potential force is found to be nearly two orders of magnitude smaller than the Casimir force. Chapter 6 presents measurements of the Casimir force between two spheres and uses the measurements to bound deviations from the proximity force approximation to $\beta' = -6 \pm 27$. Finally, this chapter summarizes the content of the thesis and discusses several additional ideas and extensions of the current work which could be explored in the future.

7.1 Future Work

Here a few additional ideas and extensions of the current work are discussed. Future experiments that relate directly to the work in one of the chapters are discussed therein, but some ideas did not fit neatly in any of them and are discussed here. These concepts include artificial patch potential forces and imaging defection motion on graphite.

7.1.1 Switchable Casimir force

The discovery of a material that can be used to switch the Casimir force at 100 Hz or more would have many uses in MEMS technology, for example, as an

actuator or a switch. Early attempts to measure a change in the Casimir force between a hydrogen switchable mirror and a gold plate reported that the change in force was below the noise level [245], possibly because of a Pd capping layer [246]. One group reported a successful *in situ* force modulation through charge-carrier density modulation using laser illumination [49], although questions remain about additional electrostatic contributions [32]. A more robust measurement of a switchable Casimir force has been performed between Au and Ag-In-Sb-Te (AIST) [50], but the switching is slow because the sample must be annealed. A promising route would be to measure the Casimir force between VO_2 and another surface, because its phase transition can be driven with an electric field [247], and occurs over sub-picosecond timescales [248], which is certainly fast enough to actuate MEMs devices.

An actively switchable Casimir force would also open up the possibility of new measurement techniques. For example, the method developed in chapter 4 measures how the Casimir force changes with separation by oscillating the plate. With a switchable force, it is not necessary to modulate the plate's separation, because the dielectric properties of one of the material could be modulated instead. Thus a force gradient measurement could be changed into a force measurement, but unlike deflection force measurements, the signal could still be measured with a lock-in amplifier. Because the force follows a more gradual separation dependence than its gradient, measuring it should expand the range of possible measurements. A basic form of this technique is used in [49], but care would need to be taken to exclude any artifacts that appear from driving the phase transition. Moreover, if

the material used to switch the Casimir force were built into an AFM probe, the TSR technique discussed in section 3.2 could be used to image variations in the Casimir/vdW forces across a surface.

7.1.2 Artificial patch potentials

In contrast to the Casimir foce, which only a few experiments report altering by 50% or more [10, 11], the force from patch potentials should, in principle, be controllable by over an order of magnitude at any one separation. To model the force from patch potentials, the quasi-local model (QLM) is used [15]. In the simplest case, two materials are randomly distributed on the plate to form metapatches, so that the potential difference between them is ΔV, they both have a characteristic diameter l, and the relative proportion of the first material is x. Then the patch potential pressure calculated from the quasilocal model is:

$$P(d) = \epsilon_0 x(1-x)\Delta V^2 \int_0^\infty k dk \left[\frac{J_0(\frac{kl}{2})}{\sinh kd}\right]^2, \tag{7.1}$$

where J_1 is a Bessel function, and P has been separated out from the rest of the patch potential pressure by assuming that the metapatches are not correlated with the intrinsic patches. The magnitude of the pressure is calculated assuming the two materials are Pt and Au, because both are relatively stable in air, even though their orientation-averaged work function difference is small (0.24 eV), and the characteristic patch diameter, l, is varied from 1 to 1000 nm (figure 7.1).

Metapatches could be fabricated a number of ways, from conductive polymers

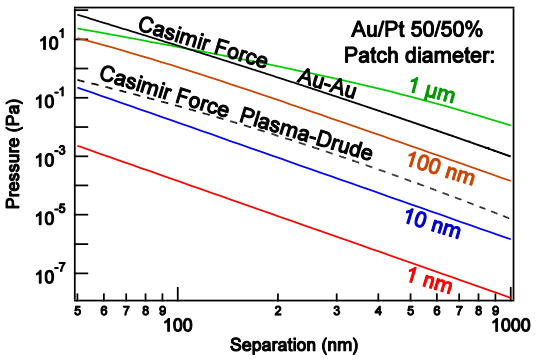

Figure 7.1: The pressure from Au-Pt metapatches is calculated for patch radii ranging from 1 to 1000 nm. At any one height, the pressure can be controlled by about two orders of magnitude, but forces less than the plasma-Drude difference could not plausibly be measured.

[100] to uneven semiconductor doping. One possible way to ensure that the plate is flat, even though it consists of two materials, is to fabricate the surface by template stripping [249]. Gold nanoparticles would first be fabricated on mica by annealing a thin film [250], and would then be back-filled with platinum (figure 7.2). When the metallic surface is stripped from the mica, a random distribution of metapatches would be exposed. Depending on the size of the patches, it may be possible to measure the patch force via the method described in chapter 4.

7.1.3 Defect motion on highly ordered pyrolytic graphite

One of the most interesting phenomena that appeared while evaluating the resolution of H-KPFM is the motion of a defect on a highly ordered pyrolytic graphite (HOPG) surface (figure 7.3). The defect is observed to move around near a boundary on a newly cleaved HOPG surface. The defect is only about 150 pm deep, but grows up to several 100 nm across and constantly changes its shape. The defect

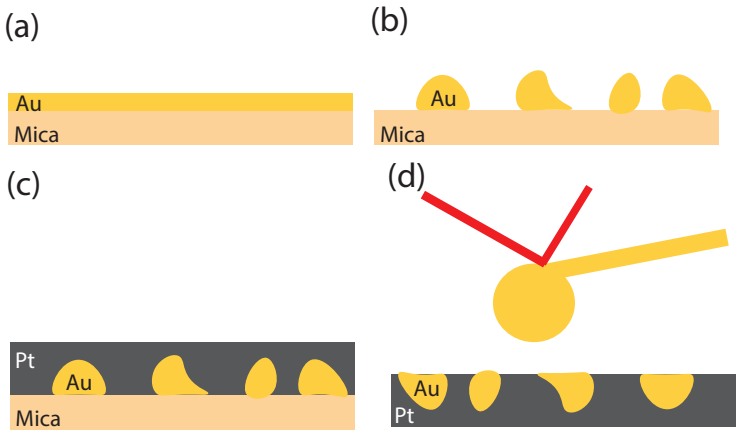

Figure 7.2: To fabricate metapatches, a thin gold film is deposited on mica (a). Annealing the film creates nanoparticles (b). The nanoparticles are backfilled with Pt (c). An atomic force microscope could be used to measure the patch force (d).

is suspected to either be due to adsorbates, or the absence of adsorbates, but the chemical identity of it is not known.

Defect motion has been observed before with AFM [251], but investigating it is pertinent to the work discussed in the previous chapters of this thesis for three reasons: (1) measuring the fluctuating potentials should help illuminate the origin and stability of patch potentials generally, including those on gold, (2) using H-KPFM to simultaneously measure both the defect's potential and position will help to understand the energy landscape that the defect is moving though, and (3) if it were possible to image the motion of two nearby defects, or a defect and a wall, sufficiently long, it should be possible to determine the in-plane force between them. Fluctuation-induced forces, such as the Casimir force, are likely to be a major constituent of the total force[1] in the $>$ 1 nm separation regime, just as they are for three dimensional objects.

[1]The force could possibly be between a defect and another defect, between a defect and a wall, between a defect and grain boundary, or between a defect and any other structure on the surface.

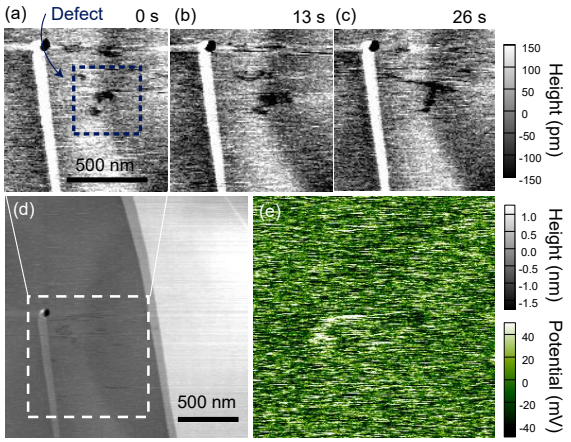

Figure 7.3: A defect is imaged on an HOPG surface at a scan rate of 13 s/scan (a-c). The defect is seen to change in size and position. A larger H-KPFM scan shows that its potential is about ≈40 mV greater than its surroundings (d,e).

7.1.4 Additional geometries

Many more geometries are possible for Casimir force measurements beyond those explored in chapter 6. The most prominent new geometry discussed in that chapter is the needle-and-hole geometry, which has been predicted to give repulsion [53]. The interplay of materials and geometry poses some questions that cannot be clearly answered yet. Both magnetic and topological materials have been predicted to give a repulsive force under certain conditions [252–256], and it is not clear what will happen when those materials are combined with a geometry that would give repulsion between metals. Further, earlier measurements with gratings observed very different behavior for semiconductors than for metals [51, 52].

Appendix A: Programming and user interfaces

I designed user interfaces to facilitate accessibility and reproducibility for the Casimir force and Kelvin probe experiments, because they simplify operation and enables other user to perform similar experiments. Here I describe a bit about how to use the interfaces, and a basic description of how each program works. Because the experimental techniques are described in the main text, I will refer the reader back to the text for information on the measurement technique, and here focus on the particulars of implementation and usage.

The first thing that other students of physics will notice is that none of this code is written in Labview. For that, I have Asylum Research to thank, for their use of a non-standard, but much more logical and useful programming language (Igor Pro). Still, Igor Pro has its own oddities, the most prominent of which is that it stores data in what it calls 'waves', which are 1-4 dimensional arrays in which the data on the arrays are evenly spaced to enhance the speed of some procedures, such as Fourier transforms, autocorrelation, *etc.* Igor Pro 6.37 is used for all the coding and the work done in this thesis, as the Cypher AFM is only compatible with that version (at this time). More information about the Igor Pro programming language can be found in the Igor Pro User Manual, particularly in chapters 4 & 5 [257].

Because Kelvin probe force microscopy and Casimir force measurements require many of the same operations, much of the code is reused (with slight variation) in all the programs. Because of this, and because of the quirks of the Igor programming language, each of the codes described in the three following sections must be used separately from the code in the other two sections.[1]

To satisfy the competing interests of simplicity and clarity, I use bold text to refer to **buttons or other components of a panel** and italic text to refer to *waves*. Functions, the third component of Igor programming, are already demarcated with parentheses.

In the interest of space, the code itself is not reproduced here, as each program would probably be a few hundred pages. Instead, the code is available on the MundayLab drive. On the MundayLab Cypher computer, the Kelvin probe and Casimir force codes can be loaded from the **Programming → Load User Func...** menu on the top navigation toolbar, after the Asylum Research software has already been launched.

A.1 Kelvin probe force microscopy panels

Kelvin probe force microscopy (KPFM) is discussed first in the main body of the thesis text (chapter 2), because it is the simplest of the techniques, and because variations of it are used in the Casimir force measurement as well. For the same reasons, we discuss the KPFM panels first here as well.

[1] An ambitious student could perhaps remedy my programming redundancies and bring all the code back under one roof, but the benefits of such an action are not readily apparent to me.

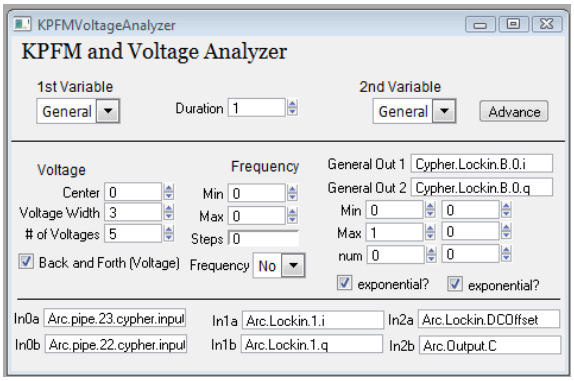

Figure A.1: The Parameter Sweep panel.

There are three KPFM panels: a parameter sweeping panel, a KPFM operation panel, and a voltage feedback panel. They are displayed automatically after the KPFM code is initialized from KPFMAnalyser.ipf.

A.1.1 Parameter sweeping panel

The parameters sweeping panel allows the AFM user to select an internal parameter or two to sweep, to set up to 6 channels (limited by Cypher hardware) for data acquisition, and to set the duration of the data acquisition (figure A.1). It is particularly useful for investigating the effect of a parameter upon data acquisition. The panel is divided into three by horizontal lines. Several options are available to sweep, but the three most useful are voltage, frequency, and general. Voltage is a special case of general, but is separated because it is the most common parameter to sweep. Frequency is a separate option because the way the Cypher AFM changes frequency is somewhat different than the way that other parameters are changed[2].

[2]If the frequencies are changed slowly, it is easier to use the General option.

To choose one of these options, go to the popup menu[3] under the words **1st Variable** and select an option. Note that it is possible to sweep two parameters at once, by also selecting a term from the **2nd Variable** popup menu. To sweep only one variable, set the **2nd Variable** popup menu to 'none'.

For voltage, the **center** voltage (typically 0), **voltage width**, and # **of Voltages** must be chosen. For frequency, the **min** and **max** frequency must be chosen. To sweep any other parameter, use the **general** option and write the name of the parameter in the **General Out 1** box (if it is the first variable) or **General Out 2** if it is the second variable. For each of these **min**, **max**, and **num** must be chosen. Furthermore, if the **exponential?** box is checked, then the parameter values to be swept through are exponentially, instead of linearly, spaced. The **exponential?** option is particularly useful for mapping out transfer functions, when a over an order of magnitude of values must be tested. To select which 6 data channels are collected during the sweep, write the name of the data to collect in the **In** boxes at the bottom of the panel. Each input (**0**, **1**, or **2**) can read in two data streams (**a** or **b**) from the ARC controller. Note that the inputs must come from the ARC controller, not from the Cypher itself. To extract a signal from the Cypher, it must first be connected to the pipe which connects the Cypher to the ARC controller (figure A.2).

After the parameters to sweep and the data to measure are chosen, **Advance** starts the measurement. The default duration for each setting of the parameter sweep is 1 second and it can be changed with **Duration** box. To plot the acquired

[3]Yes, that is the technical term used in the Igor Pro manual [257].

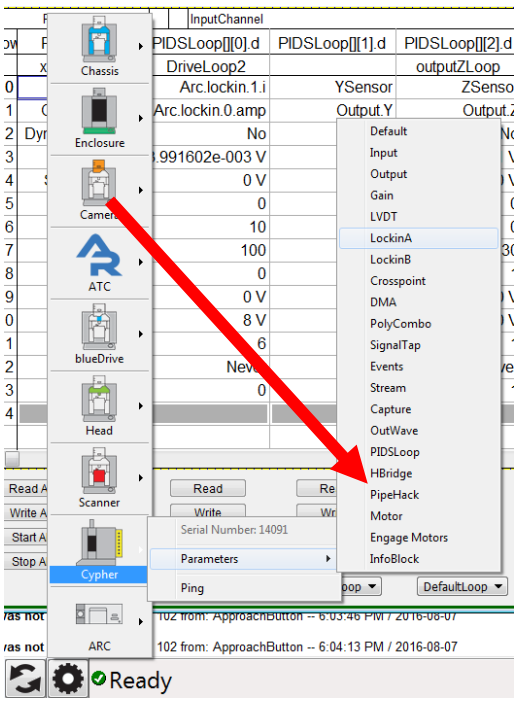

Figure A.2: The **Cypher** internal **parameters** includes **PipeHack**, which can be used to move signals from the Cypher to the ARC controller, so they can be recorded by the computer. The large red arrow is pointing to **PipeHack**.

data press **plot**. The first parameters are plotted on the x-axis and the second parameters are plotted by varying the color (dark→light). Other plotting styles can be used by plotting from the Igor command line. Each time **Advance** is pressed, it overwrites the previously recorded data, unless that data is saved in a new *wave*.

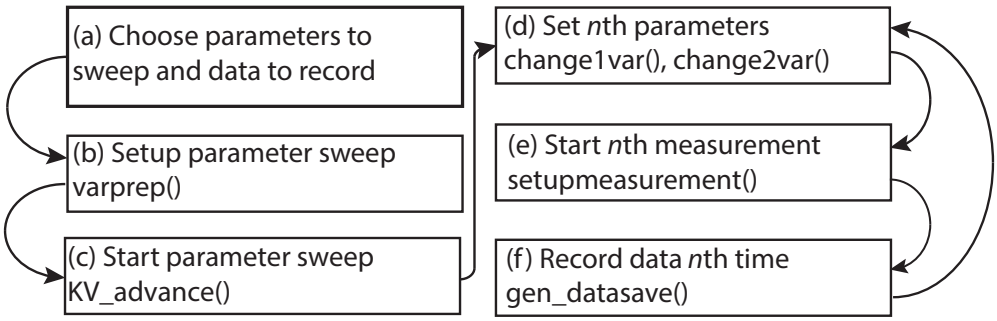

Figure A.3: To use the parameter sweeping panel, (a) select the parameters to sweep, and set the range of values to sweep. The parameters to be swept are set in *voltages*, *frequencies*, *general1*, or *general2*. (b) To setup the parameter sweep, run varprep(). (c) Then, if no error message appears, running KV_advance() starts the measurement. Pressing the **Advance** button is equivalent to steps (b) and (c). Once KV_advance() is called, the main measurement loop starts. (d) First, the parameters for the one measurement are set. (e) Next, the data channels are setup and the measurement is started. (f) After the measurement is finished, the data are stored. If one variable is being used, the averaged data is stored in *prelims*, and the raw data is stored in *alldata* (table A.1). Unless a sensitivity vs. noise analysis is necessary, the data in *prelims* is typically sufficient. If both variables are swept, then the averaged and raw data will be stored in *prelims2nd* and *all2*, respectively. The sequence (d)→(e)→(f) is repeated until all measurements have been made for all the input parameters.

Table A.1: Key data waves in Parameter Sweep panel

Wave Name	Description
prelims, prelims2nd	The time-averaged data, for one or two swept parameters
alldata, all2	The raw data (sampled at 5 kHz), can be useful for noise analysis
voltages	The voltages to be swept through
frequencies	The frequencies to be swept through
General1, general2	The values that the parameters are set to during the sweep
vars	The record of which parameter settings are currently set
to_measure	The six data streams that are recorded
output	The two parameters that are swept with the **General** options

Table A.2: Key commands of Parameter Sweep panel

Command	Description
varprep()	Sets up a parameter sweep, outputs total number of points in *alldata*
kv_advance()	Starts parameter sweep
setupmeasurement()	Sets up and runs a single measurement
gen_datasave()	Saves data recorded with the **General** options

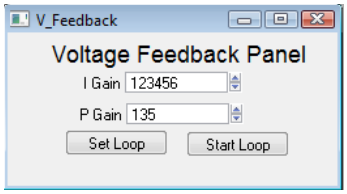

Figure A.4: The voltage feedback panel.

A.1.2 Voltage feedback panel

The small voltage feedback panel controls the voltage feedback loop. The listed and adjustable **I Gain** and **P Gain**, are set when **Set Loop** is pressed, and are adjustable even after **Start Loop** has been used to start the voltage feedback loop. The panel is small because keeping it visible is useful, as **I Gain** and are two of the most commonly adjusted parameters. For H-KPFM, **I Gain**≈50,000 and **P Gain**≈100. For FM- and AM-, the gains should be a little lower.

A.1.3 Operate KPFMs panel

The Operate KPFMs panel is used to setup and run the KPFM scanning (figure A.5). The panel allows the user to choose the KPFM **Mode**, sets up the Cypher's **Crosspoint**, and tunes the phase of the many KPFM signals. The KPFM technique is discussed in depth in chapter 2, and so here the focus is on how, operationally, can a Cypher user go about setting up KPFM.

To begin KPFM operation, it is necessary to first set up Amplitude Modulation AFM topography scanning, which is explained in the Cypher user guide [258]. Once topographical feedback is set up to maintain tip position, setting up the KPFM loop can begin:

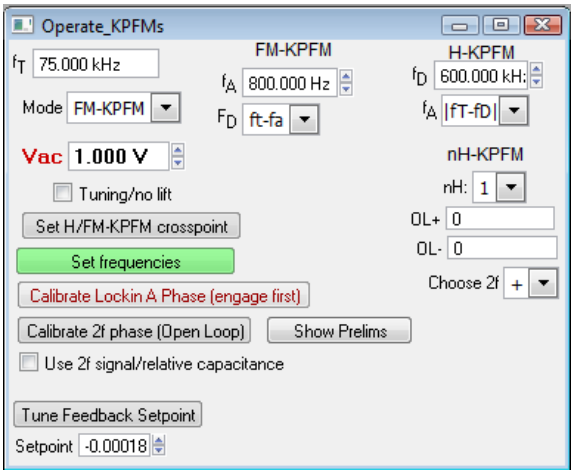

Figure A.5: The KPFM operation panel.

1. Choose which mode of KPFM to use.

2. Set frequency $\boldsymbol{f_A}$ or $\boldsymbol{f_D}$, for FM- or H-KPFM, respectively

3. Pick the positive or negative $\boldsymbol{f_D}$ or $\boldsymbol{f_A}$, for FM- or H-KPFM, respectively

4. Choose what **Vac** should be applied to the probe

5. Check **Tuning/nolift**

6. Press **Set H/FM-KPFM crosspoint**

7. Set **nH** to **1** (H-), **0** (AM-), or **>1** (TSR-KPFM)

8. Press **Set frequencies**, and engage the surface (if not already)

9. While engaged, press **Calibrate Lockin A Phase** and wait $\approx$ 30 seconds

10. (only FM-) Open up the **Main Cypher control panel**, and the **Tune** tab

11. (only FM-) Check the **Dual AC Mode** box

12. (only FM-) Press **Calibrate 2f phase** and wait $\approx$ 30 seconds

13. (for lift mode) Uncheck **Tuning/nolift**

14. (for lift mode) Open **Nap Mode**

15. (for lift mode) Press **Set H/FM-KPFM crosspoint** again

16. (for closed loop) Press **Set Voltage Loop** and **Start Voltage Loop**

17. Start a scan, and adjust the **I Gain** and **P Gain** for a clear KPFM signal

During this procedure, the **Show prelims** can be pressed to display the details of the tuning operations[4]

The Cypher has three channels that the user can set to collect data through the **Hack** panel: ***UserIn0***, ***UserIn1***, and ***UserIn2***. Here, ***UserIn1*** is the measured V_{K}, ***UserIn2*** is the signal the feedback loop acts on, and ***UserIn0*** is the quadrature signal. If the KPFM loop is working properly, the contrast should be entirely in the ***UserIn1*** channel, while ***UserIn0*** and ***UserIn2*** are mostly noise. In addition, in FM-KPFM, the $2f$ signal (proportional to V_{AC}^2) is also recorded, in the ***Amplitude2*** channel, but must be normalized by dividing by the internal optical lever sensitivity value[5]. The Open Loop estimate of V_{K} is calculated by dividing ***UserIn2*** by ***Amplitude2*** with an appropriate normalization constant. Beware, however, that in Open Loop thermal noise can often be quite large compared to

[4]Yes, it is the same *prelims* as before. This panel is actually calling the code underlying the parameter sweep panel to do the tuning!

[5]This is one of the quirks of data collection on the Cypher.

typical KPFM. However, even in closed loop operation, the $2f$ signal can be useful to look for sample heterogeneity or topographic coupling.

The Cypher's LockinA is used for the KPFM measurement, because it contains a notch filter that blocks (some of) the signal originating from the topographical feedback, and LockinB is used to control the topography. The tuning procedure that sets the phase between these LIAs is discussed in more detail in chapter 2.

A.2 Casimir force measurement panel

As described in the text above, the Casimir force measurement is performed at a series of separate heights, in several steps at each height. This appendix will provide a brief overview of the code, and some of the different types of measurements it can run. Casimir force measurements are run from the **Approach_panel**.

A particular force measurement is organized using the *The_Schema*, which is a series of measurements to be performed in order. For example, for the sphere-sphere measurements Setup_for_scan() is called first in order to align the upper sphere with the lower sphere, then meas_schema_setup() is called to run one approach/retract cycle and finally cal_schema_setup() is called to run a calibration approach/retract cycle. Each of functions ending in _schema_setup() starts by calling the KPFM code (discussed above) to set the reference phases for the electrostatic force. Then the measurement cycle begins:

1. Set height

   FM_advanceauto_P() starts the whole measurement sequence.

prepscan() starts the individual measurements.

2. Setup data collection

   Setup_am_meas2() sets up the data collection.

3. Collect data

   The data are collected by the Cypher.

4. Record data

   A callback is used to initiate the function gen_datasave().

5. Repeat

   The setup/collect/record sequence is repeated twice at each height for typical operation, and seven times if *extradata* is used.

6. Estimate sphere-plate separation and move

   If the closest approach (or furthest retraction) is reached, the movement changes direction.

The different channels are controlled automatically through the use of several multiplexer-style waves that connect signal input and signal output.

Bibliography

[1] H. Casimir, "On the attraction between two perfectly conducting plates," *Proc. K. Ned. Akad.* **360**: 793 (1948).

[2] V. A. Parsegian, *Van der Waals Forces*, Cambridge University Press, Cambridge (2006).

[3] B. V. Deryagin, "P. N. Lebedev's ideas on the nature of molecular forces," *Sov. Phys. Uspekhi* **10**, 1: 108 (1967).

[4] H. Hamaker, "The London-van der Waals attraction between spherical particles," *Physica* **4**, 10: 1058 (1937).

[5] H. B. G. Casimir and D. Polder, "The Influence of Retardation on the London-van der Waals Forces," *Phys. Rev.* **73**, 4: 360 (1948).

[6] E. Lifshitz, "The theory of molecular attractive forces between solids," *Sov. Phys.* **2**, 1: 73 (1956).

[7] I. E. Dzyaloshinskii, E. M. Lifshitz, and L. P. Pitaevskii, "General theory of van der Waals' forces," *Sov. Phys. Uspekhi* **4**, 2: 153 (1961).

[8] P. H. G. M. van Blokland and J. T. G. Overbeek, "van der Waals forces between objects covered with a chromium layer," *J. Chem. Soc. Faraday Trans. 1 Phys. Chem. Condens. Phases* **74**: 2637 (1978).

[9] S. Lamoreaux, "Demonstration of the Casimir Force in the 0. 6 to 6 μm Range," *Phys. Rev. Lett.* **78**, 1: 5 (1997).

[10] J. N. Munday, F. Capasso, and V. A. Parsegian, "Measured long-range repulsive Casimir-Lifshitz forces." *Nature* **457**, 7226: 170 (2009).

[11] S. de Man, K. Heeck, R. Wijngaarden, and D. Iannuzzi, "Halving the Casimir force with Conductive Oxides," *Phys. Rev. Lett.* **103**, 4: 040402 (2009).

[12] L. M. Woods, D. A. R. Dalvit, A. Tkatchenko, P. Rodriguez-Lopez, A. W. Rodriguez, and R. Podgornik, "Materials perspective on Casimir and van der Waals interactions," *Rev. Mod. Phys.* **88**, 4: 045003 (2016).

[13] J. Zou, Z. Marcet, A. W. Rodriguez, M. T. H. Reid, A. P. McCauley, I. I. Kravchenko, T. Lu, Y. Bao, S. G. Johnson, and H. B. Chan, "Casimir forces on a silicon micromechanical chip." *Nat. Commun.* **4**, May: 1845 (2013).

[14] L. Tang, M. Wang, C. Y. Ng, M. Nikolic, C. T. Chan, A. W. Rodriguez, and H. B. Chan, "Measurement of non-monotonic Casimir forces between silicon nanostructures," *Nat. Photonics* **11**, 2: 97 (2017).

[15] R. O. Behunin, F. Intravaia, D. A. R. Dalvit, P. A. Maia Neto, and S. Reynaud, "Modeling electrostatic patch effects in Casimir force measurements," *Phys. Rev. A* **85**, 1: 012504 (2012).

[16] N. D. Lang and W. Kohn, "Theory of Metal Surfaces: Work Function," *Phys. Rev. B* **3**, 4: 1215 (1971).

[17] A. Kahn, "Fermi level, work function and vacuum level," *Mater. Horiz.* **3**, 1: 7 (2016).

[18] M. Sparnaay, "Measurements of attractive forces between flat plates," *Physica* **24**, 3: 751 (1958).

[19] C. C. Speake and C. Trenkel, "Forces between Conducting Surfaces due to Spatial Variations of Surface Potential," *Phys. Rev. Lett.* **90**, 16: 160403 (2003).

[20] J. N. Munday and F. Capasso, "Precision measurement of the Casimir-Lifshitz force in a fluid," *Phys. Rev. A* **75**, 6: 060102 (2007).

[21] S. de Man, K. Heeck, and D. Iannuzzi, "Halving the Casimir force with conductive oxides: Experimental details," *Phys. Rev. A* **82**, 6: 062512 (2010).

[22] M. Bostrom and B. Sernelius, "Thermal effects on the Casimir force in the 0.1- 5 μm range," *Phys. Rev. Lett.* **84**, 20: 4757 (2000).

[23] A. Lambrecht, P. A. Maia Neto, and S. Reynaud, "The Casimir effect within scattering theory," *New J. Phys.* **8**, 10: 243 (2006).

[24] H. Gies and K. Klingmüller, "Worldline algorithms for Casimir configurations," *Phys. Rev. D* **74**, 4: 045002 (2006).

[25] A. Rodriguez, M. Ibanescu, D. Iannuzzi, F. Capasso, J. D. Joannopoulos, and S. G. Johnson, "Computation and Visualization of Casimir Forces in Arbitrary Geometries: Nonmonotonic Lateral-Wall Forces and the Failure of Proximity-Force Approximations," *Phys. Rev. Lett.* **99**, 8: 080401 (2007).

[26] O. Kenneth and I. Klich, "Casimir forces in a T-operator approach," *Phys. Rev. B* **78**, 1: 014103 (2008).

[27] M. Hartmann, G.-L. Ingold, and P. A. M. Neto, "Plasma versus Drude Modeling of the Casimir Force: Beyond the Proximity Force Approximation," *Phys. Rev. Lett.* **119**, 4: 043901 (2017).

[28] B. Derjaguin, "Untersuchungen uber die Reibung und Adhasion, IV," *Kolloid-Zeitschrift* **69**, 2: 155 (1934).

[29] I. Pirozhenko, A. Lambrecht, and V. B. Svetovoy, "Sample dependence of the Casimir force," *New J. Phys.* **8**, 10: 238 (2006).

[30] V. B. Svetovoy, P. J. van Zwol, G. Palasantzas, and J. T. M. De Hosson, "Optical properties of gold films and the Casimir force," *Phys. Rev. B* **77**, 3: 035439 (2008).

[31] L. P. Pitaevskii, "Pitaevskii Replies:," *Phys. Rev. Lett.* **102**, 18: 189302 (2009).

[32] D. A. R. Dalvit and S. K. Lamoreaux, "Dalvit and Lamoreaux Reply:," *Phys. Rev. Lett.* **102**, 18: 189304 (2009).

[33] S. K. Lamoreaux, "Progress in Experimental Measurements of the Surface-Surface Casimir Force: Electrostatic Calibrations and Limitations to Accuracy," in "Casimir Phys.", pp. 219–248 (2011).

[34] G. Binnig, C. Quate, and C. Gerber, "Atomic force microscope," *Phys. Rev. Lett.* **56**, 9 (1986).

[35] H.-J. Butt, B. Cappella, and M. Kappl, "Force measurements with the atomic force microscope: Technique, interpretation and applications," *Surf. Sci. Rep.* **59**, 1-6: 1 (2005).

[36] U. Mohideen and A. Roy, "Precision measurement of the Casimir force from 0.1 to 0.9 μm," *Phys. Rev. Lett.* **81**, 21: 4549 (1998).

[37] P. J. van Zwol, G. Palasantzas, and J. T. M. De Hosson, "Influence of random roughness on the Casimir force at small separations," *Phys. Rev. B* **77**, 7: 075412 (2008).

[38] H. B. Chan, V. A. Aksyuk, R. N. Kleiman, D. J. Bishop, and F. Capasso, "Quantum mechanical actuation of microelectromechanical systems by the Casimir force." *Science* **291**, 5510: 1941 (2001).

[39] R. Decca, D. López, E. Fischbach, G. Klimchitskaya, D. Krause, and V. Mostepanenko, "Precise comparison of theory and new experiment for the Casimir force leads to stronger constraints on thermal quantum effects and long-range interactions," *Ann. Phys.* **318**, 1: 37 (2005).

[40] H. B. Chan, V. A. Aksyuk, R. N. Kleiman, D. Bishop, and F. Capasso, "Nonlinear Micromechanical Casimir Oscillator," *Phys. Rev. Lett.* **87**, 21: 211801 (2001).

[41] R. S. Decca, D. López, E. Fischbach, and D. E. Krause, "Measurement of the Casimir Force between Dissimilar Metals," *Phys. Rev. Lett.* **91**, 5: 050402 (2003).

[42] F. Chen, U. Mohideen, G. Klimchitskaya, and V. Mostepanenko, "Investigation of the Casimir force between metal and semiconductor test bodies," *Phys. Rev. A* **72**, 2: 020101 (2005).

[43] W. J. Kim, A. O. Sushkov, D. A. R. Dalvit, and S. K. Lamoreaux, "Measurement of the Short-Range Attractive Force between Ge Plates Using a Torsion Balance," *Phys. Rev. Lett.* **103**, 6: 060401 (2009).

[44] G. Torricelli, I. Pirozhenko, S. Thornton, A. Lambrecht, and C. Binns, "Casimir force between a metal and a semimetal," *EPL* **93**, 5: 51001 (2011).

[45] A. Banishev, H. Wen, and J. Xu, "Measuring the Casimir force gradient from graphene on a SiO_2 substrate," *Phys. Rev. B* **205433**: 1 (2013).

[46] M. Sedighi, V. B. Svetovoy, and G. Palasantzas, "Casimir force measurements from silicon carbide surfaces," *Phys. Rev. B* **93**, 8: 085434 (2016).

[47] P. van Zwol, G. Palasantzas, and J. De Hosson, "Influence of roughness on capillary forces between hydrophilic surfaces," *Phys. Rev. E* **78**, 3: 031606 (2008).

[48] G. Palasantzas, V. Svetovoy, and P. van Zwol, "Influence of ultrathin water layer on the van der Waals/Casimir force between gold surfaces," *Phys. Rev. B* **79**, 23: 235434 (2009).

[49] F. Chen, G. L. Klimchitskaya, V. M. Mostepanenko, and U. Mohideen, "Control of the Casimir force by the modification of dielectric properties with light," *Phys. Rev. B* **76**, 3: 035338 (2007).

[50] G. Torricelli, P. van Zwol, O. Shpak, C. Binns, G. Palasantzas, B. Kooi, V. Svetovoy, and M. Wuttig, "Switching Casimir forces with phase-change materials," *Phys. Rev. A* **82**, 1: 010101 (2010).

[51] H. B. Chan, Y. Bao, J. Zou, R. Cirelli, F. Klemens, W. M. Mansfield, and C. S. Pai, "Measurement of the Casimir Force between a Gold Sphere and a Silicon Surface with Nanoscale Trench Arrays," *Phys. Rev. Lett.* **101**, 3: 030401 (2008).

[52] F. Intravaia, S. Koev, I. W. Jung, A. A. Talin, P. S. Davids, R. S. Decca, V. A. Aksyuk, D. A. R. Dalvit, and D. López, "Strong Casimir force reduction through metallic surface nanostructuring." *Nat. Commun.* **4**: 2515 (2013).

[53] M. Levin, A. P. McCauley, A. W. Rodriguez, M. T. H. Reid, and S. G. Johnson, "Casimir Repulsion between Metallic Objects in Vacuum," *Phys. Rev. Lett.* **105**, 9: 090403 (2010).

[54] I. Cavero-Peláez, K. A. Milton, P. Parashar, and K. V. Shajesh, "Noncontact gears. II. Casimir torque between concentric corrugated cylinders for the scalar case," *Phys. Rev. D* **78**, 6: 065019 (2008).

[55] D. A. T. Somers and J. N. Munday, "Conditions for repulsive Casimir forces between identical birefringent materials," *Phys. Rev. A* **95**, 2: 022509 (2017).

[56] Y. S. Barash, "Moment of van der Waals forces between anisotropic bodies," *Radiophys. Quantum Electron.* **21**, 11: 1138 (1978).

[57] J. N. Munday, D. Iannuzzi, Y. Barash, and F. Capasso, "Torque on birefringent plates induced by quantum fluctuations," *Phys. Rev. A* **71**, 4: 042102 (2005).

[58] D. A. T. Somers and J. N. Munday, "Rotation of a liquid crystal by the Casimir torque," *Phys. Rev. A* **91**, 3: 032520 (2015).

[59] R. Guérout, C. Genet, A. Lambrecht, and S. Reynaud, "Casimir torque between nanostructured plates," *EPL* **111**, 4: 44001 (2015).

[60] G. Binnig, C. Gerber, E. Stoll, T. R. Albrecht, and C. F. Quate, "Atomic Resolution with Atomic Force Microscope," *Europhys. Lett.* **3**, 12: 1281 (1987).

[61] G. Binnig, "Force microscopy," *Ultramicroscopy* **42-44**: 7 (1992).

[62] F. Giessibl, "Atomic resolution of the silicon (111)-(7x7) surface by atomic force microscopy," *Science* **267**, 5194: 68 (1995).

[63] F. Giessibl, "Forces and frequency shifts in atomic-resolution dynamic-force microscopy," *Phys. Rev. B* **56**, 24: 16010 (1997).

[64] F. J. Giessibl, "Advances in atomic force microscopy," *Rev. Mod. Phys.* **75**, 3: 949 (2003).

[65] J. L. Garrett and J. N. Munday, "Fast, high-resolution surface potential measurements in air with heterodyne Kelvin probe force microscopy." *Nanotechnology* **27**, 24: 245705 (2016).

[66] M. Nonnenmacher, M. P. O'Boyle, and H. K. Wickramasinghe, "Kelvin probe force microscopy," *Appl. Phys. Lett.* **58**, 25: 2921 (1991).

[67] M. Nonnenmacher, M. P. O'Boyle, and H. K. Wickramasinghe, "Surface investigations with a Kelvin probe force microscope," *Ultramicroscopy* **44**: 268 (1992).

[68] J. M. R. Weaver and D. W. Abraham, "High resolution atomic force microscopy potentiometry," *J. Vac. Sci. Technol. B* **9**, 3: 1559 (1991).

[69] A. K. Henning, T. Hochwitz, J. Slinkman, J. Never, S. Hoffmann, P. Kaszuba, and C. Daghlian, "Two-dimensional surface dopant profiling in silicon using scanning Kelvin probe microscopy," *J. Appl. Phys.* **77**, 5: 1888 (1995).

[70] A. Kikukawa, S. Hosaka, and R. Imura, "Silicon pn junction imaging and characterizations using sensitivity enhanced Kelvin probe force microscopy," *Appl. Phys. Lett.* **66**, 25: 3510 (1995).

[71] J. Lü, E. Delamarche, L. Eng, R. Bennewitz, E. Meyer, and H.-J. Güntherodt, "Kelvin Probe Force Microscopy on Surfaces: Investigation of the Surface Potential of Self-Assembled Monolayers on Gold," *Langmuir* **15**, 23: 8184 (1999).

[72] N. Reitzel, T. Hassenkam, K. Balashev, T. R. Jensen, P. B. Howes, K. Kjaer, A. Fechtenkötter, N. Tchebotareva, S. Ito, K. Müllen, and T. Bjørnholm, "Langmuir and Langmuir-Blodgett Films of Amphiphilic Hexa-perihexabenzocoronene: New Phase Transitions and Electronic Properties Controlled by Pressure," *Chem. Eur. J.* **7**, 22: 4894 (2001).

[73] N. Gaillard, M. Gros-Jean, D. Mariolle, F. Bertin, and A. Bsiesy, "Method to assess the grain crystallographic orientation with a submicronic spatial resolution using Kelvin probe force microscope," *Appl. Phys. Lett.* **89**, 15: 154101 (2006).

[74] A. K. Sinensky and A. M. Belcher, "Label-free and high-resolution protein/DNA nanoarray analysis using Kelvin probe force microscopy," *Nat. Nanotechnol.* **2**, 10: 653 (2007).

[75] H. O. Jacobs, H. F. Knapp, S. Müller, and A. Stemmer, "Surface potential mapping: A qualitative material contrast in SPM," *Ultramicroscopy* **69**, 1: 39 (1997).

[76] I. Lee, J. W. Lee, A. Stubna, and E. Greenbaum, "Measurement of Electrostatic Potentials above Oriented Single Photosynthetic Reaction Centers," *J. Phys. Chem. B* **104**, 11: 2439 (2000).

[77] V. Palermo, M. Palma, and P. Samorì, "Electronic Characterization of Organic Thin Films by Kelvin Probe Force Microscopy," *Adv. Mater.* **18**, 2: 145 (2006).

[78] J. Colchero, A. Gil, and A. M. Baró, "Resolution enhancement and improved data interpretation in electrostatic force microscopy," *Phys. Rev. B* **64**, 24: 245403 (2001).

[79] G. Koley, M. G. Spencer, and H. R. Bhangale, "Cantilever effects on the measurement of electrostatic potentials by scanning Kelvin probe microscopy," *Appl. Phys. Lett.* **79**, 4: 545 (2001).

[80] Z. M. Ma, L. Kou, Y. Naitoh, Y. J. Li, and Y. Sugawara, "The stray capacitance effect in Kelvin probe force microscopy using FM, AM and heterodyne AM modes." *Nanotechnology* **24**, 22: 225701 (2013).

[81] H. Diesinger, D. Deresmes, J.-P. Nys, and T. Mélin, "Kelvin force microscopy at the second cantilever resonance: An out-of-vacuum crosstalk compensation setup," *Ultramicroscopy* **108**, 8: 773 (2008).

[82] T. Mélin, S. Barbet, H. Diesinger, D. Théron, and D. Deresmes, "Note: Quantitative (artifact-free) surface potential measurements using Kelvin force microscopy," *Rev. Sci. Instrum.* **82**, 3: 036101 (2011).

[83] L. Polak, S. de Man, and R. J. Wijngaarden, "Note: switching crosstalk on and off in Kelvin Probe Force Microscopy." *Rev. Sci. Instrum.* **85**, 4: 046111 (2014).

[84] S. Barbet, M. Popoff, H. Diesinger, D. Deresmes, D. Théron, and T. Mélin, "Cross-talk artefacts in Kelvin probe force microscopy imaging: A comprehensive study," *J. Appl. Phys.* **115**, 14: 144313 (2014).

[85] S. Kitamura and M. Iwatsuki, "High-resolution imaging of contact potential difference with ultrahigh vacuum noncontact atomic force microscope," *Appl. Phys. Lett.* **72**, 24: 3154 (1998).

[86] T. Glatzel, S. Sadewasser, and M. Lux-Steiner, "Amplitude or frequency modulation-detection in Kelvin probe force microscopy," *Appl. Surf. Sci.* **210**, 1-2: 84 (2003).

[87] U. Zerweck, C. Loppacher, T. Otto, S. Grafström, and L. M. Eng, "Accuracy and resolution limits of Kelvin probe force microscopy," *Phys. Rev. B* **71**, 12: 125424 (2005).

[88] V. Panchal, R. Pearce, R. Yakimova, A. Tzalenchuk, and O. Kazakova, "Standardization of surface potential measurements of graphene domains," *Sci. Rep.* **3**, 2: 2597 (2013).

[89] C. Sommerhalter, T. W. Matthes, T. Glatzel, A. Jäger-Waldau, and M. C. Lux-Steiner, "High-sensitivity quantitative Kelvin probe microscopy by noncontact ultra-high-vacuum atomic force microscopy," *Appl. Phys. Lett.* **75**, 2: 286 (1999).

[90] S. Sadewasser, T. Glatzel, M. Rusu, A. Jäger-Waldau, and M. C. Lux-Steiner, "High-resolution work function imaging of single grains of semiconductor surfaces," *Appl. Phys. Lett.* **80**, 16: 2979 (2002).

[91] Z. Leonenko, S. Gill, S. Baoukina, L. Monticelli, J. Doehner, L. Gunasekara, F. Felderer, M. Rodenstein, L. M. Eng, and M. Amrein, "An Elevated Level of Cholesterol Impairs Self-Assembly of Pulmonary Surfactant into a Functional Film," *Biophys. J.* **93**, 2: 674 (2007).

[92] S. Sadewasser, T. Glatzel, S. Schuler, S. Nishiwaki, R. Kaigawa, and M. Lux-Steiner, "Kelvin probe force microscopy for the nano scale characterization of chalcopyrite solar cell materials and devices," *Thin Solid Films* **431-432**, 03: 257 (2003).

[93] Y. Zhang, Q. Chen, A. P. Alivisatos, and M. Salmeron, "Dynamic Charge Carrier Trapping in Quantum Dot Field Effect Transistors," *Nano Lett.* **15**, 7: 4657 (2015).

[94] F. Mohn, L. Gross, N. Moll, and G. Meyer, "Imaging the charge distribution within a single molecule," *Nat. Nanotechnol.* **7**, 4: 227 (2012).

[95] L. Gross, F. Mohn, P. Liljeroth, J. Repp, F. J. Giessibl, and G. Meyer, "Measuring the Charge State of an Adatom with Noncontact Atomic Force Microscopy," *Science* **324**, 5933: 1428 (2009).

[96] D. C. Coffey and D. S. Ginger, "Time-resolved electrostatic force microscopy of polymer solar cells." *Nat. Mater.* **5**, 9: 735 (2006).

[97] J. Murawski, T. Graupner, P. Milde, R. Raupach, U. Zerweck-Trogisch, and L. M. Eng, "Pump-probe Kelvin-probe force microscopy: Principle of operation and resolution limits," *J. Appl. Phys.* **118**, 15: 154302 (2015).

[98] O. Takeuchi, Y. Ohrai, S. Yoshida, and H. Shigekawa, "Kelvin Probe Force Microscopy without Bias-Voltage Feedback," *Jpn. J. Appl. Phys.* **46**, 8B: 5626 (2007).

[99] L. Collins, J. I. Kilpatrick, S. A. L. Weber, A. Tselev, I. V. Vlassiouk, I. N. Ivanov, S. Jesse, S. V. Kalinin, and B. J. Rodriguez, "Open loop Kelvin probe force microscopy with single and multi-frequency excitation," *Nanotechnology* **24**, 47: 475702 (2013).

[100] R. Borgani, D. Forchheimer, J. Bergqvist, P.-A. Thorén, O. Inganäs, and D. B. Haviland, "Intermodulation electrostatic force microscopy for imaging surface photo-voltage," *Appl. Phys. Lett.* **105**, 14: 143113 (2014).

[101] B. Moores, F. Hane, L. Eng, and Z. Leonenko, "Kelvin probe force microscopy in application to biomolecular films: Frequency modulation, amplitude modulation, and lift mode," *Ultramicroscopy* **110**, 6: 708 (2010).

[102] E. M. Tennyson, J. L. Garrett, J. A. Frantz, J. D. Myers, R. Y. Bekele, J. S. Sanghera, J. N. Munday, and M. S. Leite, "Nanoimaging of Open-Circuit Voltage in Photovoltaic Devices," *Adv. Energy Mater.* **5**, 23 (2015).

[103] E. Sengupta, A. L. Domanski, S. A. L. Weber, M. B. Untch, H.-J. Butt, T. Sauermann, H. J. Egelhaaf, and R. Berger, "Photoinduced Degradation Studies of Organic Solar Cell Materials Using Kelvin Probe Force and Conductive Scanning Force Microscopy," *J. Phys. Chem. C* **115**, 40: 19994 (2011).

[104] Y. Sugawara, L. Kou, Z. Ma, T. Kamijo, Y. Naitoh, and Y. Jun Li, "High potential sensitivity in heterodyne amplitude-modulation Kelvin probe force microscopy," *Appl. Phys. Lett.* **100**, 22: 223104 (2012).

[105] D. S. Wastl, A. J. Weymouth, and F. J. Giessibl, "Optimizing atomic resolution of force microscopy in ambient conditions," *Phys. Rev. B* **87**, 24: 245415 (2013).

[106] Z.-M. Ma, J.-L. Mu, J. Tang, H. Xue, H. Zhang, C.-Y. Xue, J. Liu, and Y.-J. Li, "Potential sensitivities in frequency modulation and heterodyne amplitude modulation Kelvin probe force microscopes," *Nanoscale Res. Lett.* **8**, 1: 532 (2013).

[107] S. Hudlet, M. Saint Jean, B. Roulet, J. Berger, and C. Guthmann, "Electrostatic forces between metallic tip and semiconductor surfaces," *J. Appl. Phys.* **77**, 7: 3308 (1995).

[108] J. L. Garrett, L. J. Krayer, K. J. Palm, and J. N. Munday, "Effect of lateral tip motion on multifrequency atomic force microscopy," *Appl. Phys. Lett.* **111**, 4: 043105 (2017).

[109] J. L. Garrett, D. A. T. Somers, and J. N. Munday, "The effect of patch potentials in Casimir force measurements determined by heterodyne Kelvin probe force microscopy," *J. Phys. Condens. Matter* **27**, 21: 214012 (2015).

[110] R. García and A. San Paulo, "Attractive and repulsive tip-sample interaction regimes in tapping-mode atomic force microscopy," *Phys. Rev. B* **60**, 7: 4961 (1999).

[111] K. S. Novoselov, A. K. Geim, S. V. Morozov, D. Jiang, Y. Zhang, S. V. Dubonos, I. V. Grigorieva, and A. A. Firsov, "Electric field effect in atomically thin carbon films." *Science* **306**, 5696: 666 (2004).

[112] S. V. Kalinin and D. A. Bonnell, "Surface potential at surface-interface junctions in $SrTiO_3$ bicrystals," *Phys. Rev. B* **62**, 15: 419 (2000).

[113] H. Diesinger, D. Deresmes, J.-P. Nys, and T. Mélin, "Dynamic behavior of amplitude detection Kelvin force microscopy in ultrahigh vacuum," *Ultramicroscopy* **110**, 2: 162 (2010).

[114] H. Diesinger, D. Deresmes, and T. Mélin, "Noise performance of frequency modulation Kelvin force microscopy," *Beilstein J. Nanotechnol.* **5**: 1 (2014).

[115] T. Wagner, H. Beyer, P. Reissner, P. Mensch, H. Riel, B. Gotsmann, and A. Stemmer, "Kelvin probe force microscopy for local characterisation of active nanoelectronic devices," *Beilstein J. Nanotechnol.* **6**, 1: 2193 (2015).

[116] J. Bechhoefer, "Feedback for physicists: A tutorial essay on control," *Rev. Mod. Phys.* **77**, July: 783 (2005).

[117] E. J. Spadafora, M. Linares, W. Z. Nisa Yahya, F. Lincker, R. Demadrille, and B. Grevin, "Local contact potential difference of molecular self-assemblies investigated by Kelvin probe force microscopy," *Appl. Phys. Lett.* **99**, 23: 233102 (2011).

[118] A. Labuda, J. R. Bates, and P. H. Grütter, "The noise of coated cantilevers," *Nanotechnology* **23**, 2: 025503 (2012).

[119] C. V. Heer, *Statistical Mechanics, Kinetic Theory, and Stochastic Processes*, Academic Press, Inc., New York (1972).

[120] J. Melcher, S. Hu, and A. Raman, "Equivalent point-mass models of continuous atomic force microscope probes," *Appl. Phys. Lett.* **91**, 5: 053101 (2007).

[121] H.-J. Butt and M. Jaschke, "Calculation of thermal noise in atomic force microscopy," *Nanotechnology* **6**, 1: 1 (1995).

[122] H. O. Jacobs, P. Leuchtmann, O. J. Homan, and A. Stemmer, "Resolution and contrast in Kelvin probe force microscopy," *J. Appl. Phys.* **84**, 3: 1168 (1998).

[123] H. N. McMurray and G. Williams, "Probe diameter and probe-specimen distance dependence in the lateral resolution of a scanning Kelvin probe," *J. Appl. Phys.* **91**, 3: 1673 (2002).

[124] A. Liscio, V. Palermo, D. Gentilini, F. Nolde, K. Müllen, and P. Samorì, "Quantitative Measurement of the Local Surface Potential of π-Conjugated Nanostructures: A Kelvin Probe Force Microscopy Study," *Adv. Funct. Mater.* **16**, 11: 1407 (2006).

[125] R. C. Gonzalez, R. E. Woods, and S. L. Eddins, *Digital Image Processing Using MATLAB*, vol. 1, Pearson (2004).

[126] W. J. Kim, A. O. Sushkov, D. A. R. Dalvit, and S. K. Lamoreaux, "Surface contact potential patches and Casimir force measurements," *Phys. Rev. A* **81**, 2: 022505 (2010).

[127] S. Hudlet, M. Saint Jean, C. Guthmann, and J. Berger, "Evaluation of the capacitive force between an atomic force microscopy tip and a metallic surface," *Eur. Phys. J. B* **2**, 1: 5 (1998).

[128] R. O. Behunin, Y. Zeng, D. A. R. Dalvit, and S. Reynaud, "Electrostatic patch effects in Casimir-force experiments performed in the sphere-plane geometry," *Phys. Rev. A* **86**, 5: 052509 (2012).

[129] A. Ahmad, A. Schuh, and I. W. Rangelow, "Adaptive AFM scan speed control for high aspect ratio fast structure tracking," *Rev. Sci. Instrum.* **85**, 10: 103706 (2014).

[130] S. Sadewasser, G. Villanueva, and J. A. Plaza, "Special cantilever geometry for the access of higher oscillation modes in atomic force microscopy," *Appl. Phys. Lett.* **89**, 3: 033106 (2006).

[131] M. S. Marcus, R. W. Carpick, D. Y. Sasaki, and M. A. Eriksson, "Material anisotropy revealed by phase contrast in intermittent contact atomic force microscopy," *Phys. Rev. Lett.* **88**, 22: 226103 (2002).

[132] M. J. D'Amato, M. S. Marcus, M. A. Eriksson, and R. W. Carpick, "Phase imaging and the lever-sample tilt angle in dynamic atomic force microscopy," *Appl. Phys. Lett.* **85**, 20: 4738 (2004).

[133] L.-O. Heim, M. Kappl, and H.-J. Butt, "Tilt of atomic force microscope cantilevers: effect on spring constant and adhesion measurements," *Langmuir* **20**, 7: 2760 (2004).

[134] J. L. Hutter, "Comment on tilt of atomic force microscope cantilevers: effect on spring constant and adhesion measurements." *Langmuir* **21**, 6: 2630 (2005).

[135] S. Kawai, T. Glatzel, S. Koch, B. Such, A. Baratoff, and E. Meyer, "Ultrasensitive detection of lateral atomic-scale interactions on graphite (0001) via bimodal dynamic force measurements," *Phys. Rev. B* **81**, 8: 085420 (2010).

[136] K. P. Sigdel, J. S. Grayer, and G. M. King, "Three-Dimensional Atomic Force Microscopy: Interaction Force Vector by Direct Observation of Tip Trajectory," *Nano Lett.* **13**, 11: 5106 (2013).

[137] C. F. Reiche, S. Vock, V. Neu, L. Schultz, B. Büchner, and T. Mühl, "Bidirectional quantitative force gradient microscopy," *New J. Phys.* **17**, 1: 013014 (2015).

[138] T. Meier, B. Eslami, and S. D. Solares, "Multifrequency force microscopy using flexural and torsional modes by photothermal excitation in liquid: atomic resolution imaging of calcite (1014)," *Nanotechnology* **27**, 8: 085702 (2016).

[139] F. Huang, V. A. Tamma, M. Rajaei, M. Almajhadi, and H. K. Wickramasinghe, "Measurement of laterally induced optical forces at the nanoscale," *Appl. Phys. Lett.* **110**, 6: 063103 (2017).

[140] Y. Naitoh, R. Turanský, J. Brndiar, Y. J. Li, I. Štich, and Y. Sugawara, "Subatomic-scale force vector mapping above a Ge(001) dimer using bimodal atomic force microscopy," *Nat. Phys.* **13**, 7: 663 (2017).

[141] S. Jesse, S. V. Kalinin, R. Proksch, A. P. Baddorf, and B. J. Rodriguez, "The band excitation method in scanning probe microscopy for rapid mapping of energy dissipation on the nanoscale," *Nanotechnology* **18**, 43: 435503 (2007).

[142] D. Platz, E. A. Tholén, D. Pesen, and D. B. Haviland, "Intermodulation atomic force microscopy," *Appl. Phys. Lett.* **92**, 15: 153106 (2008).

[143] L. Tetard, A. Passian, and T. Thundat, "New modes for subsurface atomic force microscopy through nanomechanical coupling." *Nat. Nanotechnol.* **5**, 2: 105 (2010).

[144] R. Garcia and E. T. Herruzo, "The emergence of multifrequency force microscopy." *Nat. Nanotechnol.* **7**, 4: 217 (2012).

[145] D. Ebeling, B. Eslami, and S. D. J. Solares, "Visualizing the Subsurface of Soft Matter: Simultaneous Topographical Imaging, Depth Modulation, and Compositional Mapping with Triple Frequency Atomic Force Microscopy," *ACS Nano* **7**, 11: 10387 (2013).

[146] I. Rajapaksa and H. K. Wickramasinghe, "Raman spectroscopy and microscopy based on mechanical force detection," *Appl. Phys. Lett.* **99**, 16: 161103 (2011).

[147] E. Arima, Y. Naitoh, Y. Jun Li, S. Yoshimura, H. Saito, H. Nomura, R. Nakatani, and Y. Sugawara, "Magnetic force microscopy using tip magnetization modulated by ferromagnetic resonance," *Nanotechnology* **26**, 12: 125701 (2015).

[148] T. U. Tumkur, X. Yang, B. Cerjan, N. J. Halas, P. Nordlander, and I. Thomann, "Photoinduced Force Mapping of Plasmonic Nanostructures," *Nano Lett.* **16**, 12: 7942 (2016).

[149] J. Jahng, B. Kim, E. S. Lee, and E. O. Potma, "Quantitative analysis of sideband coupling in photoinduced force microscopy," *Phys. Rev. B* **94**, 19: 195407 (2016).

[150] A. Ambrosio, R. C. Devlin, F. Capasso, and W. L. Wilson, "Observation of Nanoscale Refractive Index Contrast via Photoinduced Force Microscopy," *ACS Photonics* **4**, 4: 846 (2017).

[151] J. L. Garrett, E. M. Tennyson, M. Hu, J. Huang, J. N. Munday, and M. S. Leite, "Real-Time Nanoscale Open-Circuit Voltage Dynamics of Perovskite Solar Cells," *Nano Lett.* **17**, 4: 2554 (2017).

[152] G. Elias, T. Glatzel, E. Meyer, A. Schwarzman, A. Boag, and Y. Rosenwaks, "The role of the cantilever in Kelvin probe force microscopy measurements," *Beilstein J. Nanotechnol.* **2**, 1: 252 (2011).

[153] K. J. Satzinger, K. A. Brown, and R. M. Westervelt, "The importance of cantilever dynamics in the interpretation of Kelvin probe force microscopy," *J. Appl. Phys.* **112**, 6: 064510 (2012).

[154] J. Lozano and R. Garcia, "Theory of phase spectroscopy in bimodal atomic force microscopy," *Phys. Rev. B* **79**, 1: 014110 (2009).

[155] R. C. Tung, T. Wutscher, D. Martinez-Martin, R. G. Reifenberger, F. Giessibl, and A. Raman, "Higher-order eigenmodes of qPlus sensors for high resolution dynamic atomic force microscopy," *J. Appl. Phys.* **107**, 10: 104508 (2010).

[156] A. Labuda, M. Kocun, M. Lysy, T. Walsh, J. Meinhold, T. Proksch, W. Meinhold, C. Anderson, and R. Proksch, "Calibration of higher eigenmodes of cantilevers," *Rev. Sci. Instrum.* **87**, 7: 073705 (2016).

[157] Á. Paulo and R. García, "Unifying theory of tapping-mode atomic-force microscopy," *Phys. Rev. B* **66**, 4: 041406 (2002).

[158] L. Collins, S. Jesse, N. Balke, B. J. Rodriguez, S. Kalinin, and Q. Li, "Band excitation Kelvin probe force microscopy utilizing photothermal excitation," *Appl. Phys. Lett.* **106**, 10: 104102 (2015).

[159] D. A. Walters, J. P. Cleveland, N. H. Thomson, P. K. Hansma, M. A. Wendman, G. Gurley, and V. Elings, "Short cantilevers for atomic force microscopy," *Rev. Sci. Instrum.* **67**, 10: 3583 (1996).

[160] M. T. Sheldon, J. V. D. Groep, A. M. Brown, A. Polman, and H. A. Atwater, "Plasmoelectric potentials in metal nanostructures," *Science* **346**, 6211: 828 (2014).

[161] J. L. Hutter and J. Bechhoefer, "Manipulation of van der Waals forces to improve image resolution in atomic-force microscopy," *J. Appl. Phys.* **73**, 9: 4123 (1993).

[162] L. Gross, Z. L. Wang, D. Ugarte, F. Mohn, N. Moll, W. a. Heer, P. Vincent, P. Liljeroth, C. Journet, G. Meyer, V. T. Binh, M. Poot, H. S. J. V. D. Zant, A. Aguasca, A. Bachtold, K. Kim, A. Zettl, P. Hung, H. W. C. Postma, M. Bockrath, X. Blase, and S. Roche, "The Chemical structure of a molecule resolved by atomic force microscopy," *Science* **325**: 1110 (2009).

[163] L. Gross, B. Schuler, F. Mohn, N. Moll, N. Pavliček, W. Steurer, I. Scivetti, K. Kotsis, M. Persson, and G. Meyer, "Investigating atomic contrast in atomic force microscopy and Kelvin probe force microscopy on ionic systems using functionalized tips," *Phys. Rev. B* **90**, 15: 155455 (2014).

[164] C. Wagner, M. F. B. Green, P. Leinen, T. Deilmann, P. Krüger, M. Rohlfing, R. Temirov, and F. S. Tautz, "Scanning Quantum Dot Microscopy," *Phys. Rev. Lett.* **115**, 2: 026101 (2015).

[165] T. R. Albrecht, P. Grütter, D. Horne, and D. Rugar, "Frequency modulation detection using high-Q cantilevers for enhanced force microscope sensitivity," *J. Appl. Phys.* **69**, 2: 668 (1991).

[166] D. Dalvit and S. Lamoreaux, "Contribution of Drifting Carriers to the Casimir-Lifshitz and Casimir-Polder Interactions With Semiconductor Materials," *Phys. Rev. Lett.* **101**, 16: 163203 (2008).

[167] V. Svetovoy, "Application of the Lifshitz Theory to Poor Conductors," *Phys. Rev. Lett.* **101**, 16: 163603 (2008).

[168] A. A. Allocca, J. H. Wilson, and V. Galitski, "Nonanalytic behavior of the Casimir force across a Lifshitz transition in a spin-orbit-coupled material," *Phys. Rev. B* **90**, 7: 075420 (2014).

[169] C.-Y. Lai, V. Barcons, S. Santos, and M. Chiesa, "Periodicity in bimodal atomic force microscopy," *J. Appl. Phys.* **118**, 4: 044905 (2015).

[170] S. S. Borysov, D. Platz, A. S. de Wijn, D. Forchheimer, E. A. Tolén, A. V. Balatsky, and D. B. Haviland, "Reconstruction of tip-surface interactions with multimodal intermodulation atomic force microscopy," *Phys. Rev. B* **88**, 11: 115405 (2013).

[171] E. T. Herruzo, A. P. Perrino, and R. Garcia, "Fast nanomechanical spectroscopy of soft matter," *Nat. Commun.* **5** (2014).

[172] K. M. Burson, W. G. Cullen, S. Adam, C. R. Dean, K. Watanabe, T. Taniguchi, P. Kim, and M. S. Fuhrer, "Direct Imaging of Charged Impurity Density in Common Graphene Substrates," *Nano Lett.* **13**, 8: 3576 (2013).

[173] T. Ederth, "Template-stripped gold surfaces with 0.4-nm rms roughness suitable for force measurements: Application to the Casimir force in the 20-100 nm range," *Phys. Rev. A* **62**: 062104 (2000).

[174] J. Laurent, H. Sellier, A. Mosset, S. Huant, and J. Chevrier, "Casimir force measurements in Au-Au and Au-Si cavities at low temperature," *Phys. Rev. B* **85**, 3: 035426 (2012).

[175] F. Chen, G. Klimchitskaya, V. Mostepanenko, and U. Mohideen, "Demonstration of the Difference in the Casimir Force for Samples with Different Charge-Carrier Densities," *Phys. Rev. Lett.* **97**, 17: 170402 (2006).

[176] G. Bimonte, D. López, and R. S. Decca, "Isoelectronic determination of the thermal Casimir force," *Phys. Rev. B* **93**, 18: 184434 (2016).

[177] G. Bressi, G. Carugno, R. Onofrio, and G. Ruoso, "Measurement of the Casimir Force between Parallel Metallic Surfaces," *Phys. Rev. Lett.* **88**, 4: 041804 (2002).

[178] A. O. Sushkov, W. J. Kim, D. A. R. Dalvit, and S. K. Lamoreaux, "Observation of the thermal Casimir force," *Nat. Phys.* **7**, 3: 230 (2011).

[179] C.-C. Chang, A. A. Banishev, R. Castillo-Garza, G. L. Klimchitskaya, V. M. Mostepanenko, and U. Mohideen, "Gradient of the Casimir force between Au surfaces of a sphere and a plate measured using an atomic force microscope in a frequency-shift technique," *Phys. Rev. B* **85**, 16: 165443 (2012).

[180] F. Capasso, J. N. Munday, D. Iannuzzi, and H. B. Chan, "Casimir Forces and Quantum Electrodynamical Torques: Physics and Nanomechanics," *IEEE J. Sel. Top. Quantum Electron.* **13**, 2: 400 (2007).

[181] F. Serry, D. Walliser, and G. Maclay, "The anharmonic Casimir oscillator (ACO)-the Casimir effect in a model microelectromechanical system," *J. Microelectromechanical Syst.* **4**, 4: 193 (1995).

[182] W. Kim, M. Brown-Hayes, D. Dalvit, J. Brownell, and R. Onofrio, "Anomalies in electrostatic calibrations for the measurement of the Casimir force in a sphere-plane geometry," *Phys. Rev. A* **78**, 2: 020101 (2008).

[183] S. de Man, K. Heeck, and D. Iannuzzi, "No anomalous scaling in electrostatic calibrations for Casimir force measurements," *Phys. Rev. A* **79**, 2: 024102 (2009).

[184] S. K. Lamoreaux and D. Wong, "Mechanical temporal fluctuation induced distance and force systematic errors in Casimir force experiments," *J. Phys. Condens. Matter* **27**, 21: 214016 (2015).

[185] Q.-X. Huang, Y.-T. Fei, S. Gonda, I. Misumi, O. Sato, T. Keem, and T. Kurosawa, "The interference effect in an optical beam deflection detection system of a dynamic mode AFM," *Meas. Sci. Technol.* **17**, 6: 1417 (2006).

[186] G. Alphonse, D. Gilbert, M. Harvey, and M. Ettenberg, "High-power superluminescent diodes," *IEEE J. Quantum Electron.* **24**, 12: 2454 (1988).

[187] G. B. Kaggwa, J. I. Kilpatrick, J. E. Sader, and S. P. Jarvis, "Artifact-free dynamic atomic force microscopy reveals monotonic dissipation for a simple confined liquid," *Appl. Phys. Lett.* **93**, 1: 011909 (2008).

[188] R. Proksch and S. V. Kalinin, "Energy dissipation measurements in frequency-modulated scanning probe microscopy." *Nanotechnology* **21**, 45: 455705 (2010).

[189] A. Labuda, Y. Miyahara, L. Cockins, and P. H. Grütter, "Decoupling conservative and dissipative forces in frequency modulation atomic force microscopy," *Phys. Rev. B* **84**, 12: 125433 (2011).

[190] A. Labuda, K. Kobayashi, D. Kiracofe, K. Suzuki, P. H. Grutter, and H. Yamada, "Comparison of photothermal and piezoacoustic excitation methods for frequency and phase modulation atomic force microscopy in liquid environments," *AIP Adv.* **1**, 2: 022136 (2011).

[191] A. Maali and B. Bhushan, "Slip-length measurement of confined air flow using dynamic atomic force microscopy," *Phys. Rev. E* **78**, 2: 027302 (2008).

[192] J. N. Munday, F. Capasso, V. A. Parsegian, and S. M. Bezrukov, "Measurements of the Casimir-Lifshitz force in fluids: The effect of electrostatic forces and Debye screening," *Phys. Rev. A* **78**, 3: 032109 (2008).

[193] J. Laurent, A. Drezet, H. Sellier, J. Chevrier, and S. Huant, "Large Variation in the Boundary-Condition Slippage for a Rarefied Gas Flowing between Two Surfaces," *Phys. Rev. Lett.* **107**, 16: 164501 (2011).

[194] W. J. Kim, M. Brown-Hayes, D. a. R. Dalvit, J. H. Brownell, and R. Onofrio, "On electrostatic and Casimir force measurements between conducting surfaces in a sphere-plane configuration," *J. Phys. Conf. Ser.* **161**: 012004 (2009).

[195] S. K. Lamoreaux, "The Casimir Force and Related Effects: The Status of the Finite Temperature Correction and Limits on New Long-Range Forces," *Annu. Rev. Nucl. Part. Sci.* **62**, 1: 37 (2012).

[196] F. L. McCrackin, E. Passaglia, R. R. Stromberg, and H. L. Steinberg, "Measurement of the Thickness and Refractive Index of Very Thin Films and the Optical Properties of Surfaces by Ellipsometry," *J. Res. Natl. Bur. Stand. Sec. A.* **67**, 4: 363 (1963).

[197] A. Gil, J. Colchero, J. Gómez-Herrero, and A. Baró, "Macroscopic water deposits on polycrystalline gold measured by scanning force microscopy," *Ultramicroscopy* **86**, 1-2: 1 (2001).

[198] G. M. Sacha, A. Verdaguer, and M. Salmeron, "Induced Water Condensation and Bridge Formation by Electric Fields in Atomic Force Microscopy," *J. Phys. Chem. B* **110**, 30: 14870 (2006).

[199] G. L. Klimchitskaya, A. Roy, U. Mohideen, and V. M. Mostepanenko, "Complete roughness and conductivity corrections for Casimir force measurement," *Phys. Rev. A* **60**, 5: 3487 (1999).

[200] C. Genet, A. Lambrecht, P. A. Maia Neto, and S. Reynaud, "The Casimir force between rough metallic plates," *EPL* **484** (2003).

[201] W. Broer, G. Palasantzas, J. Knoester, and V. B. Svetovoy, "Roughness correction to the Casimir force at short separations: Contact distance and extreme value statistics," *Phys. Rev. B* **85**, 15: 155410 (2012).

[202] R. I. P. Sedmik, A. Almasi, and D. Iannuzzi, "Locality of surface interactions on colloidal probes," *Phys. Rev. B* **88**, 16: 165429 (2013).

[203] J. Villarrubia, "Algorithms for scanned probe microscope image simulation, surface reconstruction, and tip estimation," *J. Res. Natl. Inst. Stand. Technol.* **102**, 4: 425 (1997).

[204] K.-C. Fan, N. Wang, Z.-W. Wang, and H. Zhang, "Development of a roundness measuring system for microspheres," *Meas. Sci. Technol.* **25**, 6: 064009 (2014).

[205] N. A. Burnham and R. J. Colton, "Measuring the nanomechanical properties and surface forces of materials using an atomic force microscope," *J. Vac. Sci. Technol. A Vacuum, Surfaces, Film.* **7**, 4: 2906 (1989).

[206] N. A. Burnham, X. Chen, C. S. Hodges, G. A. Matei, E. J. Thoreson, C. J. Roberts, M. C. Davies, and S. J. B. Tendler, "Comparison of calibration methods for atomic-force microscopy cantilevers," *Nanotechnology* **14**, 1: 1 (2003).

[207] K.-H. Chung, G. A. Shaw, and J. R. Pratt, "Accurate noncontact calibration of colloidal probe sensitivities in atomic force microscopy." *Rev. Sci. Instrum.* **80**, 6: 065107 (2009).

[208] A. Maali, T. Cohen-Bouhacina, and H. Kellay, "Measurement of the slip length of water flow on graphite surface," *Appl. Phys. Lett.* **92**, 5: 053101 (2008).

[209] A. Labuda and R. Proksch, "Quantitative measurements of electromechanical response with a combined optical beam and interferometric atomic force microscope," *Appl. Phys. Lett.* **106**, 25: 253103 (2015).

[210] S. Watanabe and T. Fujii, "Micro-fabricated piezoelectric cantilever for atomic force microscopy," *Rev. Sci. Instrum.* **67**, 11: 3898 (1996).

[211] J. N. Munday and F. Capasso, "Reply to "Comment on 'Precision measurement of the Casimir-Lifshitz force in a fluid' "," *Phys. Rev. A* **77**, 3: 036103 (2008).

[212] R. O. Behunin, D. A. R. Dalvit, R. S. Decca, and C. C. Speake, "Limits on the accuracy of isoelectronic gravity measurements at short separation due to patch potentials," *Phys. Rev. D* **89**, 5: 5 (2014).

[213] E. D. Palik, *Handbook of Optical Constants of Solids*, Academic, New York (1998).

[214] R. O. Behunin, D. A. R. Dalvit, R. S. Decca, C. Genet, I. W. Jung, A. Lambrecht, A. Liscio, D. Lopez, S. Reynaud, G. Schnoering, G. Voisin, and Y. Zeng, "Kelvin probe force microscopy of metallic surfaces used in Casimir force measurements," *Phys. Rev. A* **90**, 6: 062115 (2014).

[215] W. J. Kim and U. D. Schwarz, "Potential contributions of noncontact atomic force microscopy for the future Casimir force measurements," *J. Vac. Sci. Technol. B Microelectron. Nanom. Struct.* **28**, 3: C4A1 (2010).

[216] S. Buchman and J. P. Turneaure, "The effects of patch-potentials on the gravity probe B gyroscopes," *Rev. Sci. Instrum.* **82**, 7: 074502 (2011).

[217] D. Hite, Y. Colombe, A. C. Wilson, D. Allcock, D. Leibfried, D. Wineland, and D. Pappas, "Surface science for improved ion traps," *MRS Bull.* **38**, 10: 826 (2013).

[218] V. G. Karpov, "Electrostatic Theory of Metal Whiskers," *Phys. Rev. Appl.* **1**, 4: 044001 (2014).

[219] J. D. Carter and J. D. D. Martin, "Energy shifts of Rydberg atoms due to patch fields near metal surfaces," *Phys. Rev. A* **83**, 3: 032902 (2011).

[220] Y. Pu, D. D. Neufeld, and F. B. Dunning, "Ionization of Rydberg atoms at metallic surfaces: Influence of stray fields," *Phys. Rev. A* **81**, 4: 042904 (2010).

[221] D. Garcia-Sanchez, K. Fong, H. Bhaskaran, S. Lamoreaux, and H. Tang, "Casimir Force and In Situ Surface Potential Measurements on Nanomembranes," *Phys. Rev. Lett.* **109**, 2: 027202 (2012).

[222] R. Decca, D. López, E. Fischbach, G. Klimchitskaya, D. Krause, and V. Mostepanenko, "Tests of new physics from precise measurements of the Casimir pressure between two gold-coated plates," *Phys. Rev. D* **75**, 7: 077101 (2007).

[223] R. S. Decca, D. López, E. Fischbach, G. L. Klimchitskaya, D. E. Krause, and V. M. Mostepanenko, "Novel constraints on light elementary particles and extra-dimensional physics from the Casimir effect," *Eur Phys J C* **51**: 963 (2007).

[224] C. Shannon, "Communication in the presence of noise," *Proc. IRE* pp. 10–21 (1949).

[225] M. Sonka, V. Hlavac, and R. Boyle, *Image processing, analysis, and machine vision*, Cengage Learning; 3 edition, third ed. (2007).

[226] J. J. Blackstock, Z. Li, M. R. Freeman, and D. R. Stewart, "Ultra-flat platinum surfaces from template-stripping of sputter deposited films," *Surf. Sci.* **546**: 87 (2003).

[227] A. Lambrecht and S. Reynaud, "Casimir force between metallic mirrors," *Eur. Phys. J. D* **318**: 309 (2000).

[228] S. K. Lamoreaux and A. O. Sushkov, "On the Origin of the log d Variation of the Electrostatic Force Minimizing Voltage in Casimir Experiments," *arXiv:1106.3549* (2011).

[229] J. Wang, S. Guan, K. Chen, W. Wu, Z. Tian, P. Luo, A. Jin, S. Yang, C. Shao, and J. Luo, "Test of non-Newtonian gravitational forces at micrometer range with two-dimensional force mapping," *Phys. Rev. D* **94**, 12: 122005 (2016).

[230] L. Collins, J. Kilpatrick, S. V. Kalinin, and B. J. Rodriguez, "Nanoscale electrical measurements in liquids using AFM - progress and outlook," *arXiv* p. 1701.06633 (2017).

[231] T. Emig, A. Hanke, R. Golestanian, and M. Kardar, "Probing the Strong Boundary Shape Dependence of the Casimir Force," *Phys. Rev. Lett.* **87**, 26: 260402 (2001).

[232] M. F. Maghrebi, S. J. Rahi, T. Emig, N. Graham, R. L. Jaffe, and M. Kardar, "Analytical results on Casimir forces for conductors with edges and tips," *Proc. Natl. Acad. Sci.* **108**, 17: 6867 (2011).

[233] C. D. Fosco, F. C. Lombardo, and F. D. Mazzitelli, "Proximity force approximation for the Casimir energy as a derivative expansion," *Phys. Rev. D* **84**, 10: 105031 (2011).

[234] G. Bimonte, T. Emig, R. L. Jaffe, and M. Kardar, "Casimir forces beyond the proximity approximation," *EPL* **97**, 5: 50001 (2012).

[235] A. W. Rodriguez, J. D. Joannopoulos, and S. G. Johnson, "Repulsive and attractive Casimir forces in a glide-symmetric geometry," *Phys. Rev. A* **77**, 6: 062107 (2008).

[236] A. W. Rodriguez, M. T. H. Reid, F. Intravaia, A. Woolf, D. A. R. Dalvit, F. Capasso, and S. G. Johnson, "Geometry-Induced Casimir Suspension of Oblate Bodies in Fluids," *Phys. Rev. Lett.* **111**, 18: 180402 (2013).

[237] D. E. Krause, R. S. Decca, D. López, and E. Fischbach, "Experimental Investigation of the Casimir Force beyond the Proximity-Force Approximation," *Phys. Rev. Lett.* **98**, 5: 050403 (2007).

[238] A. Almasi, P. Brax, D. Iannuzzi, and R. I. P. Sedmik, "Force sensor for chameleon and Casimir force experiments with parallel-plate configuration," *Phys. Rev. D - Part. Fields, Gravit. Cosmol.* **91**, 10: 102002 (2015).

[239] A. A. Banishev, G. L. Klimchitskaya, V. M. Mostepanenko, and U. Mohideen, "Demonstration of the Casimir force between ferromagnetic surfaces of a Ni-coated sphere and a Ni-coated plate," *Phys. Rev. Lett.* **110**: 137401 (2013).

[240] T. Emig, N. Graham, R. L. Jaffe, and M. Kardar, "Casimir Forces between Arbitrary Compact Objects," *Phys. Rev. Lett.* **99**, 17: 170403 (2007).

[241] P. Rodriguez-Lopez, "Casimir energy and entropy in the sphere-sphere geometry," *Phys. Rev. B* **84** (2011).

[242] M. Elzbieciak-Wodka, M. N. Popescu, F. J. Montes Ruiz-Cabello, G. Trefalt, P. Maroni, and M. Borkovec, "Measurements of dispersion forces between colloidal latex particles with the atomic force microscope and comparison with Lifshitz theory." *J. Chem. Phys.* **140**, 10: 104906 (2014).

[243] D. S. Ether, L. B. Pires, S. Umrath, D. Martinez, Y. Ayala, B. Pontes, G. R. de S. Araújo, S. Frases, G.-L. Ingold, F. S. S. Rosa, N. B. Viana, H. M. Nussenzveig, and P. A. Maia Neto, "Probing the Casimir force with optical tweezers," *EPL* **112**, 4: 44001 (2015).

[244] J. Lekner, "Electrostatic force between two conducting spheres at constant potential difference," *J. Appl. Phys.* **111**, 7: 076102 (2012).

[245] D. Iannuzzi, M. Lisanti, and F. Capasso, "Effect of hydrogen-switchable mirrors on the Casimir force." *Proc. Natl. Acad. Sci. U. S. A.* **101**, 12: 4019 (2004).

[246] S. de Man and D. Iannuzzi, "On the use of hydrogen switchable mirrors in Casimir force experiments," *New J. Phys.* **8**, 10: 235 (2006).

[247] B. Wu, A. Zimmers, H. Aubin, R. Ghosh, Y. Liu, and R. Lopez, "Electric-field-driven phase transition in vanadium dioxide," *Phys. Rev. B* **84**, 24: 241410 (2011).

[248] A. Cavalleri, C. Tóth, C. W. Siders, J. A. Squier, F. Ráksi, P. Forget, and J. C. Kieffer, "Femtosecond Structural Dynamics in VO₂ during an Ultrafast Solid-Solid Phase Transition," *Phys. Rev. Lett.* **87**, 23: 237401 (2001).

[249] N. Venkataraman, J. Pei, and C. Cremmel, "Template-Stripped, Ultraflat Gold Surfaces with Coplanar, Embedded Titanium Micropatterns," *Langmuir* (2013).

[250] C. Gong, M. R. S. Dias, G. C. Wessler, J. A. Taillon, L. G. Salamanca-Riba, and M. S. Leite, "Near-Field Optical Properties of Fully Alloyed Noble Metal Nanoparticles," *Adv. Opt. Mater.* **5**, 1: 1600568 (2017).

[251] Y. Sugawara, M. Ohta, H. Ueyama, and S. Morita, "Defect Motion on an InP(110) Surface Observed with Noncontact Atomic Force Microscopy," *Science* **270**, 5242: 1646 (1995).

[252] T. H. Boyer, "Van der Waals forces and zero-point energy for dielectric and permeable materials," *Phys. Rev. A* **9**, 5: 2078 (1974).

[253] A. Grushin and A. Cortijo, "Tunable Casimir Repulsion with Three-Dimensional Topological Insulators," *Phys. Rev. Lett.* **106**, 2: 020403 (2011).

[254] W.-K. Tse and A. H. MacDonald, "Quantized Casimir Force," *Phys. Rev. Lett.* **109**, 23: 236806 (2012).

[255] J. H. Wilson, A. A. Allocca, and V. Galitski, "Repulsive Casimir force between Weyl semimetals," *Phys. Rev. B* **91**, 23: 235115 (2015).

[256] N. Inui, "Quantum levitation of a thin magnetodielectric plate on a metallic plate using the repulsive Casimir force," *J. Appl. Phys.* **111**, 7: 074304 (2012).

[257] Wavemetrics, *Igor Pro User Manual*, 6.37 ed. (2015).

[258] Asylum Research, *Cypher User Guide* (2014).